# Development of a $^{19}F/^{1}H$ Coil for a 7 T Human Magnetic Resonance Imaging System with First Results of Non-Invasive Temperature Measurements

**Thesis**

for the degree of

**doctor rerum naturalium (Dr. rer. nat.)**

approved by the Faculty of Natural Sciences of
Otto von Guericke University Magdeburg

by Dipl.-Phys. Christian Bruns
born on December 27, 1989 in Diepholz

Examiner: Prof. Dr. rer. nat. Dr. med. Johannes Bernarding
Prof. Dr. rer. nat. Michael Bock

submitted on: August 13, 2024
defended on: January 14, 2025

# Contents

## Abstract

Fluorinated substances have attracted increasing attention in recent decades due to their interesting properties and potential uses in various research projects. $^{19}$F is an ecellent substance in magnetic resonance imaging (MRI) as it has a nuclear spin of ½, a theoretically similar MR sensitivity to protons and no natural occurence in the human body. Therefore, fluorinated substances may be ideal for the development of contrast agents. However, the construction of MRI coils is challenging due to the rather close Larmor frequencies of $^{1}$H and $^{19}$F, which in turn complicates the decoupling of double-tuned coils.

To address this issue, an MRI coil was developed in the present work that allows $^{19}$F imaging to be performed with a 7 T MRI scanner. Due to broadband characteristics of the $^{19}$F coil, $^{1}$H imaging was additionally enabled without the need for custom tuning of additional coil elements. First, simulations for the coil design were carried out, effects with different phantom types inside the developed four-element phased-array coil were discussed, and a coil was constructed which provided a homogeneous $B_1^+$ field within the phantoms.

The optimized simulated coil was finally built with 3D printing support and tested in the 7 T whole body MRI. Various fluorinated substances were measured in aqueous solution, mostly using trifluoroethanol (TFE) and heptafluorobutyric acid (HFBA). It was shown that both $^{19}$F and $^{1}$H imaging is possible with the constructed coil. Additionally, series of experiments were carried out to measure different concentrations. Here, concentrations as low as 700 $\mu$M of TFE could be detected by imaging with a signal-to-noise ratio of 2.5. This concentration in the used resolution corresponds to the detection of $5.7 \cdot 10^{16}$ fluorine nuclei per voxel.

In addition to the imaging experiments, spectroscopic investigations were also carried out at the 7 T MRI, which provided information about the structure as well as about intermolecular interactions or general changes in the environment of the nucleus under consideration. These results were confirmed by complementary measurements at a wide bore 7 T nuclear magnetic resonance (NMR) spectrometer (300 MHz proton frequency). Furthermore, the temperature-dependence of TFE and HFBA was determined using chemical shift imaging sequences proving that spatial resolution of spectroscopic measurements is possible. The various fluorinated groups exhibit characteristic chemical shift differences when the temperature changes. Using HFBA with its three fluorinated groups, a method was developed that allows the temperature to be determined without an additional reference substance to be recorded.

Concluding, this work was able to demonstrate that the developed $^{19}$F MRI coil for 7 T MRI showed a quality high enough to allow $^{19}$F/$^{1}$H imaging, spatially resolved spectroscopy and due to that temperature determination. It shows that further developments are promising for subsequent studies.

## Zusammenfassung

Fluorierte Substanzen haben in den letzten Jahrzehnten aufgrund ihrer interessanten Eigenschaften und potenziellen Verwendungsmöglichkeiten in verschiedenen Forschungsprojekten zunehmend Aufmerksamkeit auf sich gezogen. In der Magnetresonanztomographie (MRT) ist $^{19}$F eine ausgezeichnete Substanz, da es einen Kernspin von ½, eine theoretisch ähnliche MR-Empfindlichkeit wie Protonen hat und kein natürliches Fluor-Hintergrundsignal im menschlichen Körper aufweist, was es ideal für die Entwicklung von Kontrastmitteln erscheinen lässt. Der Bau von MRT-Spulen ist jedoch aufgrund der relativ nahen Larmor-Frequenzen von $^{1}$H und $^{19}$F, was eine Entkopplung der Elemente erschwert, eine Herausforderung.

In der vorliegenden Arbeit wurde eine MRT-Spule entwickelt, die die Durchführung einer $^{19}$F-Bildgebung mit einem 7 T-MRT ermöglicht. Aufgrund der Breitbandeigenschaften der $^{19}$F-Spule wurde zusätzlich die $^{1}$H-Bildgebung ermöglicht, ohne dass eine individuelle Abstimmung zusätzlicher Spulenelemente erforderlich war. Zunächst wurden Simulationen für das Spulendesign durchgeführt, Effekte mit verschiedenen Phantomtypen innerhalb der entwickelten 4-Element-Phased-Array-Spule diskutiert und schließlich eine Spule konstruiert, die ein homogenes $B_1^+$-Feld innerhalb der Phantome erzeugte.

Die optimierte simulierte Spule wurde anschließend mit Unterstützung eines 3D-Drucks gebaut und im 7 T-Ganzkörper-MRT getestet. Es wurden verschiedene fluorierte Substanzen, hauptsächlich Trifluorethanol (TFE) und Heptafluorbuttersäure (HFBA), in wässriger Lösung gemessen und die Möglichkeit von $^{19}$F- als auch $^{1}$H-Bildgebung nachgewiesen. Zusätzlich wurden Versuchsreihen zur Messung verschiedener Konzentrationen durchgeführt. Dabei konnten Konzentrationen von nur 700 $\mu$M TFE durch Bildgebung mit einem Signal-Rausch-Verhältnis von 2,5 nachgewiesen werden. Diese Konzentration in der verwendeten Auflösung entspricht dem Nachweis von $5.7 \cdot 10^{16}$ Fluor-Kernen pro Voxel.

Zusätzlich zu den Bildgebungsexperimenten wurden auch spektroskopische Untersuchungen am 7 T-MRT durchgeführt, die Informationen über die Struktur sowie über intermolekulare Wechselwirkungen oder allgemeine Veränderungen in der Umgebung des betrachteten Kerns lieferten. Diese Ergebnisse wurden durch ergänzende Messungen an einem 7 T-Kernspinresonanz Spektrometer mit breiter Bohrung bestätigt. Darüber hinaus wurde die Temperaturabhängigkeit von TFE und HFBA mithilfe von Chemical-Shift-Imaging-Sequenzen, welche räumlich aufgelöste spektroskopische Messungen erlauben, untersucht. Unter Verwendung von HFBA mit ihren drei fluorierten Gruppen, welche bei Temperaturänderung charakteristische Unterschiede in der chemischen Verschiebung aufweise, wurde eine Methode entwickelt, mit der die Temperatur ohne zusätzliche Referenzsubstanz bestimmt werden kann.

Zusammenfassend konnte diese Arbeit die Möglichkeit der $^{19}$F/$^{1}$H-Bildgebung, der ortsaufgelösten Spektroskopie und damit der Temperaturbestimmung mit der entwickelten MRT-Spule aufzeigen. Sie zeigt, dass weitere Entwicklungen für nachfolgende Studien vielversprechend sind.

# List of Figures

# 1 Introduction

Nuclear magnetic resonance was discovered in the mid-1930s was followed by the first attempts at nuclear magnetic spectroscopy (NMR) in the 1940s.[1]–[3] This ultimately led to the development of magnetic resonance imaging (MRI) in the mid-1970s. In the years and decades that followed, this in turn became a versatile and indispensable method in various fields of medicine and biomedical research.[4]–[7] The development and optimization of various MRI data acquisition methods (sequences), which can provide a wide range of information such as anatomy, neuronal activity, elastic modulus or diffusion in the contrast of the acquired magnetic resonance (MR) images, led to the wider use of MRI in biological and medical applications and ultimately in everyday clinical practice.[8], [9]

Due to their very high natural occurrence and their maximum MR sensitivity, protons are largely used in MRI for signal generation.[4] However, in view of the use of MR in molecular, metabolic and many biomedical applications, other nuclei also have a high and so far underutilized potential.

Especially since Ahrens et al. [10] showed that certain cell cultures labeled by fluorinated molecules can be bedetected by $^{19}$F MRI, fluorine imaging has also been adapted in biomedical imaging.[11]–[13] Of particular importance is that $^{19}$F has a high gyromagnetic ratio (94% of $^{1}$H), while at the same time it has almost no natural occurrence in biological systems. Simultaneously $^{19}$F is part of many fluorinated important drugs, which shows the high potential for biomedical and pharmacological research and treatment. Fluorinated substances, which can accumulate in tissues of interest for medical questions, can be used to generate $^{19}$F images, which, when superimposed on anatomical $^{1}$H images, can lead to specific contrasts providing biomarker information.[11], [14]–[17] Fluorine exhibits a relatively high MR sensitivity to environmental influences, such as pH, temperature or concentrations, and molecular changes, which are reflected in a strong change in chemical shift and relaxation times. [18]–[21]

A central challenge of heteronuclear MR methods is the low sensitivity of nuclear magnetic resonance. Especially *in vivo* achievable spin densities are often very low and thus often fall below the detection limit of the systems and require long measurement times, which is often not acceptable in the clinical routine. There are various approaches to overcoming this problem, from hyperpolarization to increasing the general $B_0$ flux density.[22], [23] This is because higher magnetic flux densities increase the signal-to-noise ratio ($SNR$) proportionally.

As described above, there are already initial approaches for $^{19}$F imaging. However, these have so far mostly performed at lower field strengths or animal scanners. Since standard clinical MRI systems are focused on $^{1}$H imaging, generally X-nuclei imaging requires separately matched Radio Frequency (RF) coils to transmit and receive signals. For this purpose, developments for most nuclei are focused on multiple transmit and receive coils.[24], [25] In clinical examinations, double resonant coils are preferred as they increase patient comfort and at the same time reduce measurement time by preventing the exchange of coils. In

$^{19}$F imaging in particular, however, the Larmor frequencies are so close together that a simple matching that covers both frequencies is used, especially for low $B_0$ flow densities.[26]

In general, the MR scanner for X-nuclei imaging must be equipped with an additional multinuclear option consisting of a broadband transmitter and a corresponding receiver chain. In addition, a suitable radio frequency (RF) system is needed for the multinuclear option. The RF coils form the interface between every MRI system and the object to be examined. A distinction is made between transmit/receive (Tx/Rx) coils and pure receive coils (Rx). In order to develop and evaluate MRI coils, prior simulation using special software for the simulation of electromagnetic (EM) fields has become established. The foundation for this was laid by Kane Yee with the development of the finite-difference time-domain (FDTD) algorithm for the simulation of time-varying EM fields.[27] Based on the idea of this algorithm, many other calculation methods were developed. One such software solution is CST studio suite 2020 software from Dassault Systèmes Simulia Corp. (`https://www.3ds.com/de/`,Providence, Rhode Island, USA)This was originally developed by Thomas Weiland at the Hamburg Helmholtz Institute DESY in 1983 and is based on the software package MAFIA (Solution of Maxwell's Equations by the Finite Integration Algorithm), which is based on finite integration technology (FIT). Depending on which calculation method is used and how complex the MRI coil, model and simulation environment are, a simulation of the EM fields and the resulting specific absorption rate requires much computing power and time. To accomplish these needs, the use of graphics cards on the hardware side can significantly accelerate the evaluation of high-resolution EM field simulations in a shorter time through parallelization, although the simulation time can still take hours or days. At the same time, so-called adaptive 3D co-simulation processes are being used to make the simulation and, above all, its adaptation more effective. [28]

Temperature in particular is an important parameter in many areas of everyday life and medicine, as knowledge of the local temperature or its temperature distribution can lead to the optimization of processes or contribute to the diagnosis and treatment (theranostics) of diseases. Examples include hyperthermia and hypothermia, inflammation, but also the investigation of implant deformations.[21], [29]–[31] Temperature measure within an MRI represents a major challenge, as conventional thermometers cannot be operated due to the strong magnetic field. This is why optical fibers are often used, although these cannot be operated non-invasively. Various methods of MR thermometry basing on proton density, proton resonance frequency,$T_1$ and $T_2$ relaxation times, magnetization transfer, and diffusion also repeatedly reveal major problems, especially for in-vivo applications.[32], [33]

The aim of this work is to further develop a phased-array coil for a Siemens 7 T whole body MRI system that allows both $^{19}$F imaging and $^{1}$H imaging, which at least in principle allows anatomical imaging. To the best of our knowledge this would be the first $^{1}$H/$^{19}$F imaging system in a human 7 T MRI scanner. For this purpose, appropriate simulations for the design had to be first be carried out. Then the design was optimized, constructed, built and implemented accordingly. In addition, a transmit-receive switch must be developed, which splits the signal accordingly and sends the received signal back to the MRI system via preamplifiers and corresponding coil files. The following test measurements will show a

possible $^{19}$F imaging on the human scanner and evaluate its limits and discuss its applicability for subsequent biomedical studies. In addition, spectroscopic investigations will be carried out to allow comparison with measurements on the NMR spectrometer.

These results will be used to develop and evaluate methods for determining temperature using fluorinated substances. Furthermore, the methods can be developed into future applications such as temperature sensitive $^{19}$F MRI as well as spatially resolved spectroscopy.

# 2 Theoretical Principles

## 2.1 Nuclear Magnetic Resonance

### 2.1.1 Semiclassical View of Nuclear Spin in the Magnetic Field

Important for the occurrence of a nuclear spin resonance is a nuclear spin $\vec{S} \neq 0$, which in general can take half or integer values. Thus a magnetic dipole moment $\vec{\mu}_M$ can be obtained:

$$\vec{\mu}_M = \gamma\hbar\vec{S}, \tag{1}$$

with the gyromagnetic ratio $\gamma$ and Planck's quantum of action $\hbar = 6.626 \cdot 10^{-34}$ Js define. A variety of atomic nuclei, such as $^1$H, $^{13}$C, and $^{19}$F possess a nuclear spin quantum number $S \neq 0$, where for medical application of MRI $^1$H with the $S = \frac{1}{2}$ is most significant, since $^1$H is found in high concentration in bound form in the water molecule or in lipids in the organism to be examined, and furthermore has a very high natural signal strength. In macroscopic terms, a semiclassical description of nuclear magnetic resonance is often sufficient. In the absence of external field, the $N$ nuclear spins are evenly distributed, so that on average they have a net magnetization

$$\vec{M} = \sum_{i=1}^{N} \vec{\mu}_i = 0. \tag{2}$$

[34] Applying an external magnetic field of flux density $\vec{B}_0$, which usually determines the Z-component of the reference frame, results in either parallel or antiparallel alignment of the nuclear spin ensemble [35] by the Zeeman effect, with an associated energy difference

$$\Delta E = \gamma\hbar|\vec{B}_0|. \tag{3}$$

The ratio of the two groups of spins of higher ($n_\beta$) and lower energy levels ($n_\alpha$) follows the Boltzmann distribution

$$\frac{n_\beta}{n_\alpha} = \exp\left(\frac{-\hbar\gamma|\vec{B}_0|}{k_B T}\right), \tag{4}$$

with Boltzmann constant $k_B$ and temperature $T$, resulting in a net magnetization $\vec{M} > 0$. This relationship between the net magnetization $\vec{M}$ and thus the signal strength and the $\vec{B}_0$ field is also one of the main arguments for the use of ever higher $\vec{B}_0$ fields in MRI research systems.

### 2.1.2 Resonance Excitation and Relaxation

Not only the magnetization is field-dependent, but also the Larmor frequency $\omega_L$, which describes the resonance frequency that gives MRI its name and at which the nuclei absorb EM radiation:

$$\omega_L = \gamma|\vec{B}_0|, \tag{5}$$

where gyromagnetic ratio $\gamma$ is isotope specific (Table 1).

**Table 1:** Larmor frequencies of the signal strongest isotopes with nuclear spin $\frac{1}{2}$ in the MR range.[36]

| **atomic nucleus** | **$\gamma$ (MHz/T)** | **spin** | **relative sensitivity to $^1$H (%)** |
|---|---|---|---|
| $^1$H hydrogen | 42.576 | $\frac{1}{2}$ | 100 |
| $^{19}$F fluorine | 40.059 | $\frac{1}{2}$ | 83.2 |
| $^{31}$P phosphorus | 17.235 | $\frac{1}{2}$ | 6.63 |
| $^{13}$C carbon | 10.705 | $\frac{1}{2}$ | 1.59 |

To describe in more detail the time course of magnetization after excited of the spins by the Larmor frequency, the so-called Bloch equations have to be solved, where the exciting magnetic field is described by $\vec{B}_1$:

$$\frac{dM_X}{dt} = \gamma(M_Y B_0 + M_Z B_1 \sin[\omega_L t]) - \frac{M_X}{T_2}, \tag{6}$$

$$\frac{dM_Y}{dt} = \gamma(-M_X B_0 + M_Z B_1 \cos[\omega_L t]) - \frac{M_Y}{T_2}, \tag{7}$$

$$\frac{dM_Z}{dt} = \gamma(-M_X B_1 \sin[\omega_L t] - M_Y B_1 \cos[\omega_L t]) - \frac{M_Z - M_0}{T_1}. \tag{8}$$

Here, the external magnetic field $\overrightarrow{B_0}$ leads to the output magnetization $\overrightarrow{M}_0$. The striving for thermal equilibrium and the interaction of the nuclei with each other, counteract this magnetization. Depending on the material, this results in longitudinal relaxation with its associated time $T_1$ and transverse relaxation (Fig. 1) with the associated time $T_2$.[1], [4].

This change in direction of the net magnetization $\overrightarrow{M}$ leads to an angular deflection between the net magnetization $\overrightarrow{M}$ and the static magnetic field $\vec{B}_0$, which is called the flip angle $\alpha$. The $\overrightarrow{B_1}$ field irradiated for the time duration $t_p - t_0$ is called a pulse. Thus, the flip angle can be used to form a measure of the excitation of the net magnetization $\overrightarrow{M}$, where the flip angle is defined as follows:[4], [38]

$$\alpha = \gamma \int_{t_0}^{t_p} B_1(t) dt. \tag{9}$$

### 2.1.3 Spin-Spin and Spin-Lattice Relaxation

The resulted flipped magnetization starts to relax after the pulse to a state of equilibrium $M_0$. The relaxation of the magnetization component $M_Z$ along the direction of the external magnetic field is called longitudinal or spin-lattice relaxation. [38]The time depence of $M_Z$ is given by

$$\frac{dM_Z}{dt} = -\frac{M_Z - M_0}{T_1}. \tag{10}$$

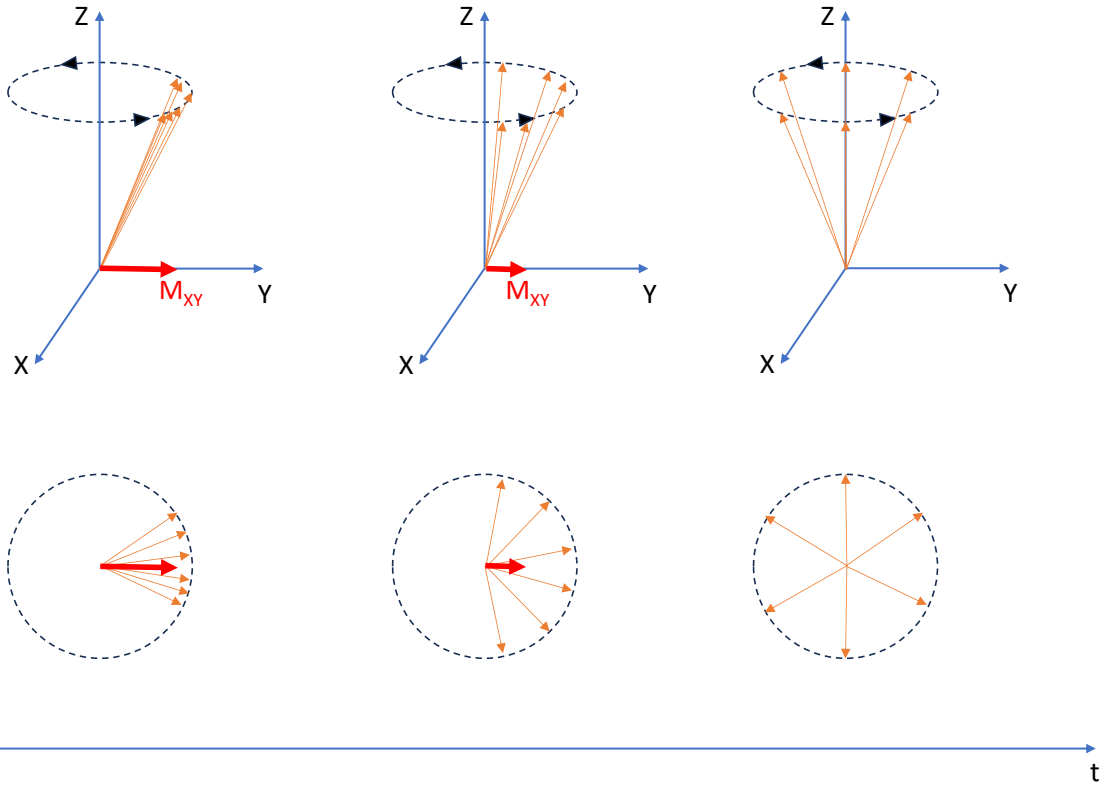


**Figure 1:** Illustration of transverse relaxation in the reference frame rotating with $\omega_L$. After a 90° pulse (a), nuclear spins begin to dephase (b, c) modified after [37].

This leads to

$$M_Z(t) = M_0(1 - e^{-t/T_1}). \tag{11}$$

The time constant $T_1$ depends on various parameters, such as composition of the sample the temperature. The development into equilibrium of longitudinal magnetization and the determination of the $T_1$ time is shown in Fig. 2. $T_1$ is typically longer for stronger magnetic fields.[38]

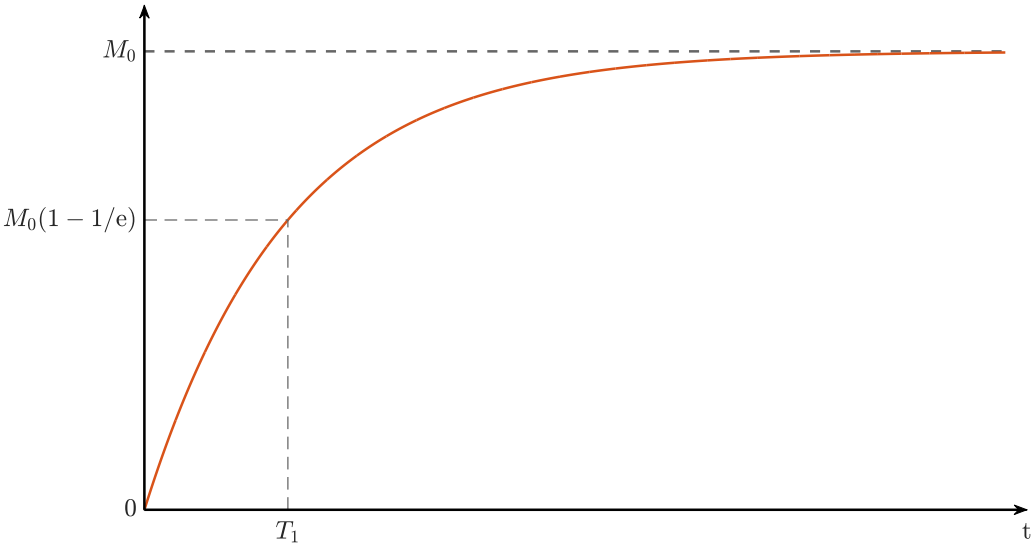


**Figure 2:** Plot of typical ongitudinal magnetization relaxation and the determination of $T_1$ according to [39].

At the same time a relaxation of the magnetisation $M_{XY}$ in transverse plane can also be detected following the Bloch equations by:

$$\frac{dM_{XY}}{dt} = -\frac{M_{XY}}{T_2}. \tag{12}$$

which results in the function

$$M_{XY}(t) = M_0 e^{-t/T_2}. \tag{13}$$

This decay with the time constant $T_2$ describes the spin-spin or transverse relaxation and is shown in Fig. 3 [40].
The effective decay of the signal as measured experimentally, is additional influenced by locally inhomogeneities of the $\vec{B}$ field. This leads to the combined time $T_2^*$ with the time constant $T_2'$, resulting from the inhomogeneity of $\vec{B}$ and the subject dependencies:

$$\frac{1}{T_2^*} = \frac{1}{T_2} + \frac{1}{T_2'}. \tag{14}$$

This results in a faster decay of signal resulting by $T_2^*$, which influences image contrast[40].

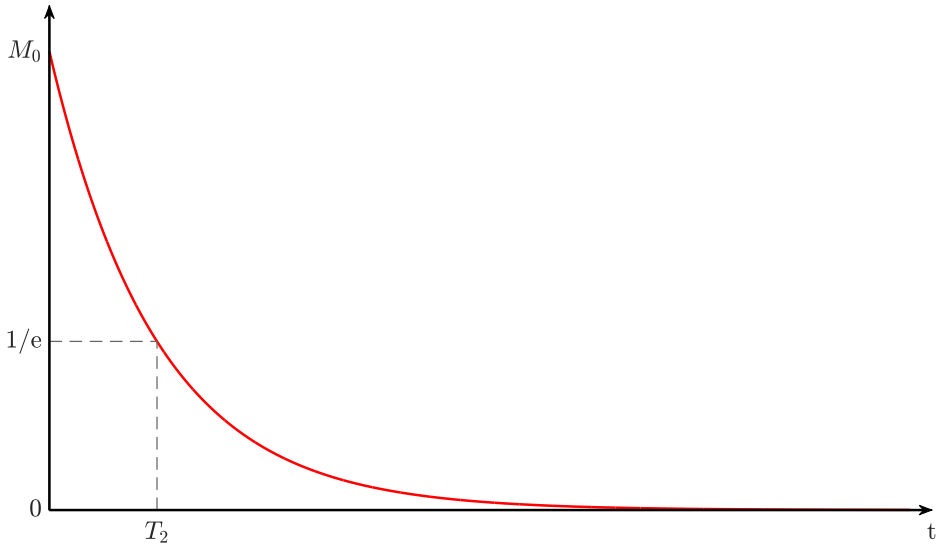


**Figure 3:** Plot of typical transverse magnetization relaxation and the determination of $T_2$ according to[39].

### 2.1.4 $B_1$ field properties

As described in section 2.1.1, the excitation process is realized by an external oscillating $\overrightarrow{B_1}$ field which is perpendicular to $\overrightarrow{B_0}$. To establish a phase coherence of the magnetic moments it has to rotate with an angular frequency where time dependency is given by a function of the modulated signal $\overrightarrow{B_{1m}}(t)$, the inital phase $\phi$ and the carrier frequency $\omega_c$ of the RF pulse:

$$\overrightarrow{B_1}(t) = Re(\overrightarrow{B_{1m}}(t)e^{-i(\omega_c t+\phi)}). \tag{15}$$

This oscillating field $\overrightarrow{B_1}$ can be decomposed into two field components: a clockwise rotating field $B_1^+(t)$ which is the effective field component for spin excitation and a anticlockwise rotating field $B_1^-(t)$. [38] After excitation of the precession of the spins, an induced voltage then can then be measured using a RF coil. [41]

## 2.2 Electromagnetic Field Simulation

### 2.2.1 Basic Idea

Electromagnetic field theory and Maxwell's equations can be used to solve many simple homogeneous problems analytically. Since complex antenna architectures can no longer be solved analytically using electromagnetic field theory, numerical methods are used that can also solve more complex and inhomogeneous electromagnetic problems. The basic idea here, as with many numerical models, is the discretization of structures that are actually continuous. Kane Yee laid the first foundations for this back in 1966 by describing how Maxwell's differential equations can be discretized both spatially and temporally using finite differences.[27] Here, the finite difference method FDTD (Finite Difference Time Domain), which works in the time domain, is one of the most established and oldest methods.[42] However, a discretization of Maxwell's equations in integral form can also be realized by the so-called FIT.[43]

### 2.2.2 Maxwell's Equations

Maxwell's equations are used to calculate electromagnetic fields and their behavior in space and time $t$., which is the basis of detecting MRI signal. Maxwell's equations can be given in both differential and integral form, with the differential form representing the electromagnetic field $\vec{E}$ and magnetic field $\vec{B}$ as a function of time $t$, permittivity $\epsilon$, permeability, $\mu$, charge distribution $\rho$ and a local point [44]:

$$\vec{\nabla} \cdot \vec{E} = \frac{\rho}{\epsilon}, \tag{16}$$

$$\vec{\nabla} \cdot \vec{B} = 0, \tag{17}$$

$$\vec{\nabla} \times \vec{E} = -\frac{\partial \vec{B}}{\partial t}, \tag{18}$$

$$\vec{\nabla} \times \vec{B} = \mu \vec{j} + \mu\epsilon \frac{\partial \vec{E}}{\partial t}. \tag{19}$$

The integral form of these equations represents the electromagnetic field $\vec{E}$ as a function of time $t$, current density $\vec{j}$ and volume $V$, areas $\vec{A}$ or curves $\vec{s}$ and can be transformed into the differential form using the integral theorems of Gauss and Stokes [44]:

$$\iiint_V \rho dV = Q(V), \tag{20}$$

$$\oint_{\partial V} \vec{B} d\vec{A} = 0, \tag{21}$$

$$\oint_{\partial A} \vec{E} d\vec{s} = -\iint_A \frac{\partial \vec{B}}{\partial t} \cdot d\vec{A}, \tag{22}$$

$$\oint_{\partial A} \vec{B} d\vec{s} = \iint_A \mu \vec{j}\, d\vec{A} + \left( \iint_A \mu\epsilon \frac{\partial \vec{E}}{\partial t} \cdot d\vec{A} \right). \tag{23}$$

The Gauss law describes the source of the electromagnetic field, i.e. the charge distribution $\rho$ is the source of the electric field $\vec{E}$ and the magnetic $\vec{B}$ field is source-free. In other words, it means that there are no magnetic monopoles.[45] The law of induction describes the effect of a temporal change of the $\vec{B}$-field to electric vortex fields $\vec{E}$ and vice versa. On the other hand, vortices of the $\vec{B}$-field depend on the electric current density $\vec{j}$ and the temporal change of the electric field $\vec{E}$. Important quantities for Maxwell's equations are the permittivity $\epsilon$ and the permeability $\mu$, which is made up of a vacuum reference quantity (index 0) and a material-dependent quantity (index $r$):

$$\epsilon = \epsilon_0 \epsilon_r, \tag{24}$$

$$\mu = \mu_0 \mu_r, \tag{25}$$

where $\epsilon_0 = 8.854 \cdot 10^{-12}$ As/Vm and $\mu_0 = 4 \cdot \pi \cdot 10^{-7}$ Vs/Am and via

$$\mu\epsilon = \frac{1}{c_r^2} \tag{26}$$

is related to the speed of light $c$ in the respective material.

### 2.2.3 Poynting Vector

The Poynting vector $\vec{S}_p$ defines the vector of the electromagnetic energy flow and is formed from the cross product of the electric field strength $\vec{E}$ and the magnetic $\vec{B}$ field [44]

$$\vec{S}_p = \frac{1}{\mu}(\vec{E} \times B). \tag{27}$$

### 2.2.4 Finite Differences Method

The discretization proposed by Yee can be illustrated by the so-called Yee cell (Fig. 4).[27] The entire spatial domain is broken down into small discrete cubic sub-elements. In these cubes, the components of the electric field are arranged at the edges and the components of magnetic field at the normals of the individual surfaces. This describes a discrete form of rotation as described in principle by the law of induction (Eq. 18), since one magnetic field component is surrounded by four electric field components. Furthermore, a primary and a nested secondary grid are formed from these cubes. The secondary grid is arranged in such a way that the surface normals of the primary grid lie on the edges of the secondary grid. The field components on the edges of the primary grid thus become surface normals of the secondary grid, which means that four magnetic field components enclose an electric one in the secondary grid. This corresponds to the rotation from the Ampère's circuital law (Eq. 19). Based on this approach, Maxwell's equations can be discretized.
The electric and magnetic fields are given by Eq. 18 and Eq. 19 via a simple relationship of the first derivative of both field types. These can be approximated with the help of the discrete difference operator [46]

$$\frac{df}{dx} \approx \frac{f(x + \Delta x) - f(x)}{\Delta x}. \tag{28}$$

The resulting equations are then solved iteratively using the so-called leapfrog method. The electric and magnetic field components are each calculated with a shift of half a time step. A complete time step therefore consists of the alternating calculation of H and E field components. These can be saved as parameters for the next time step.[47] The procedure is repeated until all field components have been determined for the entire area to be calculated and the corresponding time termination criterion has been reached. This can be defined by certain energy levels or by a specified number of time steps.

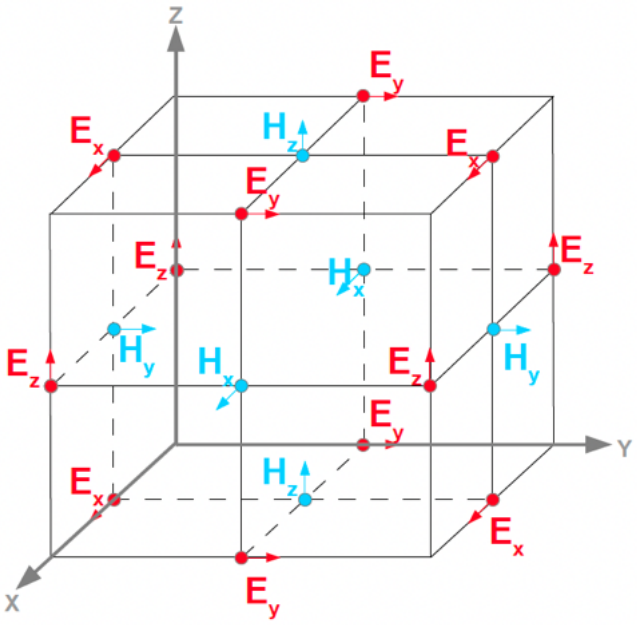


**Figure 4:** Schematic representation of the Yee cell according to [28]. The electric field components (red) are shown at the edges and the magnetic field components (blue) at the faces.

### 2.2.5 Finite Integral Method

In 1977, Thomas Weiland [43] presented an approach that also allows Maxwell's equations to be discretized in their integral form. The finite integral method, also known as the FIT, was initially presented for orthogonal grids and later generalized for arbitrary grids. For the orthogonal grid, the further procedure can again be illustrated using the Yee cell in a primary and secondary grid. From this volume covered by the grid, individual sub-volumes $V$ of the number $n_V$ and intersection surfaces of two volumes are created, which are defined as surfaces $A$ with their number $n_A$. The set of intersection lines $L$ of these surfaces is specified as $n_L$ and their intersection points $P$ as $n_P$. For each edge $L_i$ of the individual surfaces $A_j$, the electrical edge voltage is defined as

$$e_{L_i} = \oint_{L_i} \vec{E} d\vec{s}, \tag{29}$$

and the magnetic flux as

$$b_{A_j} = \int_{A_j} \vec{B} d\vec{A}. \tag{30}$$

This results for a surface from the law of induction (equation 18):

$$e_i = \frac{\partial}{\partial t} b_{A_j}. \tag{31}$$

This results in the law of induction for the entire primary grid:

$$\widehat{C}\,\vec{e} = \frac{\partial}{\partial t}\,\vec{b} \tag{32}$$

with the matrix $\widehat{C} = \widehat{(c_{ij})}$ with $i = (1, \ldots, n_A), j = (1, \ldots, n_L)$. The equation realizes the calculation of the orbital integral around the area $A_j$ with the discrete rotation operator $\widehat{C}$, whose elements accordingly assume the values -1, 0 and 1. Analogously, this can be applied to the secondary grid with the Ampère's circuital law (Eq. 19)

$$\widehat{F}\,\vec{b} = \mu\,\vec{j} + \mu\epsilon \frac{\partial}{\partial t}\,\vec{e}. \tag{33}$$

Here, $\widehat{F}$ is the discrete operator for the operations of the secondary lattice in the extended flow law.

For the first two Maxwell equations, a discrete divergence operator is required, which can be obtained from the condition for the magnetic source freedom:

$$\sum_{i=0}^{3} (b_{i+2} - b_{i+1}) = 0. \tag{34}$$

This means that all coefficients of the matrix $\widehat{D}$ with $i = (1, \ldots, n_V), j = (1, \ldots, n_A)$ must be chosen so that for each cell Eq. 34 is fulfilled so that

$$\widehat{D}\,\vec{b} = 0. \tag{35}$$

Now the electric charge $q$ in a subvolume can be represented in matrix form using macroscopic Gauss's law with the electric displacement field $\vec{d}$:

$$\widehat{D}\,\vec{d} = q. \tag{36}$$

The equations 32, 33, 35 and 36 represent Maxwell's integral equations exactly and thus represent the first part of the so-called Maxwell Grid Equations (MGE). With the material matrices $\widehat{M_\mu}$and $\widehat{M_\sigma}$, which contain the averaged material parameters for the permeability $\mu$ and the electrical conductivity $\sigma$ for each cell of the grids, a discretization can be carried out [48]:

$$\vec{b} = \widehat{M_\mu}\,\vec{h}, \tag{37}$$

$$\vec{d} = \widehat{M_\epsilon}\,\vec{e}, \tag{38}$$

$$\vec{j} = \widehat{M_\sigma}\,\vec{e}. \tag{39}$$

In this method, each individual grid cell is defined with a parameter set of these three variables. Since these are mean values, all discretization errors of this method are based on the discrete material equations, which is particularly important at interfaces.

In this work, the CST Microwave Studio® 2020 software, which uses the FIT, was used to simulate the fields of the head coil. This makes it possible to comprehensively model the physical behavior of the materials used, such as electrical conductivity, permeability and permittivity. As a result of the simulation, many properties of the model can be determined, from the S-parameters and the resulting $\overrightarrow{B_1}$ fields to the specific absorption rate (SAR).

## 2.3 MRI Coils

### 2.3.1 Coil concepts

As described in the previous sections the RF coil is used to excite the spin magnetization and receive an induced signal from the excited and relaxing spins. Quadrature excitation and detection is an important topic here, as coils with this property have a higher sensitivity by a factor of $\sqrt{2}$ when receiving $\overrightarrow{B_1}$ compared to linear coils and also have a more homogeneous RF excitation profile[49], [50]. To achieve a homogeneous flip angle (FA) $\alpha$ distribution it is necessary to have a homogeneous $\overrightarrow{B_1}$ field due to the correspondance of equation 9.

The magnitude of the $\overrightarrow{B_1}$ field depends on the square root of the power emitted to the MRI transmit coil, while the sensitivity depends on the characteristics of the receiver coil. Due to themal principles each MRI coil generates noisy results which can be characterized by

$$U_{noise} = \sqrt{4kT\Delta\nu R}, \tag{40}$$

whith the coil temperature $T$, the bandwidth $\Delta\nu$ , and the coil resistance $R$. [51]. From this relationship, the theoretical SNR can be calculated as a function of equation 42 and the the frequency $\omega_0$ and the transmit field $B_1$:[51]

$$\text{SNR} = \frac{\omega_0^{7/4} B_1}{\sqrt{4kT\Delta\nu R}}. \tag{41}$$

### 2.3.2 Surface Coil

A main characteristic of a so-called surface coil is the high sensitivity to $\overrightarrow{B_1}$ in a small excited volume and high filling factor. This feature predestines them for a efficient local signal reception. A simple solution of a surface coil is the construction with a single wire loop which generates radial ($B_{radial}$) and axial ($B_{axial}$) field components [38], as shown in Fig. 5. The resulting axial $\overrightarrow{B_1}$ field is calculated as a function of the radius $r_c$of the coil, the current $I$, and the distance $y$ from the coil:

$$B_{axial} = \frac{\mu_0 I r_C^2}{2(r_c^2 + y^2)^{3/2}}. \tag{42}$$

### 2.3.3 Volume Coil

To extend the observed volume several (surface) coils can be arranged which are used in the phased-array technique. This solution, which combines high sensitivity and an extended field of View (FoV), was first described by Roemer et al.[52] The challenge of this coil type is to demodulate and digitize each individual MR signal of each arranged coil to combine all the weak and noisy signals.

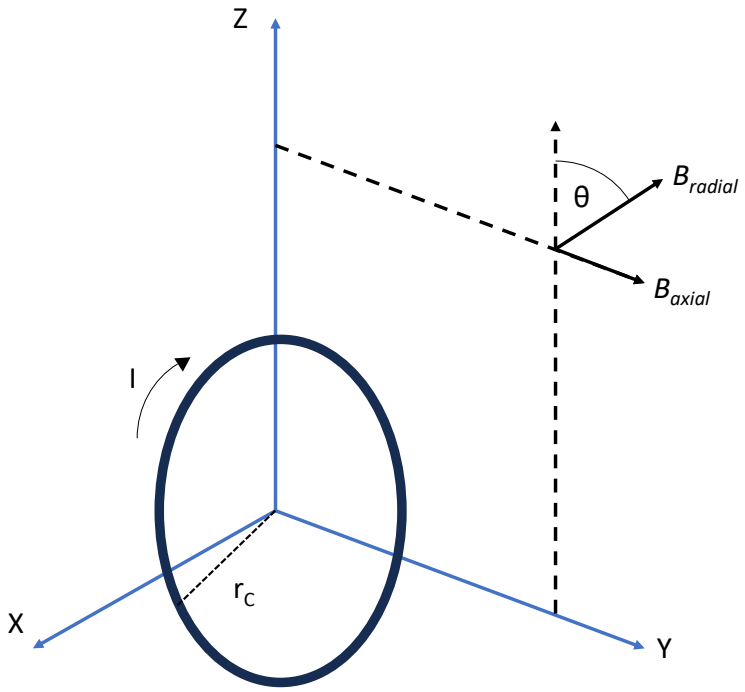


**Figure 5:** Geometry of field directions of a basic surface coil according to [38]. Z-direction is in field direction of $\overrightarrow{B_0}$.

A typical problem when using phased array coils is the inductive mutual coupling between the various coil elements. To reduce the coupling between the arranged coils, different strategies exists.A widely used method is the overlapping of neighboring elements as shown in Fig. 6.

Due to inductance law the coupling generates a voltage in the neighboring element which is dependent on the distance between the elements. To bring this resulting coupling to a minimum the relative ratio between the diameter and the distance was optimized. This otimum was found to 1/0.78 for circular loops (Fig. 6a) and 1/0.86 for square loops (Fig. 6b). [52] While this works well for interaction of neighboring coil elements this does not solve the mutual induction in more distant coil elements (i.e. next-but-one neighbors). This coupling can be reduced by avoiding currents flowing in the surface coils generating magnetic coupling. This is solved by coils with low intrinsic impedance and impedance transformers what avoids currents in the surface coils for very small preamplifier impedances.

## 2.4 Basics of Conduction Theory

For the construction of the monopole antenna head coil, some aspects of line theory had to be taken into account and it was necessary to measure some parameters, such as the S-parameters for characterization, which are briefly explained here.

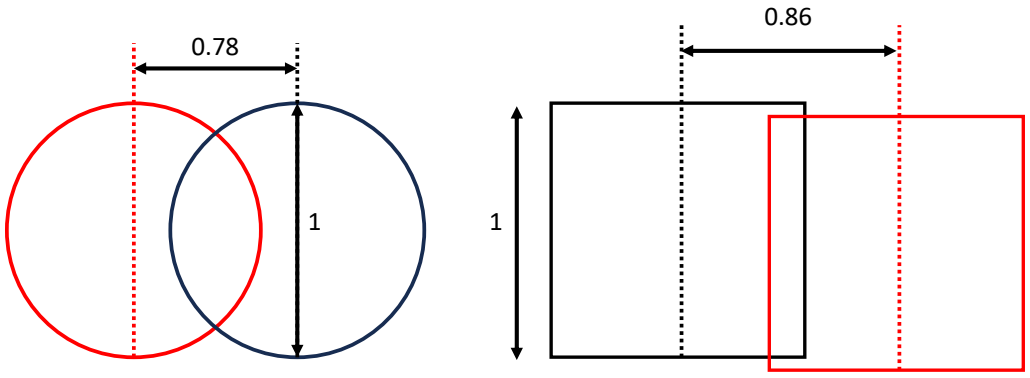


**Figure 6:** Relative overlapping of neighboring coil elements to reduce inductive coupling. Concept shown for (a) circular and (b) square loop coils with normalized relationship according to [52].

### 2.4.1 Line Equivalent Circuit Diagram

An infinitesimal section of an electrical line can be represented as an equivalent circuit diagram consisting of capacitive, inductive and resistive elements and thus serves as the basis for an analytical calculation. From this equivalent circuit diagram, it is then possible to calculate the longitudinal load, i.e. the resistance load $R'$ and the inductance load $L'$ :

$$R' = \frac{\Delta R}{\Delta z}, \tag{43}$$

$$L' = \frac{\Delta L}{\Delta z}. \tag{44}$$

On the other hand, the transverse coatings, i.e. the capacitance coating $C'$ and the conductance coating $G'$

$$C' = \frac{\Delta C}{\Delta z}, \tag{45}$$

$$G' = \frac{\Delta G}{\Delta z} \tag{46}$$

can be calculated. From these, the impedance layer $Z'$ and the admittance layer $Y'$ can then be represented in complex form as follows using the mesh and node rules [53]:

$$Z' = R' + i\omega L', \tag{47}$$

$$Y' = G' + i\omega C'. \tag{48}$$

In conduction theory, we speak of waves $U^+, I^+$ traveling in the positive z-direction and waves $U^-, I^-$ traveling back in the negative z-direction. If there is no optimal matching at the end of the line, reflections can result. These result in a field superposition that varies periodically due to outgoing and returning waves, which in turn can be characterized by the so-called standing wave ratio (SWR). The line equations here represent the propagation

behavior for current and voltage of the forward and return waves via the longitudinal and transverse coverings and the propagation constant $\gamma_p$:

$$U(z) = U^+ e^{-\gamma_p z} + U^- e^{+\gamma_p z}, \tag{49}$$

$$I(z) = I^+ e^{-\gamma_p z} + I^- e^{+\gamma_p z}. \tag{50}$$

### 2.4.2 S-Parameter

In high-frequency technology, the scattering parameters (S-parameters) are an important parameter for determining the transmission characteristics of an electrical line. In the field of high-frequency technology, the S-parameters are much more effective than conventional equivalent circuit diagrams, as their parameters are frequency-dependent. Furthermore, S-parameters are complex and dimensionless and they form the entries of the scattering matrix that connects the outgoing ($\vec{a}$) and returning ($\vec{b}$) waves:

$$\vec{b} = \widehat{S} \cdot \vec{a}. \tag{51}$$

The S-parameters for a port can only be recorded if the other ports are matched with their characteristic impedance. This means that the reflection and transmission can be determined for any number of gates or ports using the S-parameters. The most common measurement of the S-parameters takes place for two ports [54]:

$$\begin{pmatrix} b_1 \\ b_2 \end{pmatrix} = \begin{pmatrix} S_{11} & S_{12} \\ S_{21} & S_{22} \end{pmatrix} \begin{pmatrix} a_1 \\ a_2 \end{pmatrix}. \tag{52}$$

# 3 Development of a 7 T $^{19}$F/$^{1}$H Coil for MR Imaging

## 3.1 System Hardware

This chapter presents the development of an MRI coil for $^{19}$F and $^{1}$H imaging on 7 T MRI. The 7 T MRI system (Magnetom, Siemens, Erlangen, Germany) consisted superconducting magnet (Magnex Magnet Technology, Oxford, UK) with a diameter of 90 cm, filled by a body gradient system with a diameter of 60 cm. and a maximum strength of 70 mT m$^{-1}$s$^{-1}$.

For transmission, eight RF power amplifiers (operating at both, 297.2 MHz, the larmor frequency of $^{1}$H and 279.6 MHz, the larmor frequency of $^{19}$F) with a maximum power of 1 kW for single-channel operation each were interconnected at the existing system. New hardware and coilfiles had to be added, as described in the following sections. The modulated RF signal containing the imaging information and carrier signals of 297.2 MHz and 279.6 MHz, respectively and the combined signals were amplified. [55] The $B_1$ sensitivity depended mainly on the power of the RF coil and the preamplifier.

## 3.2 Construction of Power Dividers, Transmit/Receive Switches, and Phase Shifter

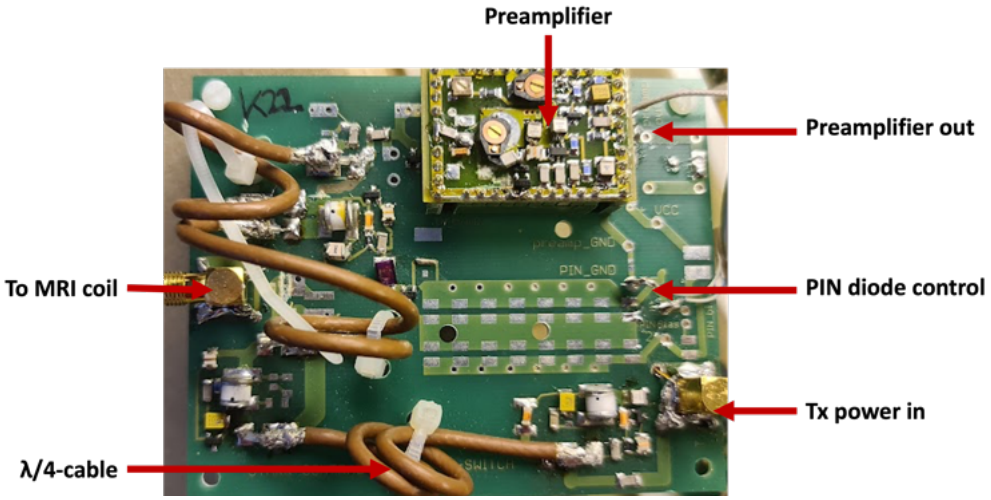


**Figure 7:** Linear Tx/Rx switch for $^{19}$F imaging on a 7 T MRI including preamplifiers with 4 x 10 pin footprint. The RF ports were marked and also the control of the pin-diode to control the system. The board has a total size of 10 x 8 cm$^2$ with a height of 3 cm.

To connect the transmit power from MRI system to the coil and to switch the receive mode and as well as to preamplify the receiving signal additional RF circuits are required. These Tx/Rx switches were commercial linear Tx/Rx switches for $^{1}$H (Fig. 7) from Stark Contrast (Erlangen, Germany). The $\lambda/4$ cable which was originally convectioned for $^{1}$H was shortened in order to that the transmission for $^{19}$F is optimally adapted. These switches

were actively operated via positive intrinsic negative (pin-)diodes. These had a bias current of +100 mA in Tx mode and could be switched by a voltage of -30 V to Rx mode. In addition, passive protection was provided for faults or excessive power handling, which was used to protect the preamplifiers. For connection, the boards were equipped with three RF ports: one port for power in, one port for connecting the coil and one port behind the preamplifier to the 7 T MRI system. All ports were prepared for connection to coaxial cables. In addition, a space for preamplifiers was provided on the boards. The boards had a total size of 10 x 8 $cm^2$ with a height of 3 cm.

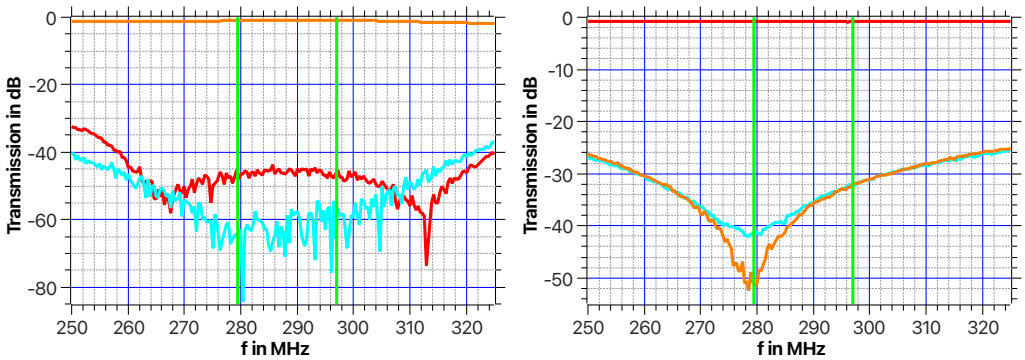


**Figure 8:** Frequency response of the Tx/Rx switches in passive and active mode. The passive mode is shown on the left and the active mode on the right. The connection from the power supply to the MRI coil is shown in red, the connection from the MRI coil to the preamplifier in orange and the possible connection from the power supply to the preamplifier in turquoise. The Larmor frequencies of $^{19}F$ and $^{1}H$ are shown in green.

The preamplifiers with a footprint of 4 x 10 pins, which were optimized to 279.578 MHz, were installed directly on this board. These had a high reflection for preamplifier decoupling of individual coil elements with a protection circuit at input and high output level for 0.1 dB compression point.

To finally test the adapted Tx/Rx switch and check the parameters, the transmission was examined in active and passive status. For this purpose, an external voltage of -30 V was applied to the pin-diode to simulate a switching process. In active mode (voltage applied), the transmit direction should be activated (and thus the receive channel switched off) and in passive mode (no voltage applied), the receive direction should be active (and the RF power supply interrupted).

In Fig. 8 you can clearly see the switching process and corresponding channel releases or blockages that protect the elements. The respective contact points on the Tx/Rx switches were firstly the Tx power in, then the channel to the MRI coil and directly before the preamplifier.

In order to adapt the MRI's single-channel RF transmission system to the 4-element coil, power splitters had to be implemented. A typical solution for this is to use Wilkinson power dividers, which not only divide the RF power evenly, but also have excellent port isolation, low losses and, most importantly, negligible phase shifts [55], [56]. Here, all ports were matched to 50 Ω to reduce reflection and achieve the optimum power division ratio efficiency. The realized solution is displayed in Fig. 9. The attenuation from the input to the output ports, the isolation between the output ports and the phase shift between the output ports were optimized by using a network analyzer (FieldFox, Keysight, Santa Rosa, USA). Three two-way Wilkinson power dividers were then cascaded so that four connections with an equal phase shift were available for the coil at the other end.

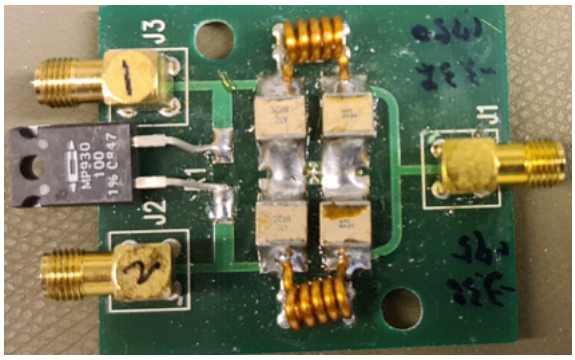


**Figure 9:** Constructed Wilkinson Power Divider with two 50 Ω matched output ports on the left and one input port on the right.

For an ideal lumped element Wilkinson power divider [56], the inductance $L$ and capacitance $C$ can be calculated by

$$L = \frac{R}{\sqrt{2}\pi f}, \tag{53}$$

$$C = \frac{1}{2\sqrt{2}\pi f R}. \tag{54}$$

Once the power deviders had been constructed, their transmission was measured accordingly. This showed an extremely accurate match of the two outputs, which each had 3.4 dB and 3.6 dB attenuation for the corresponding Larmor frequencies of $^{1}$H and $^{19}$F (see Fig. 10). There is also a very good agreement of the resulting phase shift (Fig. 11). Here, both channels showed a phase shift of 137.1 ° and 103.5 ° for the corresponding Larmor frequencies of $^{1}$H and $^{19}$F. As a result, there was no phase difference between the two elements.

A 90° phase-shifted RF power signal with the same amplitude in the RF coil was required for transmission. For this purpose, delay lines were introduced downstream of the power divider at the four outputs. These were designed using semi-rigid, formable microwave cables with an attenuation of less than 0.4 dB/m of cable type EZ_141_CU_TP. In order to achieve the corresponding phase shifts, the following lengths were cut and convected for the channels:

1. 100.0 mm
2. 286.3 mm
3. 472.6 mm
4. 658.9 mm

The final constructed Tx/Rx-Box is shown in Fig. 12.

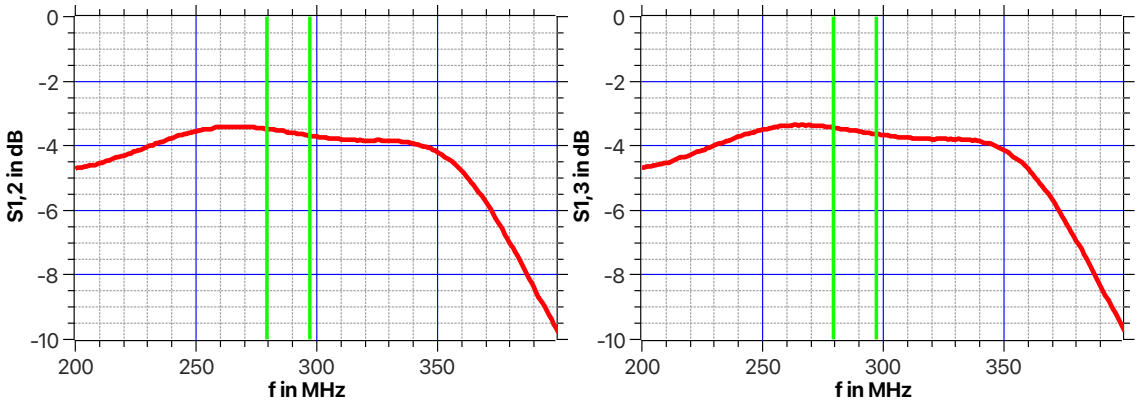


**Figure 10:** Frequency dependency of the magnitude of constructed Wilkinson power divider.The transmission magnitude from the input to the two outputs is shown here. The respective Larmor frequencies for $^{19}$F and $^{1}$H are marked in green.

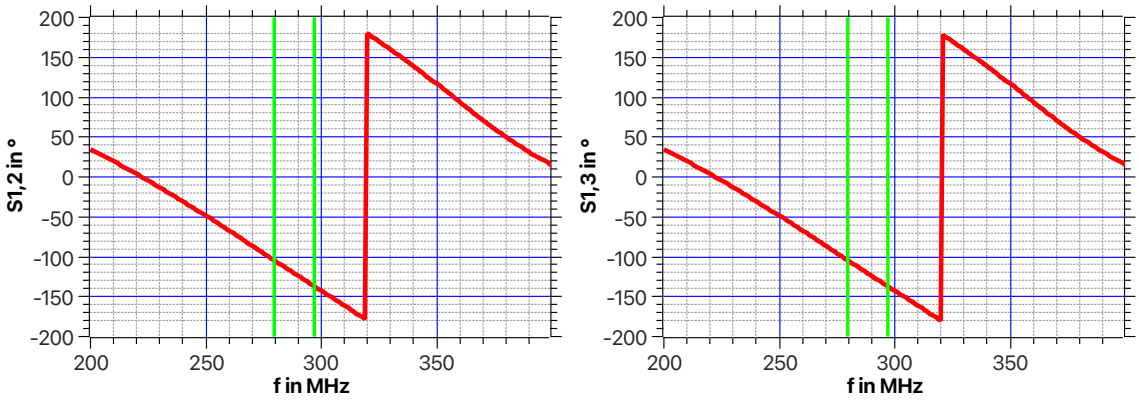


**Figure 11:** Frequency dependency of the phase of constructed Wilkinson power divider. Shown here is the transmission phase from the input to the two outputs. The respective Larmor frequencies for $^{19}$F and $^{1}$H are marked in green.

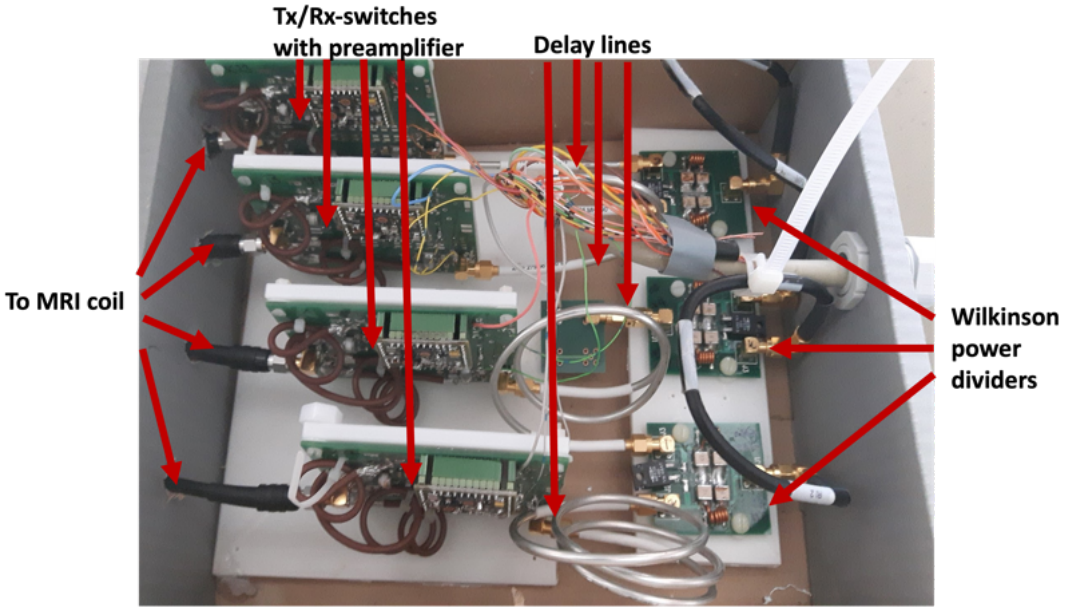


**Figure 12:** Self developed Tx/Rx switch box with HF power divider and delay lines for the phase shift.

## 3.3 Design of a Surface Coil

### 3.3.1 Simulations of a Surface Coil

Since a classic phased-array coil consists of several surface coils, this chapter first describes the simulation and setup of a surface coil for 7 T MRI. This is intended to demonstrate the feasibility of $^{19}$F imaging on the one hand and to reduce possible sources of error if several elements are later combined on the other. In the next step, in chapter 3.4, the knowledge of the surface coil will be used in order to build a phased-array coil.

When implementing a field simulation, the first step is to select the type of MRI coil based on the desired field of application. Sufficient knowledge of the expected behavior of the coil model to be simulated is helpful for interpreting the results and identifying possible errors in the modeling at an early stage. The EM field simulation software can usually be used to create the model if it is equipped with the appropriate Computer Aided Design (CAD) tools. If this is not the case, import functions are available that enable the integration of models from CAD design applications.[28]

How detailed the MRI coil needs to be modeled depends on the objective for the results. If absolute results must match the measurable results in the real MRI environment as closely as possible, a model of the MRI coil must be created that is as true to the original as possible. The effort required for such a simulation is significantly higher than when looking at relative results: it is usually sufficient to examine how results change with specific parameter variations. In this case, only the behavior of the MRI coil is examined when one or more parameters are changed, although it should be noted that this change in the results also depends on the level of detail of the MRI coil used.

For an effective and fast implementation of the EM field simulation, it is usually useful to first look at relative results in order to evaluate how they develop. This can save an enormous amount of time and resources. Once the system response to specific variations in system parameters is available, a more detailed model can be created to calculate the final version of the EM field simulation.

Co-simulation is extremely important for the simulation of MRI coils.[28] For the co-simulation, the S-parameters for each port of the 3D EM field simulation are determined by a simulation in the time domain. For this reason, all discrete components are first replaced by ports. By energizing one port and simultaneously terminating all the other ports with 50 Ω, the S-parameters at this port are determined. This calculation is performed for all ports. A complex resonant simulation is thus broken down into many non-resonant sub-simulations that can be calculated much faster. Subsequently, within the co-simulation software, any component with a known impedance can be used for each port and the entire structure can be calculated using the superposition principle.

The established field simulation software applications offer two possible ways to create a grid. The purely automatic adaptive grid resolves very fine structures, which potentially have a strong influence on the results, to a higher degree. Other areas are then weighted less

heavily. Depending on the software, different algorithms are used to create the automatic grid, e.g. geometric edges should also be represented by interfaces between grid cells. The correct linking of the concentrated components with the coil architecture must also be ensured. Current software applications usually take this into account automatically. Nevertheless, a manual follow-up check is required to ensure an accurate grid and to make manual adjustments if necessary.

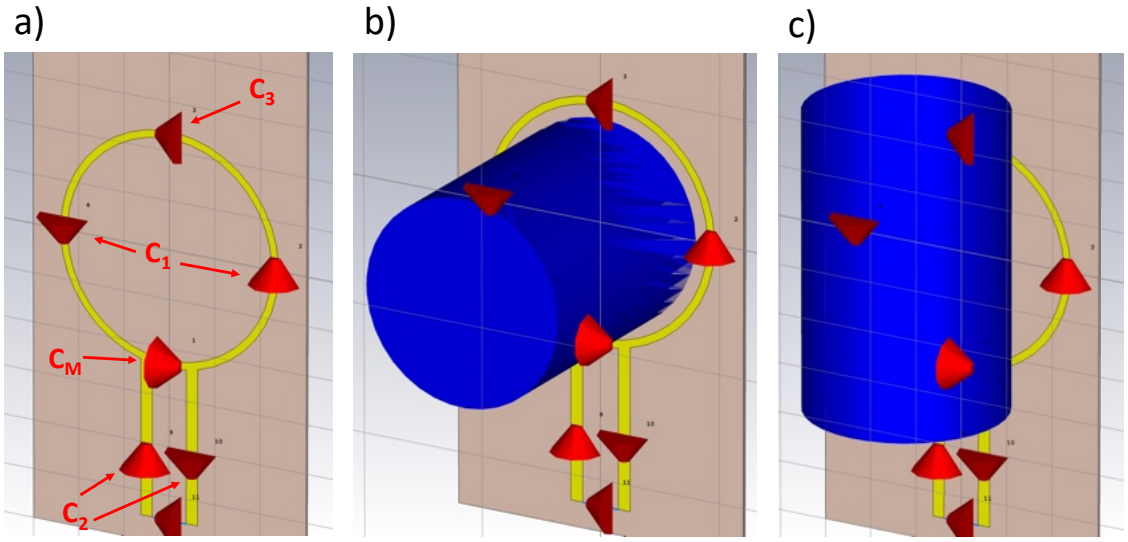


**Figure 13:** Design sketch of the surface coil. a) Surface coil with a full-port design of all elements (red). b) Surface coil loaded with an upright cylindrical phantom filled with water. c) Surface coil loaded with a cylindrical phantom filled with water and aligned parallel to the coil surface.

When using the Time-Domain solver, the convergence criterion is important for the accuracy of the field simulation results. At the end of a simulation, the system should be completely free of energy. Particularly in the case of resonant systems, care must be taken to ensure that the system energy has completely decayed. In this work, a system energy limit value of -60 dB was set for a system that no longer oscillates. The EM simulation software records the remaining field energy within the simulating volume. For valid results, the fed in energy must have been completely converted into field energy. If the system continues to oscillate at -60 dB, the field simulation must be continued until the energy has completely decayed in order to achieve valid results.

The CST studio suite 2020 software from Dassault Systèmes Simulia Corp. was used to realize these simulations. For this purpose, the surface coil was first modeled and all capacitances were replaced by so-called ports as described above (Fig. 13 a). The MR coil has an inner diameter of the active elements of 9 cm. A simple cylindrical water phantom was initially selected on top. In order to assess the influence of orientation and shapes close

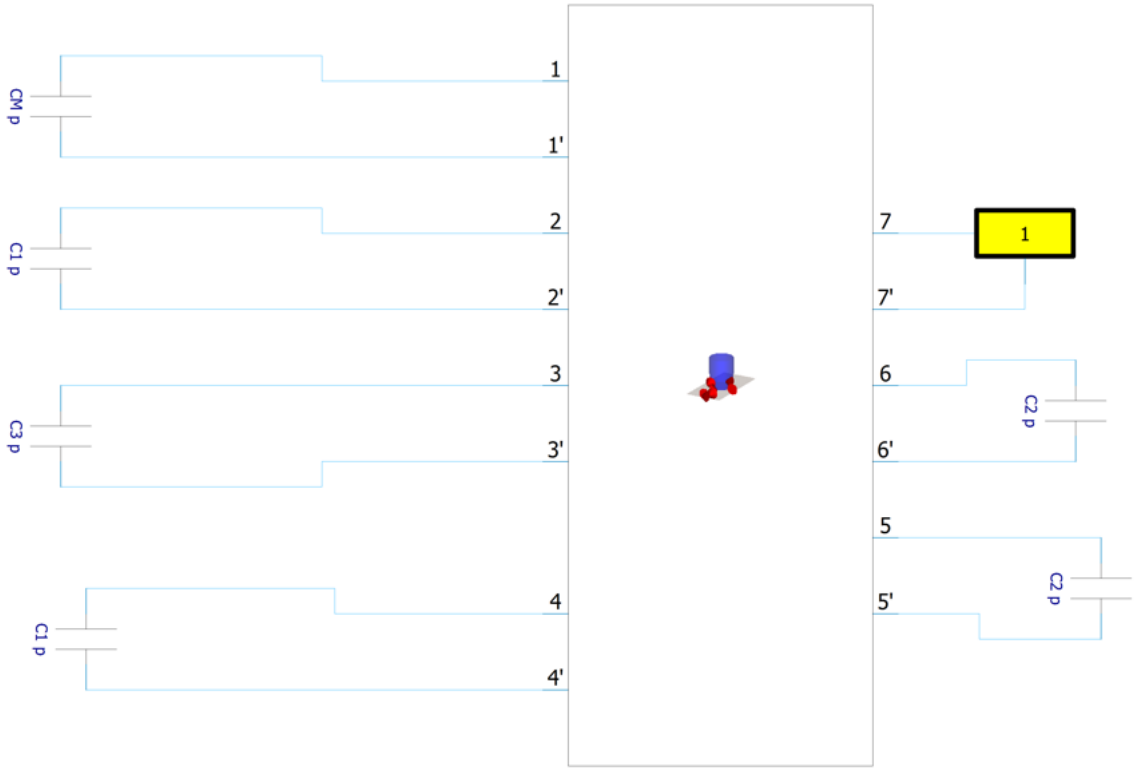


**Figure 14:** Connections for the ports in Fig. 13. $C_1$ are the capacitances on the right and left of the circle. $C_2$ describes the capacitances in the lower tuning and matching network on the left and right. $C_3$ describes the capacitance on the opposite side of the tuning and matching network and $C_M$ describes the lower capacitance in the circle of the coil. The numbers are the numbers of the outputs in the ports in the full port simulation, while the inputs are marked with dashes.

to the coil, the phantom was rotated in two different directions as shown in Fig. 13 b and c.

In the background, all ports were then replaced with the corresponding inserted element (in this case only capacitances, see Fig. 14).

After modeling, a mesh was then generated that was very fine in the area of the phantom and the coil and thinned out in the outer area in order to generate the best possible ratio of mesh cells and resolution of the field distribution. In addition, open boundary conditions were assumed, as it can be assumed that corresponding structures in the MRI can only be expected after a large distance from the coil. Around 6 million mesh cells were used in the simulations for the surface coil. The volume of these cells ranged from 0.5 $\mathrm{mm}^3$ to 23 $\mathrm{mm}^3$.

Next, the S-parameters were simulated and then the capatities were optimized by co-simulation so that the reflection parameters are directly at the Larmor frequency of $^{19}$F and yet some signal can also be expected in the $^{1}$H range. The capacitances defined as in Fig. 13 found for this are composed as follows:

- $C_1 = 14\,\mathrm{pF}$,
- $C_2 = 4\,\mathrm{pF}$,
- $C_3 = 14\,\mathrm{pF}$,
- $C_M = 4\,\mathrm{pF}$.

After the simulation described above and corresponding optimization in the co-simulation, the above-mentioned capacitances in the grid generate S-parameters as shown in Fig. 15.

The field distributions for the $B_1^+$ fields were then determined in the field simulations (Fig. 16). Since surface coils in particular have the great advantage of being freely positionable on the measurement object, the other extreme of orthogonal alignment was also simulated in addition to parallel alignment to the $B_0$ field (Fig. 17).

Finally, in order to gain a comparison of the influence of the position or shape close to the coil on the field distribution and the S-parameters, the same simulation was carried out again with similar mesh cells (a small difference could not be avoided due to the changed geometry) for the setup as in Fig. 13 c). This revealed a slightly different distribution of the S-parameters with the same capacitance settings, which can be seen in Fig. 18.

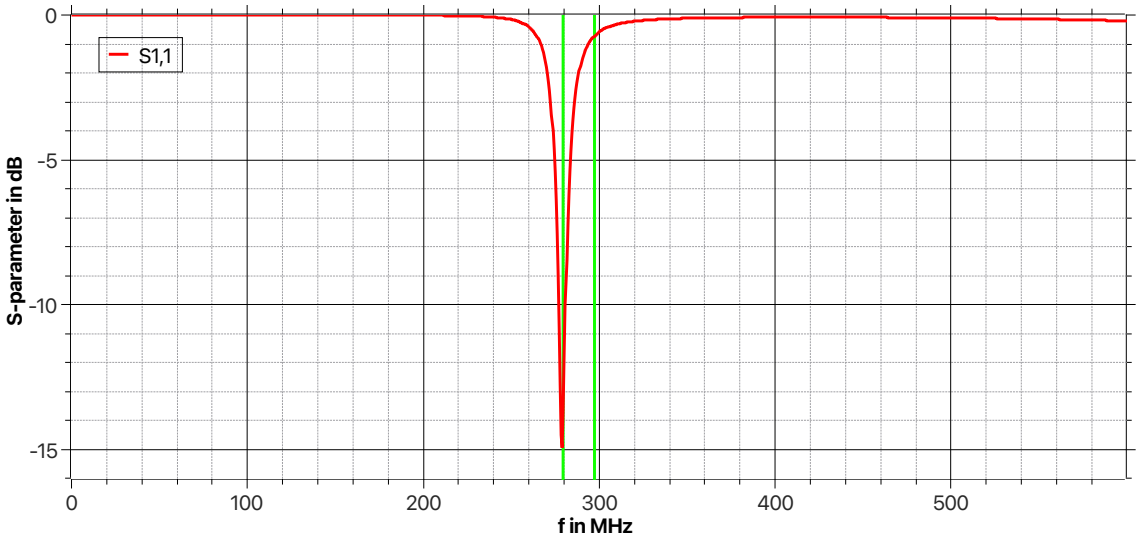


**Figure 15:** S-parameter (in this case only reflection parameters, as there is only one channel) of the surface coil with an upright water-filled cylinder phantom as a load (see Fig. 13 b). The green lines mark the resonance frequencies of $^{19}$F (279.5 MHz) and $^{1}$H (297.2 MHz).

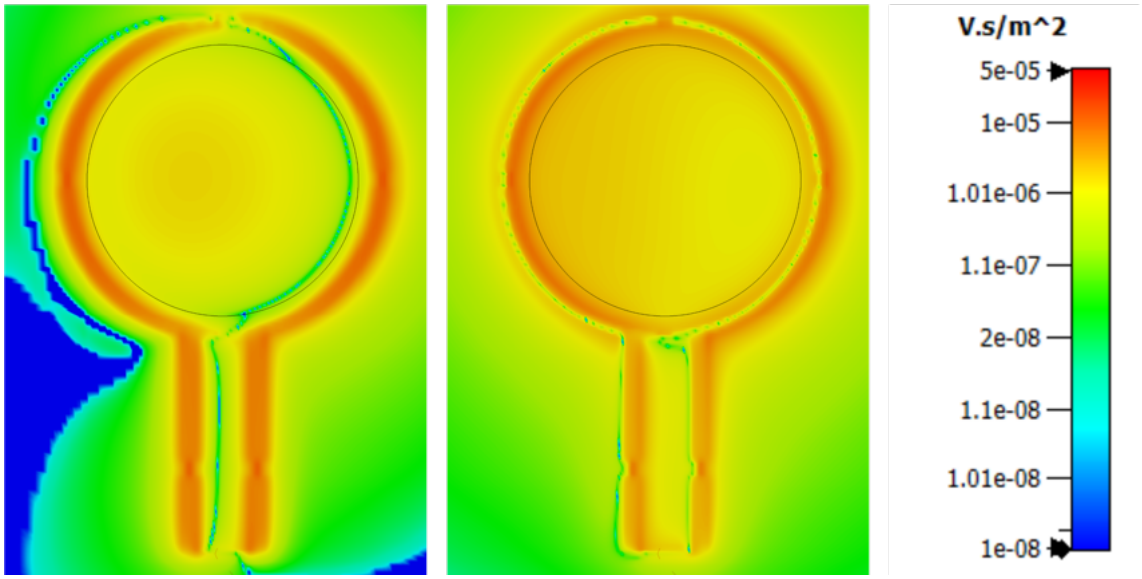


**Figure 16:** RF-field simulation of the surface coil (see Fig. 13 b) with an upright water-filled cylinder phantom as a load depicted by black lines. The orientation of the coil is in plane parallel to $\vec{B}_0$. The left (right) image depict the $B_1^+$-field distribution in a coronal plane in the center of the coil for 279.5 MHz, the Larmor frequency of $^{19}$F (297.2 MHz, the Larmor frequency of $^{1}$H). The colorbars show the field strength in Vs/m$^2$ in a logarithmic representation.

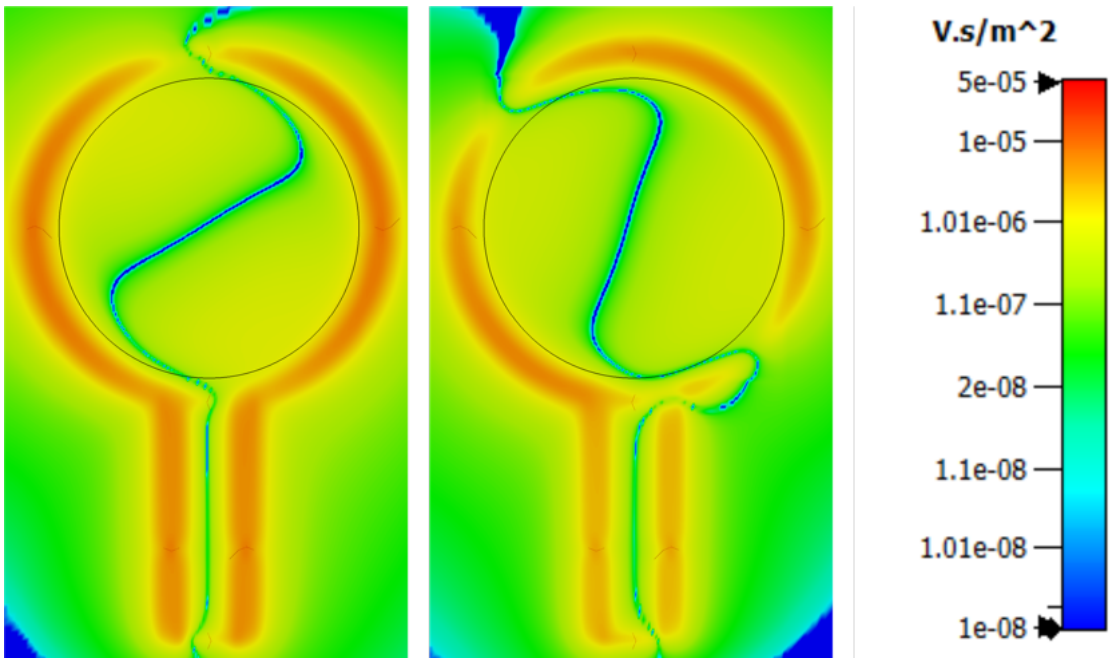


**Figure 17:** RF-field simulation of the surface coil (see Fig. 13 b) with an upright water-filled cylinder phantom as a load depicted by black lines. The orientation of the coil is in plane orthogonal to $\vec{B}_0$. The left (right) image depict the $B_1^+$-field distribution in a coronal plane in the center of the coil for 279.5 MHz, the Larmor frequency of $^{19}$F (297.2 MHz, the Larmor frequency of $^{1}$H). The colorbars show the field strength in Vs/m$^2$ in a logarithmic representation.

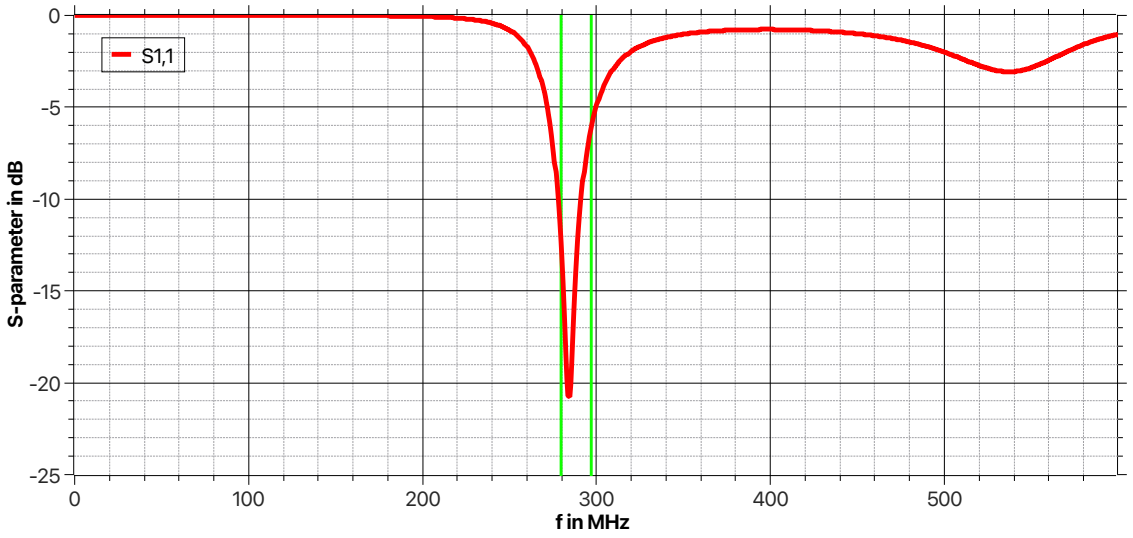


**Figure 18:** S-parameter (in this case only reflection parameters, as there is only one channel) of the surface coil with a laying water-filled cylinder phantom as a load (see Fig. 13 c). The green lines mark the resonance frequencies of $^{19}$F (279.5 MHz) and $^{1}$H (297.2 MHz).

### 3.3.2 Hardware of a Surface Coil

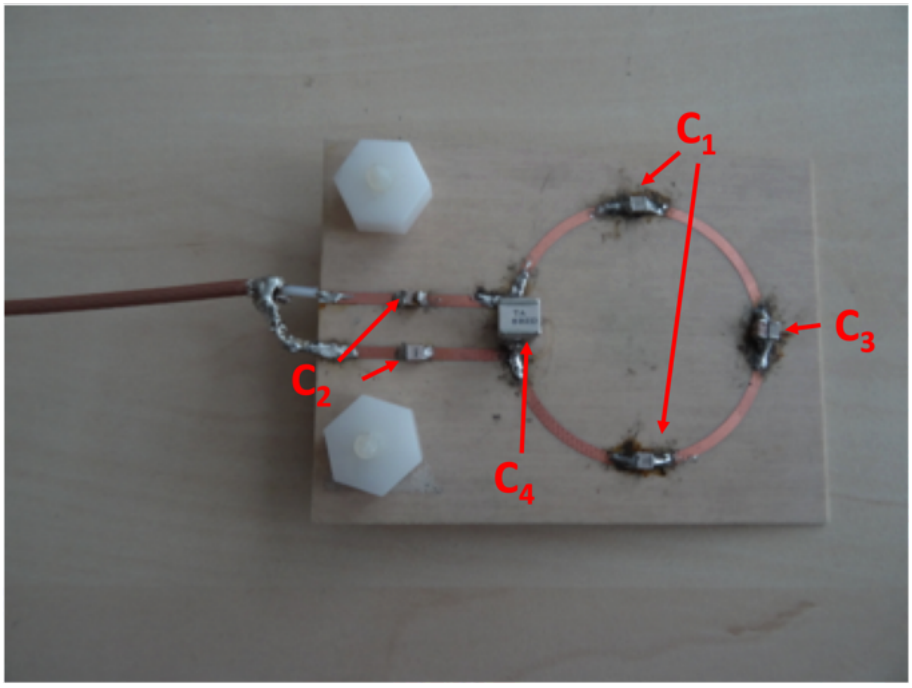


**Figure 19:** Picture of the built surface coil. The surface coil consists of a glass fibre plate with glued-on copper tape and soldered-in capacitors. The exact values of the capacitors are listed in the text for the capacitors $C_1$, which can be seen on the sides of the circle. The capacitors $C_2$ describe those which are located directly in the tuning and matching network on the sides. The capacitor $C_3$ is the one on the opposite side of the tuning and matching network, at the top of the MRI coil. Finally, $C_4$ describes the matching capacitance at the bottom of the coil, which is shared with the tuning and matching network.

When building the surface coil, the experience gained from the simulation was initially used. A glass fibre plate with an applied copper strip was used for the coil itself, as can be seen in Fig. 19. Capacitances were applied to the gaps, as in the simulation, and the reflection parameters were adjusted as best as possible for 279.5 MHz, the resonance frequency of $^{19}$F. It turned out that the Capacitances values of the simulation could be used very well to achieve a first fit. The final values of the manual optimization carried out to be

- $C_1 = 11\,\mathrm{pF}$,
- $C_2 = 4.7\,\mathrm{pF}$,
- $C_3 = 10\,\mathrm{pF}$,
- $C_M = 32.2\,\mathrm{pF}$.

for the definition in Fig. 19. The final optimized version, which was used for the later experiments, resulted in the reflection parameters as shown in Fig. 20.

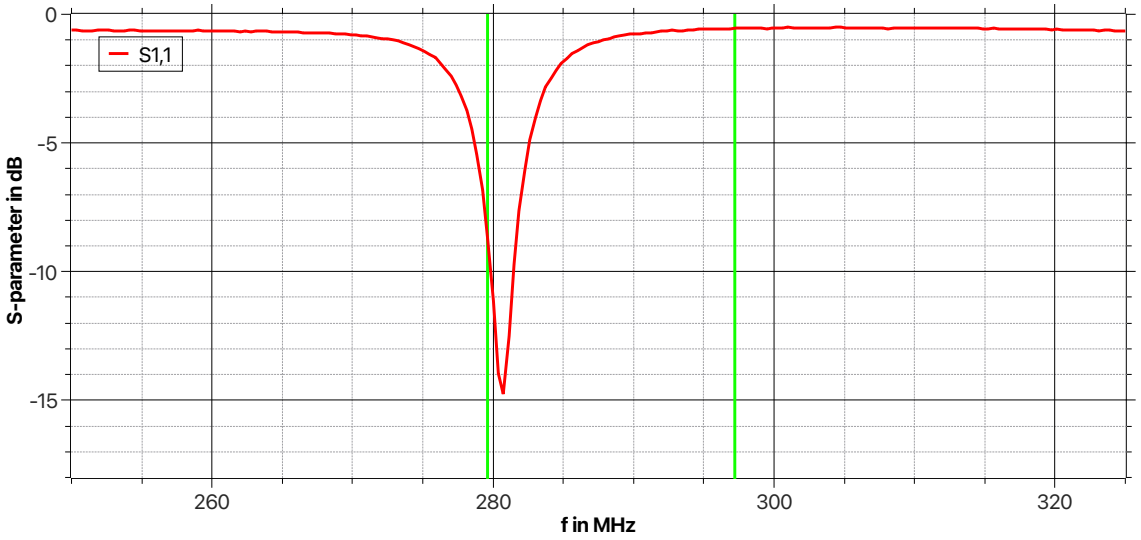


**Figure 20:** Measured S-parameter of the constructed surface coil with standing water-filled cylinder phantom as a load (see Fig. 47 c). The green lines mark the resonance frequencies of $^{19}$F (279.5 MHz) and $^{1}$H (297.2 MHz).

Once this coil had been adjusted accordingly and prepared as best as possible for the measurements, it was connected to the transmit-receive switch (see Fig. 7) using a coaxial cable. The transmit-receive switch with its preamplifier was afterwards connected directly to the 7 T MRI.

## 3.4 Design of a Phased-Array Coil

This chapter describes the development and construction of a four-element phased-array MRI coil. Many of the experiences gained with the surface coil in chapter 3.3 are utilised and further developed. The basic concept of this coil is a combination of several simple elements that are very similar to a standard surface coil in order to utilise its positive properties and to be able to cover a larger volume. The approach here is to generate the $B_1^+$ distribution in the best possible way by means of a phase shift between the elements. As the coil used here consists of four evenly circularly arranged elements, the ideal phase shift is 90° in each case. This chapter also describes how the initial design experience is gained via simulation, which is then later transferred to a built coil and adjusted manually.

### 3.4.1 Simulations of a Phased-Array Coil

Similar to section 3.3.1, this coil was also initially modelled in a CAD model using the CST studio suite 2020 software, as shown in Fig. 21. First, a round plastic housing with an outer diameter of 8 cm and a wall thickness of 0.5 cm was created and copper tracks were attached to it in a rectangle that extends over the round plastic housing. The copper conductor track was then interrupted for various lumped elements and ports. However, as in section 3.3.1, these were initially all represented by ports in order to be able to perform a co-simulation again and to be able to carry out a good matching of the entire network in a time-efficient manner. This rectangular element was now distributed evenly four times on the coil housing.

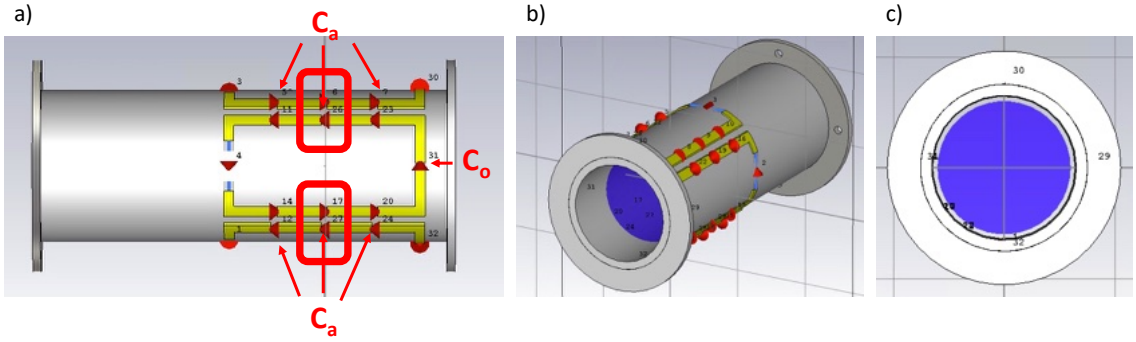


**Figure 21:** Modelling of the four-element phased-array coil. a) side view, the red frames indicate the ports that will be connected later for capacitive decoupling via additional capacitances (see also Fig. 22). Additionally all ports, which were lateron replaced are shown by name definitions; b) front view; c) perspective view. The outer diameter of the MRI coil is 8 cm. The model was filled by a cylindric water phantom with a diameter of 6 cm.

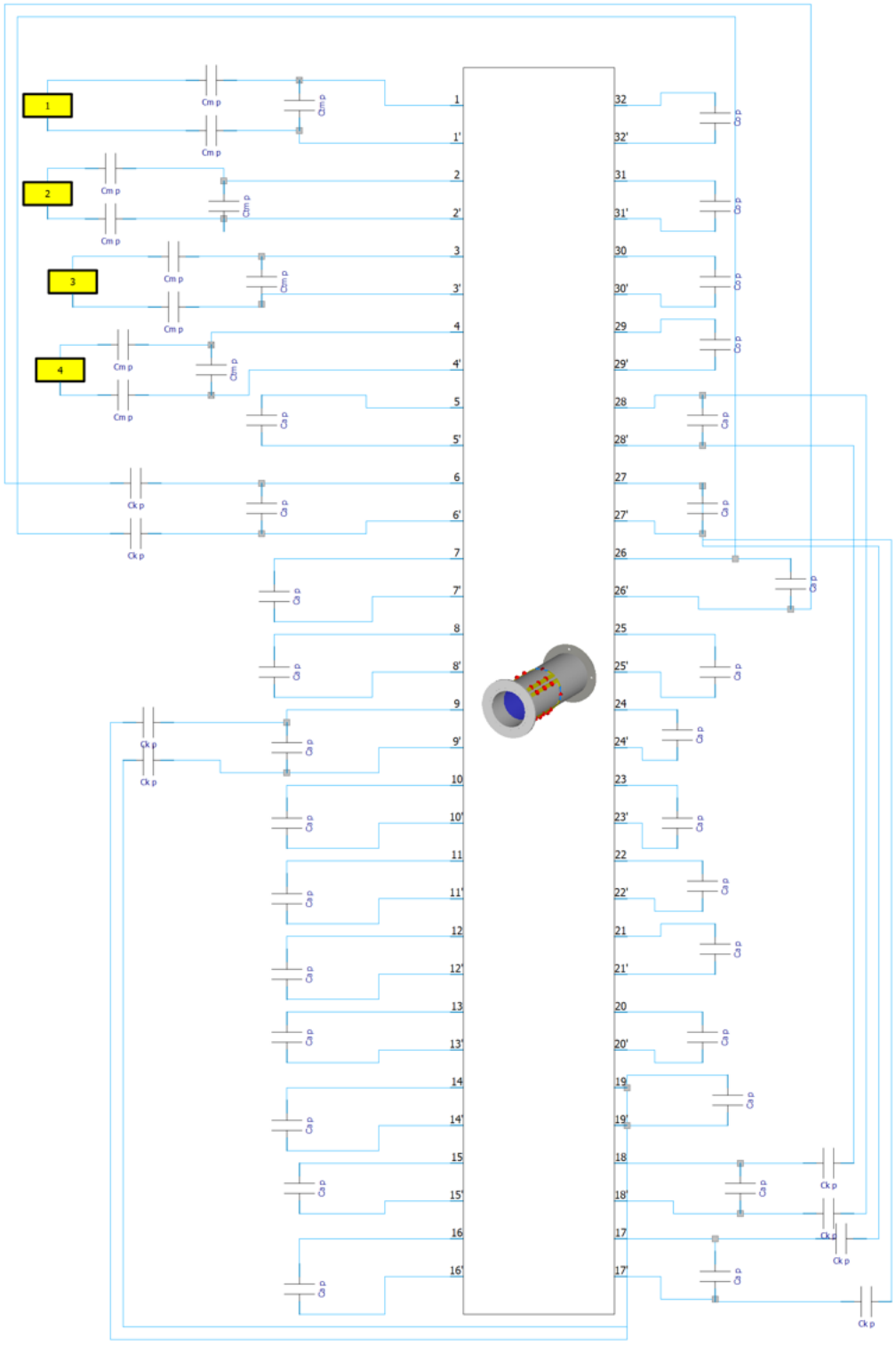


**Figure 22:** Circuit of the four-element phased-array coil. All virtual ports in the construction (see Fig. 21) were replaced by a function. Ports 1-4 are active ports including a tuning and matching network. All the other ports were replaced by capacitances. Additionally the adjacent middle elements in each array were combined by capacitances for decoupling of each coil-element.

Subsequently, various phantom shapes were analysed in this chapter to investigate their influence on the field distributions and S-parameters. In the first approach, a round cylindrical phantom was selected, which largely fills the coil. The meshs used for these simulations had around 11 million mesh cells (with a small variation, depending on the phantom).

A network was then created in the co-simulation area that comes as close as possible to the real MRI coil to be built later. This network can also be seen in Fig. 22. For this purpose, the excitation ports were provided with a tuning and matching network consisting of two symmetrically arranged capacitors and a connecting capacitor. All the other ports were replaced by capacitors, whereby the capacitors, which are directly adjacent in the middle, were connected symmetrically by further capacitors in order to create capacitive decoupling. The red frames in Fig. 21 show the position.

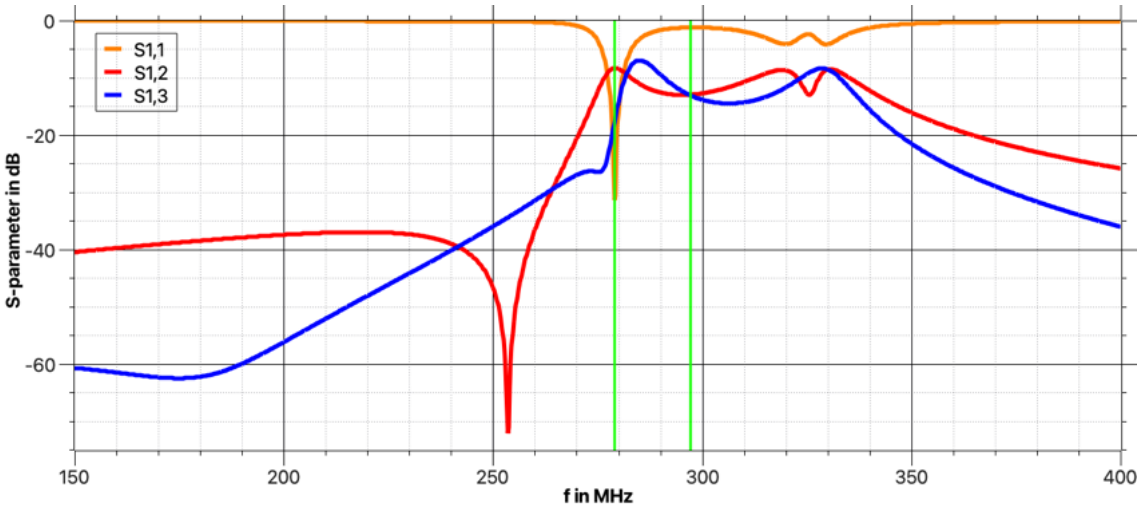


**Figure 23:** S-parameters for the four-element phased-array coil (see Fig. 21) with a cylinder phantom as load. Three S-parameters were listed as examples, which are identical to the others due to the symmetry. Here, S1,1 applies to the reflection parameters S1,1; S2,2; ... The coupling parameters for the nearest neighbors S1,2; S1,4; S2,3; ... are also identical. The reflection parameters of the opposite elements S1,3; S2,4; ... are then the last category accordingly. The green lines mark the resonance frequencies of $^{19}$F (279.5 MHz) and $^{1}$H (297.2 MHz).

Next, the S-parameters were simulated (Fig. 23) and then the capacitances were optimized by co-simulation so that the reflection parameters are directly at the Larmor frequency of $^{19}$F and yet some signal can also be expected in the $^{1}$H range. The capacitances found for this are composed as follows:

- Matching capacitances $C_m = 14\,\mathrm{pF}$,
- Mixed tuning and matching capacitances $C_{tm} = 10\,\mathrm{pF}$,

- Decoupling capacitances $C_k = 17\,\mathrm{pF}$,
- Capacitances on the opposite side the ports $C_o = 15.5\,\mathrm{pF}$,
- Remaining capacitances in the network $C_a = 13\,\mathrm{pF}$.

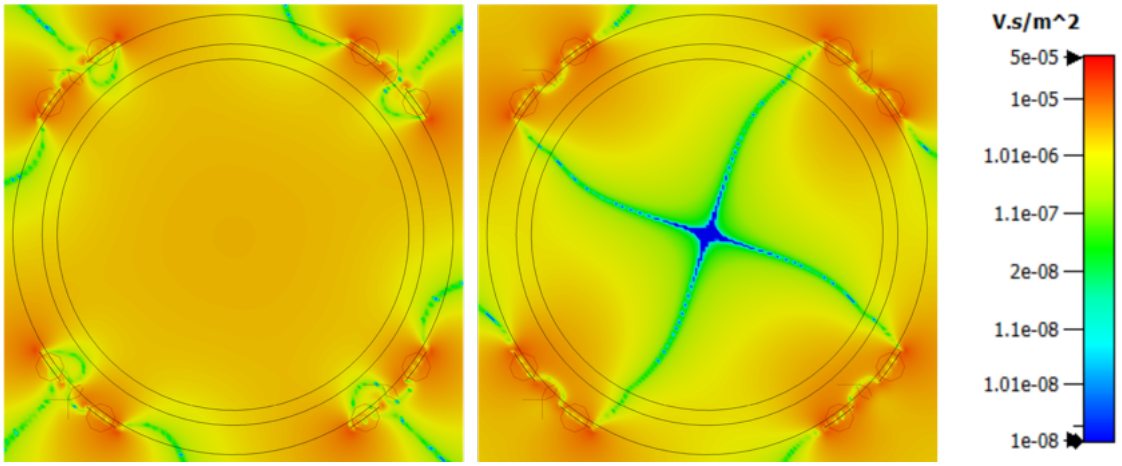


**Figure 24:** Fullport RF-field simulation of the four-element phased-array coil (see Fig. 21) with a cylinder phantom as load at 279.5 MHz, the Larmor frequency of $^{19}$F. The view is a central axial slice of the field distribution. The left (right) image depicts the $B_1^+$ ($B_1^-$) field distributions. The colorbars show the field strength in Vs/m$^2$ in a logarithmic representation.

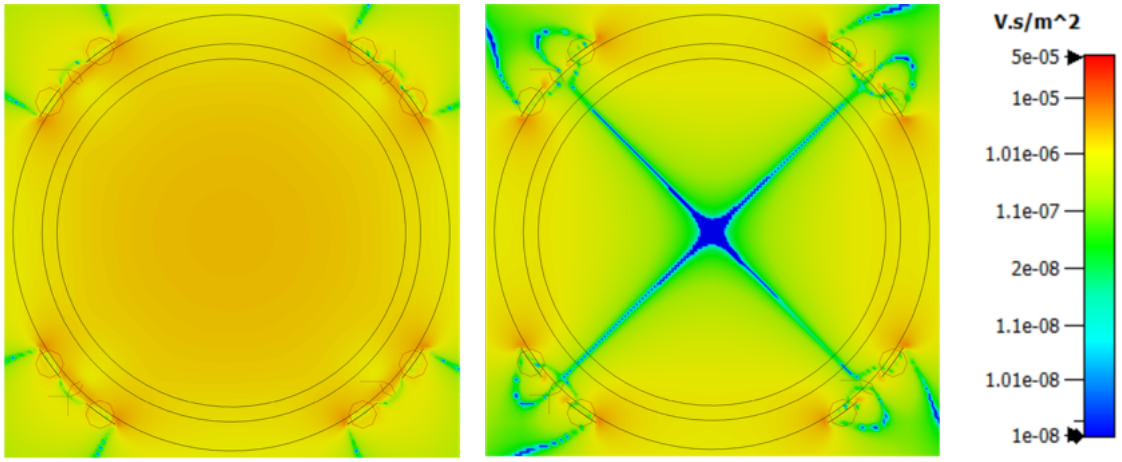


**Figure 25:** Fullport RF-field simulation of the four-element phased-array coil (see Fig. 21) with a cylinder phantom as load at 297.2 MHz, the Larmor frequency of $^{1}$H. The view is a central axial slice of the field distribution. The left (right) image depicts the $B_1^+$ ($B_1^-$) field distributions. The colorbars show the field strength in Vs/m$^2$ in a logarithmic representation.

Next, the resulting $B_1^+$ and $B_1^-$ field distributions were calculated and analyzed. This was done for the Larmor frequency of $^1$H and $^{19}$F respectively (Fig. 24 and 25).

In addition, a further series of simulations was carried out to observe how the coil behaves in the event of incomplete and inhomogeneous filling. Later in the experiments, it became clear that it was helpful to use Falcon$^{TM}$ Tubes as phantoms, as they were cylindrical and could be used to investigate different concentrations without requiring a large amount of material. Therefore, in the following series of experiments, it was decided to position four Falcon$^{TM}$ Tubes in the same coil (see Fig. 26).

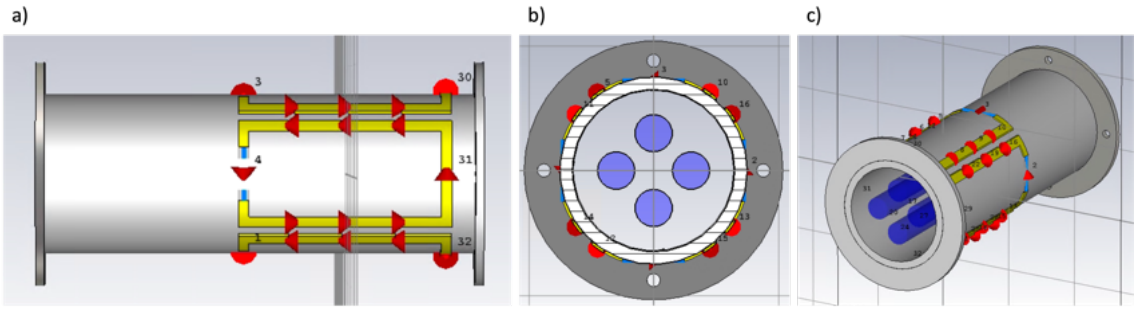


**Figure 26:** Modelling of the four-element phased-array coil filled by four 15 mm diameter and 12 cm long water tubes. a) Side view; b) front view; c) perspective view. The MR coil has the same design as in Fig. 21.

In the following, the S-parameters were also simulated for this variant. This showed a slight shift in the S-parameters (see Fig. 27), as the load and shape were different from those of a filling cylinder phantom. This also led to a change in the field distributions. It is noticeable that the absolute $B_1^+$-fields are higher at $^1$H frequency than at $^{19}$F frequency (see Fig. 28). To analyze this phenomenon, a comparison of the losses was also carried out (see Fig. 29).

To counter the results and also find an optimum for this setting, another slightly modified tuning and matching was carried out for this setup, which is shown in the S-parameters in Fig. 30. The values for this tuning and matching are as follows:

- Matching capacitances $C_m = 17\,\text{pF}$,
- Mixed tuning and matching capacitances $C_{tm} = 11\,\text{pF}$,
- Decoupling capacitances $C_k = 25\,\text{pF}$,
- Remaining capacitances in the network $C_a = 13.5\,\text{pF}$.

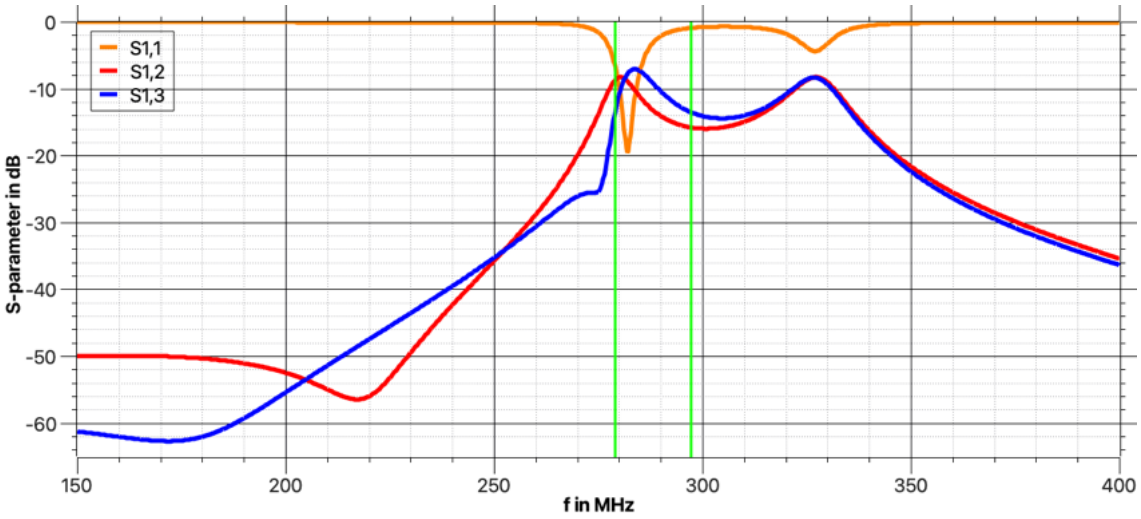


**Figure 27:** S-parameters for the four-element phased-array coil (see Fig. 26) with four water tubes as load. Three S-parameters were listed as examples, which are identical to the others due to the symmetry. Here, S1,1 applies to the reflection parameters S1,1; S2,2; ... The coupling parameters for the nearest neighbors S1,2; S1,4; S2,3; ... are also identical. The reflection parameters of the opposite elements S1,3; S2,4; ... are then the last category accordingly. The green lines mark the resonance frequencies of $^{19}$F (279.5 MHz) and $^{1}$H (297.2 MHz).

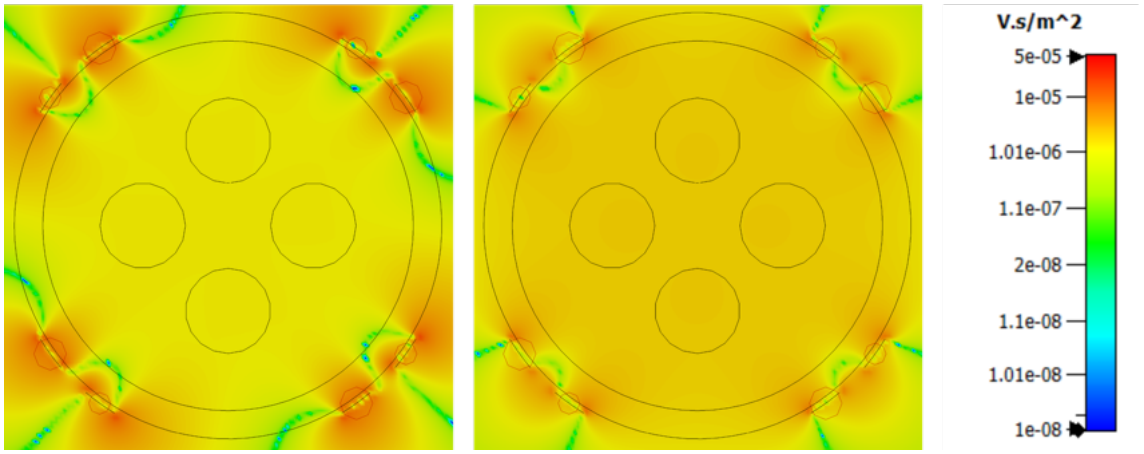


**Figure 28:** Fullport RF-field simulation of the four-element phased-array coil (see Fig. 21) loaded by four cylindric water tubes for the same tuning and matching as for the cylindric phantom. The view is a central axial slice of the field distribution. The left side shows the $B_1^+$-results for 279.5 MHz, the Larmor frequency of $^{19}$F. The right side shows the $B_1^+$-results for 297.2 MHz, the Larmor frequency of $^{1}$H. The colorbars show the field strength in Vs/m$^2$ in a logarithmic representation.

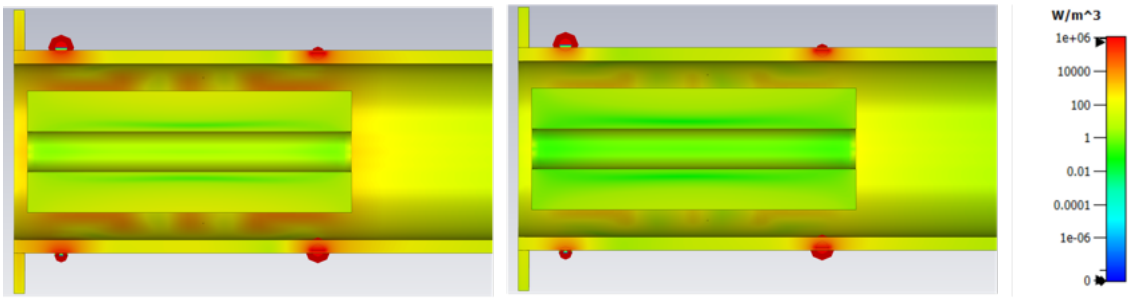


**Figure 29:** Loss-field simulation results for a fullport simulation of the four-element phased-array coil (see Fig. 21) for the RF-field simulation of Fig. 28. The view is a central saggital slice of the field distribution. The left side shows the loss-results for 279.5 MHz, the Larmor frequency of $^{19}$F. The right side shows the loss-results for 297.2 MHz, the Larmor frequency of $^{1}$H. The colorbars show the field strength in W/m$^3$ in a logarithmic representation.

The $B_1^+$ and $B_1^-$ field distributions after this tuning and matching for the respective Larmor frequencies were also shown in the axial direction in Figs. 31 and 32 and in the sagittal direction in Fig. 33.

Finally, a spherical phantom was generated for the four-element MR coil (see Fig. 34). This has the advantage that there are no sharp edges in any spatial direction. On the other hand, spherical phantoms (see Fig. 49) were used in later temperature experiments and for this reason alone it is interesting to see how S-parameters and field distribution behave.

The S-parameters were also determined for the sphere phantom and here, a shift of the S-parameters as in Fig. 35 can be seen, too. Just as with the four water tubes, the image of a poorer $B_1^+$ field distribution was also shown here, especially with regard to the $^{19}$F frequency, which is why a loss image was also generated here (Fig. 36).

Again, a new tuning and matching was then carried out, which found the following parameters to be optimal:

- Matching capacitances $C_m = 8\,\text{pF}$,
- Mixed tuning and matching capacitances $C_tm = 6\,\text{pF}$,
- Decoupling capacitances $C_k = 80\,\text{pF}$,
- Remaining capacitances in the network $C_a = 14.5\,\text{pF}$.

The S-parameters (Fig. 37), the axial field distributions for the $^{19}$F (Fig. 38) and $^{1}$H frequencies (Fig. 39) were also determined for this purpose and a saggital view for both $B_1^+$ field distributions was generated (Fig. 40).

Finally, another simulation was carried out in which only one port was excited and the three other elements including the matching network were connected with 50 Ω. The results

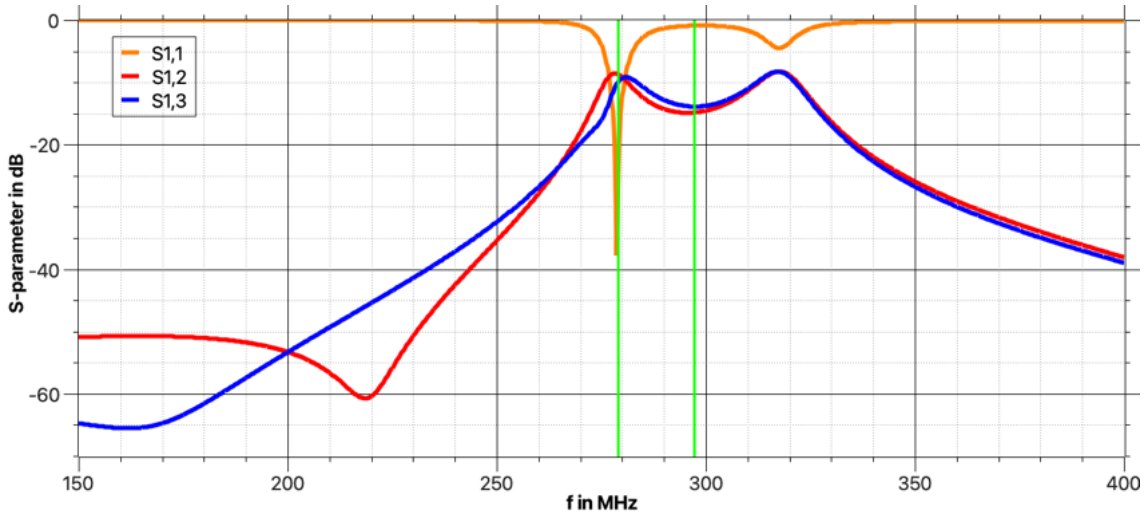


**Figure 30:** S-parameters for the four-element phased-array coil (see Fig. 26) with four water tubes as load after retuning and matching. Three S-parameters were listed as examples, which are identical to the others due to the symmetry. Here, S1,1 applies to the reflection parameters S1,1; S2,2; ... The coupling parameters for the nearest neighbors S1,2; S1,4; S2,3; ... are also identical. The reflection parameters of the opposite elements S1,3; S2,4; ... are then the last category accordingly. The green lines mark the resonance frequencies of $^{19}$F (279.5 MHz) and $^{1}$H (297.2 MHz).

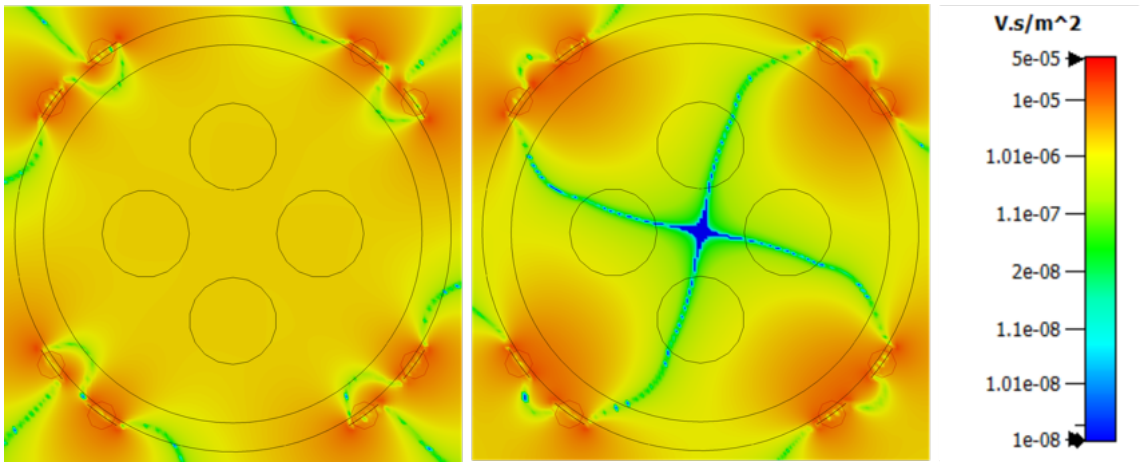


**Figure 31:** Fullport RF-field simulation of the four-element phased-array coil (see Fig. 21) with four water tubes as load at 279.5 MHz, the Larmor frequency of $^{19}$F. The view is a central axial slice of the field distribution. The left (right) image depicts the $B_1^+$ ($B_1^-$) field distributions. The colorbars show the field strength in Vs/m$^2$ in a logarithmic representation.

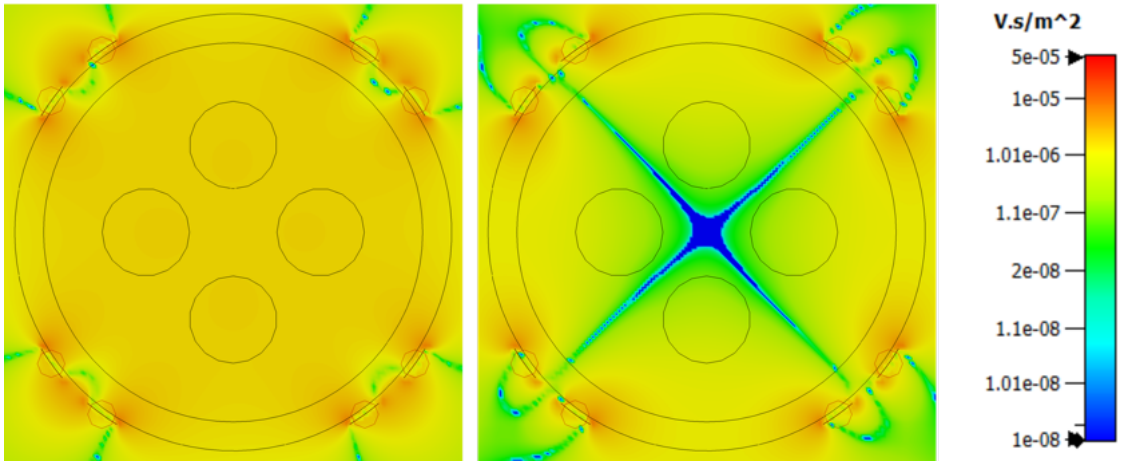


**Figure 32:** Fullport RF-field simulation of the four-element phased-array coil (see Fig. 21) with four water tubes as load at 297.2 MHz, the Larmor frequency of $^{1}$H. The view is a central axial slice of the field distribution. The left (right) image depicts the $B_1^+$ ($B_1^-$) field distributions. The colorbars show the field strength in Vs/m$^2$ in a logarithmic representation.

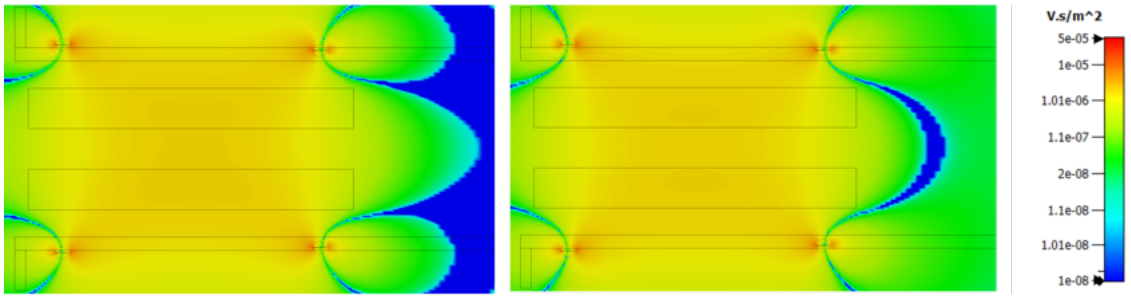


**Figure 33:** Fullport RF-field simulation of the four-element phased-array coil (see Fig. 21) with four water tubes as load. The view is a central saggital slice of the field distribution. The left (right) image depicts the $B_1^+$field distributions at $^{19}$F($^{1}$H) resonance frequencies. The colorbars show the field strength in Vs/m$^2$ in a logarithmic representation.

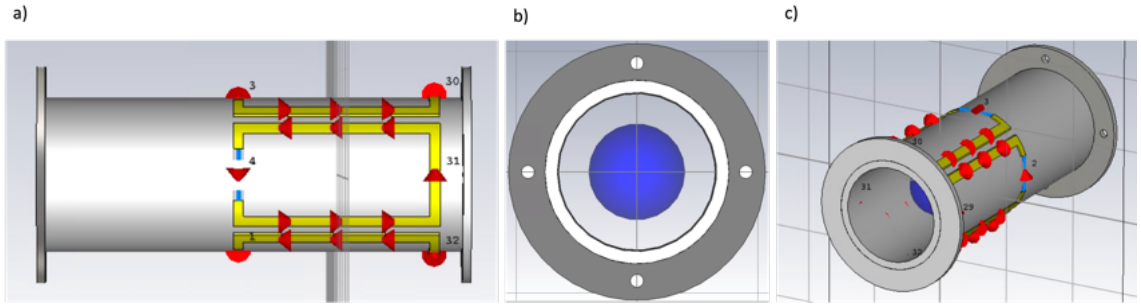


**Figure 34:** Modelling of the four-element phased-array coil (comparable with Fig. 21) filled by 4 cm diameter spherical phantom a) Side view; b) front view; c) perspective view. All capacitances and circuits were designed as ports and later on filled by a function.

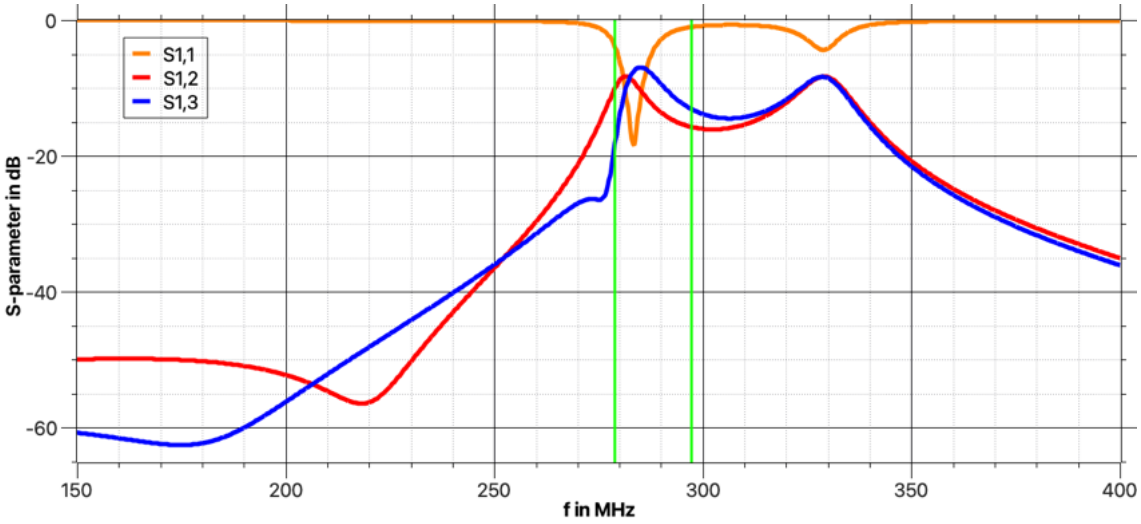


**Figure 35:** S-parameters for the four-element phased-array coil (see Fig. 26) with a spherical phantom as load. Three S-parameters were listed as examples, which are identical to the others due to the symmetry. Here, S1,1 applies to the reflection parameters S1,1; S2,2; ... The coupling parameters for the nearest neighbors S1,2; S1,4; S2,3; ... are also identical. The reflection parameters of the opposite elements S1,3; S2,4; ... are then the last category accordingly. The green lines mark the resonance frequencies of $^{19}$F (279.5 MHz) and $^{1}$H (297.2 MHz).

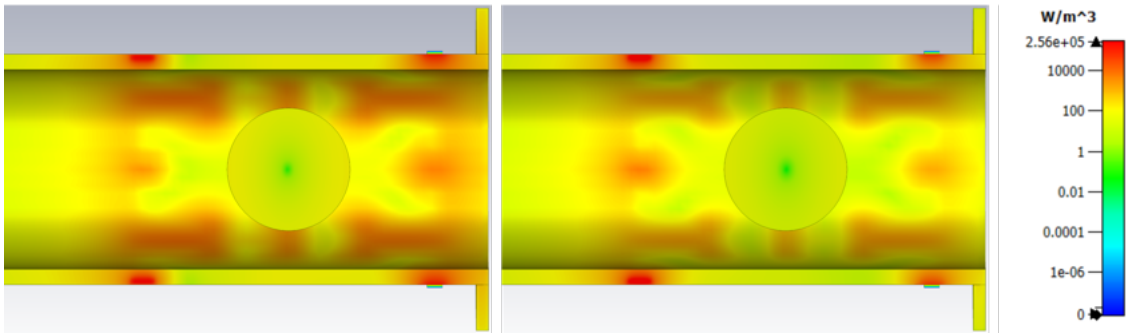


**Figure 36:** Loss-field simulation results for a fullport simulation of the four-element phased-array coil (see Fig. 34)filled with a spherical phantom. The view is a central saggital slice of the field distribution. The left side shows the loss-results for 279.5 MHz, the Larmor frequency of $^{19}$F. The right side shows the loss-results for 297.2 MHz, the Larmor frequency of $^{1}$H. The colorbars show the field strength in W/m$^3$ in a logarithmic representation.

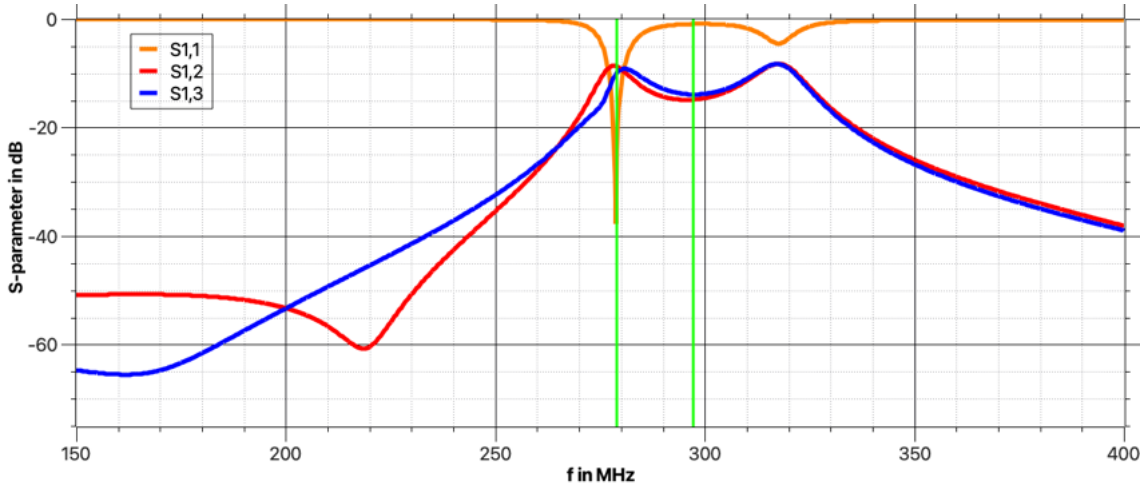


**Figure 37:** S-parameters for the four-element phased-array coil (see Fig. 34) with a spherical phantom as load after retuning and rematching. Three S-parameters were listed as examples, which are identical to the others due to the symmetry. Here, S1,1 applies to the reflection parameters S1,1; S2,2; ... The coupling parameters for the nearest neighbors S1,2; S1,4; S2,3; ... are also identical. The reflection parameters of the opposite elements S1,3; S2,4; ... are then the last category accordingly. The green lines mark the resonance frequencies of $^{19}$F (279.5 MHz) and $^{1}$H (297.2 MHz).

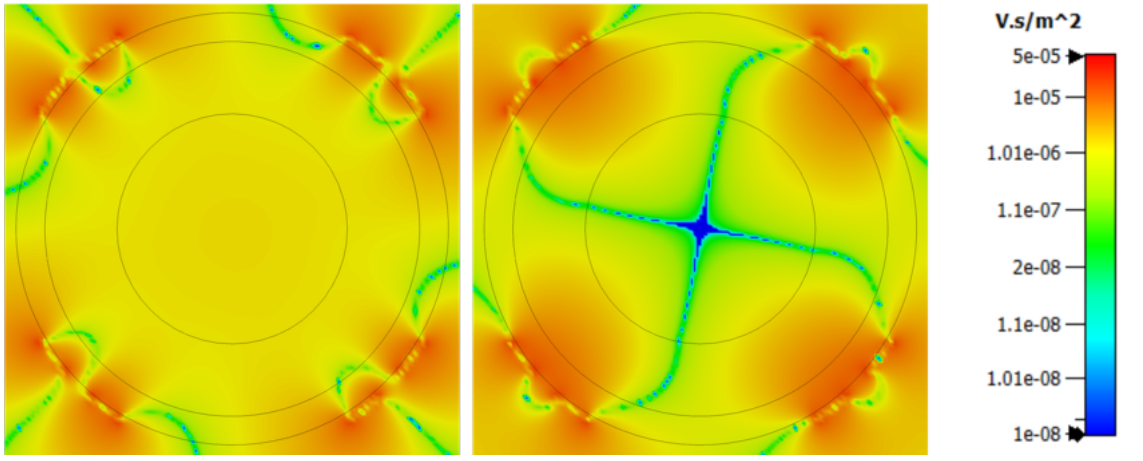


**Figure 38:** Fullport RF-field simulation of the four-element phased-array coil (see Fig. 34) with spherical phantom as load at 279.5 MHz, the Larmor frequency of $^{19}$F. The view is a central axial slice of the field distribution. The left (right) image depicts the $B_1^+$ ($B_1^-$) field distributions. The colorbars show the field strength in Vs/m$^2$ in a logarithmic representation.

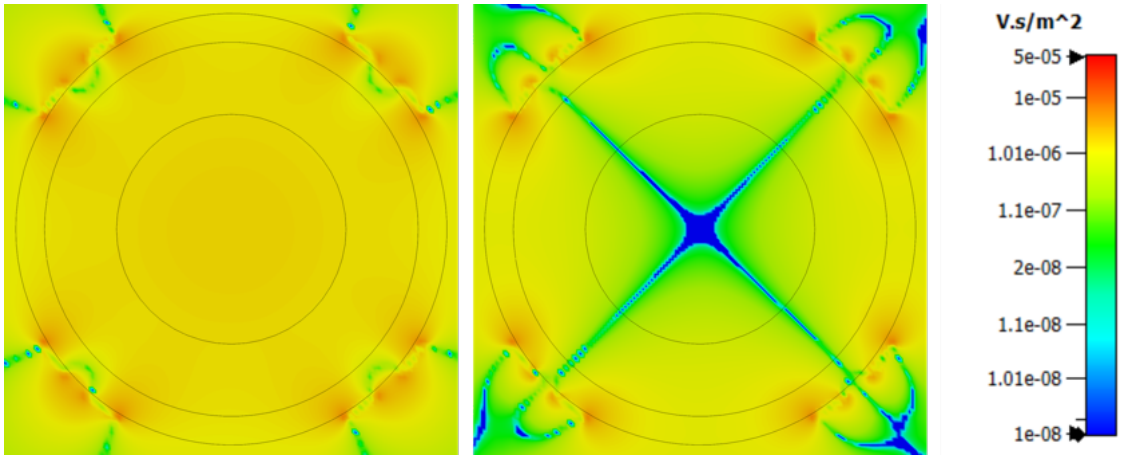


**Figure 39:** Fullport RF-field simulation of the four-element phased-array coil (see Fig. 34) with spherical phantom as load at 279.5 MHz, the Larmor frequency of $^{1}$H. The view is a central axial slice of the field distribution. The left (right) image depicts the $B_1^+$ ($B_1^-$) field distributions. The colorbars show the field strength in Vs/m$^2$ in a logarithmic representation.

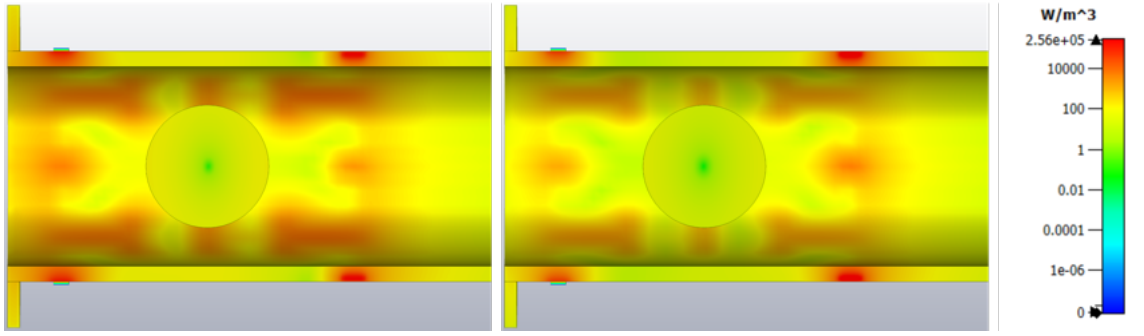


**Figure 40:** Fullport RF-field simulation of the four-element phased-array coil (see Fig. 34) with a spherical phantom as load. The view is a central saggital slice of the field distribution. The left (right) image depicts the $B_1^+$field distributions at $^{19}$F($^1$H) resonance frequencies. The colorbars show the field strength in Vs/m$^2$ in a logarithmic representation.

of the $B_1^+$ fields were shown here for the $^{19}$F and $^1$H resonance frequency in Fig. 41.

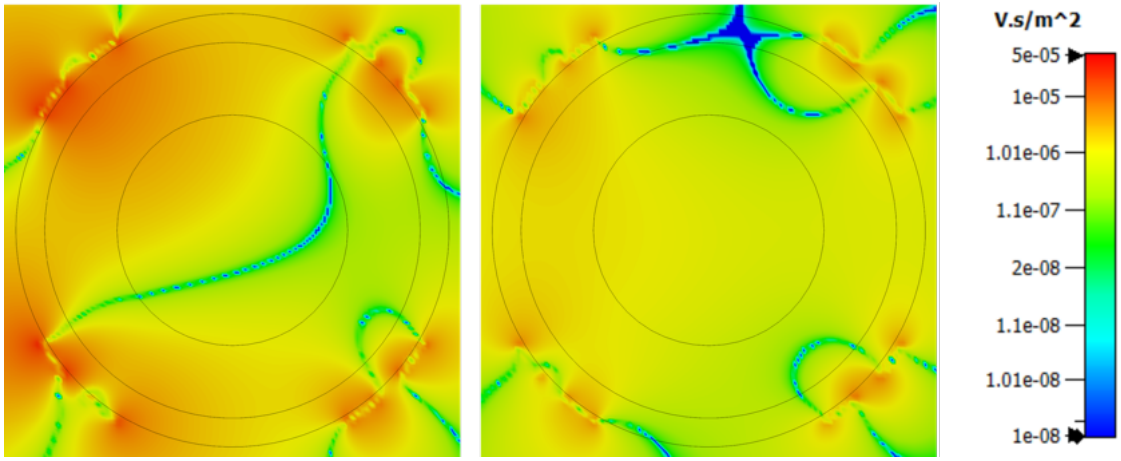


**Figure 41:** Single port RF-field simulation of the four-element phased-array coil (see Fig. 34) with spherical phantom as load. The view is a central axial slice of the field distribution. The left (right) image depicts the $B_1^+$field distributions at $^{19}$F($^1$H) resonance frequencies. The colorbars show the field strength in Vs/m$^2$ in a logarithmic representation.

Finally, an MRI coil was developed and simulated, which had a significantly larger diameter (22 cm) and was also longer (30 cm). The background here was that the previous coil was kept relatively small as a proof-of-principle, while human test subjects or their body parts did not fit into it. The aim here was to construct a coil that had the design of the four-element coil but used the larger dimensions. To achieve this, the same concept of capacitive decoupling was used, but applied to a coil with eight elements (see Fig. 42). This coil was also adapted to the load accordingly and a $B_1^+$ field distribution was simulated for $^1$H and

$^{19}$F. As shown in Fig. 43, a homogeneous field distribution could also be achieved in this case.

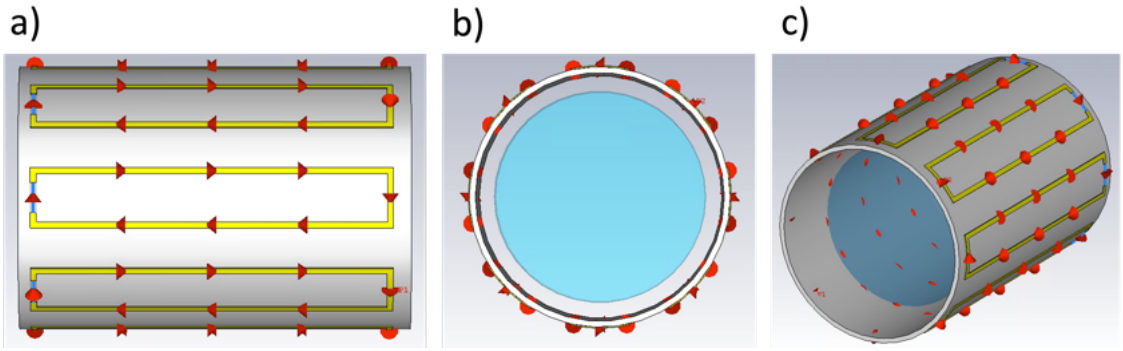


**Figure 42:** Modeling of the eight-element phased-array coil filled with a cylindrical phantom with a diameter of 18 cm. Outer diameter of the coil: 22 cm length: 30 cm. a) side view; b) perspective view; c) front view. All capacitances and circuits were designed as ports and later filled with a function.

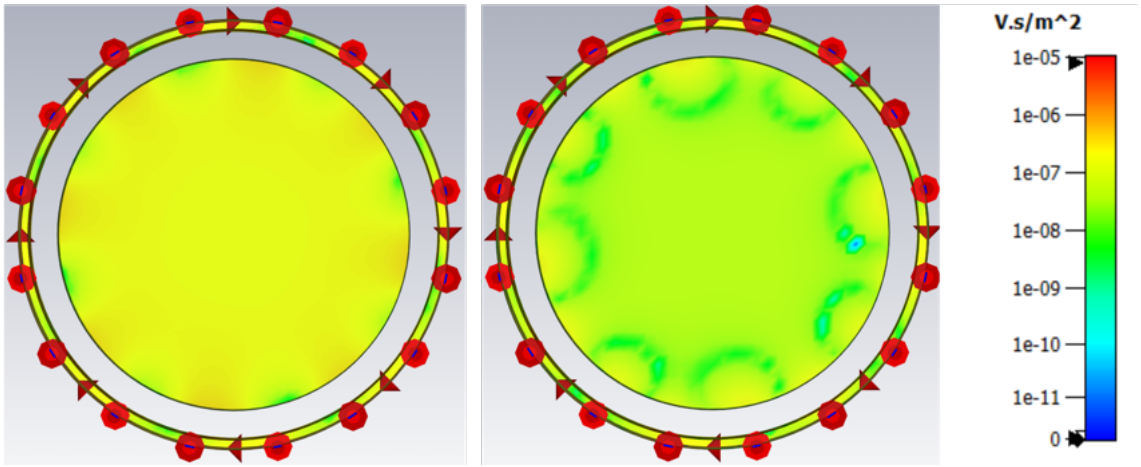


**Figure 43:** Results of the RF field simulation for a single port simulation of the eight-element phased-array coil (see Fig. 42) with cylindrical phantom as load. The view is a central axial section of the field distribution. The left (right) image shows the $B_1^+$ field distributions at $^{19}$F($^{1}$H) resonant frequencies. The color bars show the field strength in Vs/m$^2$ in a logarithmic representation.

### 3.4.2 Hardware of a Phased-Array Coil

Based on the results of the field simulations, the four-element coil was finally designed and built. As can be seen in Fig. 44, the coil was built according to the model of the simulation in Fig. 21. First, the housing was exported from the simulation into a .stl format and adapted accordingly for an UltiMaker 2+ 3D printer using the UltiMaker Cura software

(`https://ultimaker.com/`, UltiMaker,Utrecht, Netherlands). This was then printed exactly as in the simulation. A prefabricated conductor track was used for the copper lines, which had corresponding gaps in which the lumped elements, i.e. the capacitors in this case, could be soldered. In addition, the middle capacitors were connected to two capacitors of the neighboring elements in order to create a capacitive decoupling, as used in the simulation.

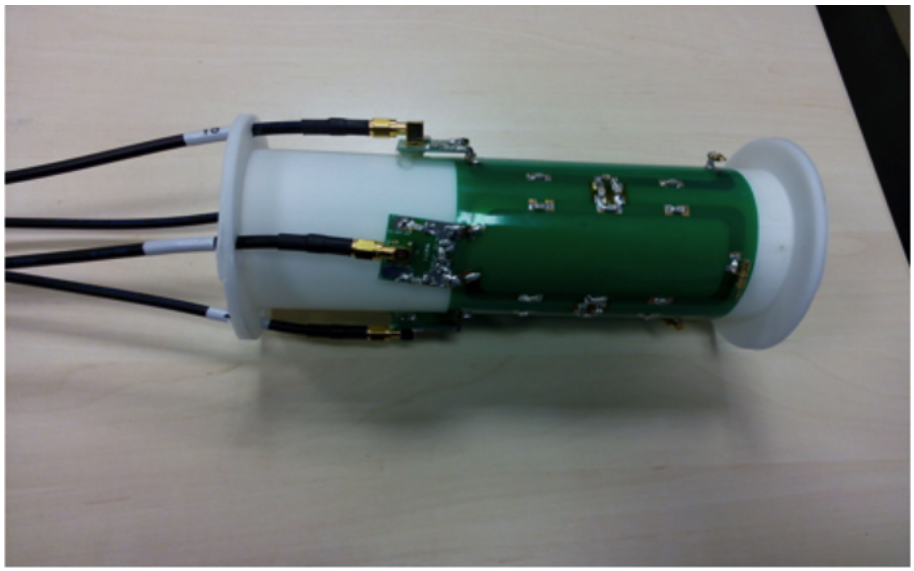

**Figure 44:** Picture of the constructed four-element MRI coil. A prefabricated conductor track with gaps for the lumped elements was glued onto the 3D-printed PLA housing. Capacitances were inserted into all gaps that were optimal for an optimal matching of the S-parameters (Fig. 23) to the Larmor frequency of $^{19}$F. A tuning and matching network was implemented on a small glass fibre pad, which was then soldered to the lower area using copper strips and forms the connection to the coaxial cable.

The tuning and matching network was realized on a separate pad and then an K (Sub-Miniature version A) connector was soldered on to connect the coaxial cables. Adjustable capacitors were soldered to the capacitors opposite to be connected in order to compensate for slight fluctuations in the design. Similar to the simulations, the aim here was also to tune and match the network to the Larmor frequency of $^{19}$F. This resulted in slightly different values for the respective capacitances compared to the simulation:

- Matching capacitances $C_m = 15\,\mathrm{pF}$,
- Mixed tuning and matching capacitances $C_{tm} = 8.2\,\mathrm{pF}$,
- Decoupling capacitances $C_k = 10\,\mathrm{pF}$,
- Capacitances on the opposite side the ports $C_o = 14\,\mathrm{pF}$,
- Remaining capacitances in the network $C_a = 15\,\mathrm{pF}$.

The corresponding S-parameters can be seen in Fig. 45. These were measured using a FieldFox network analyser from Keysight (Santa Rosa, California, USA). As only two channels were available, several measurements were carried out and the other channels were each terminated with a 50 Ω resistor.

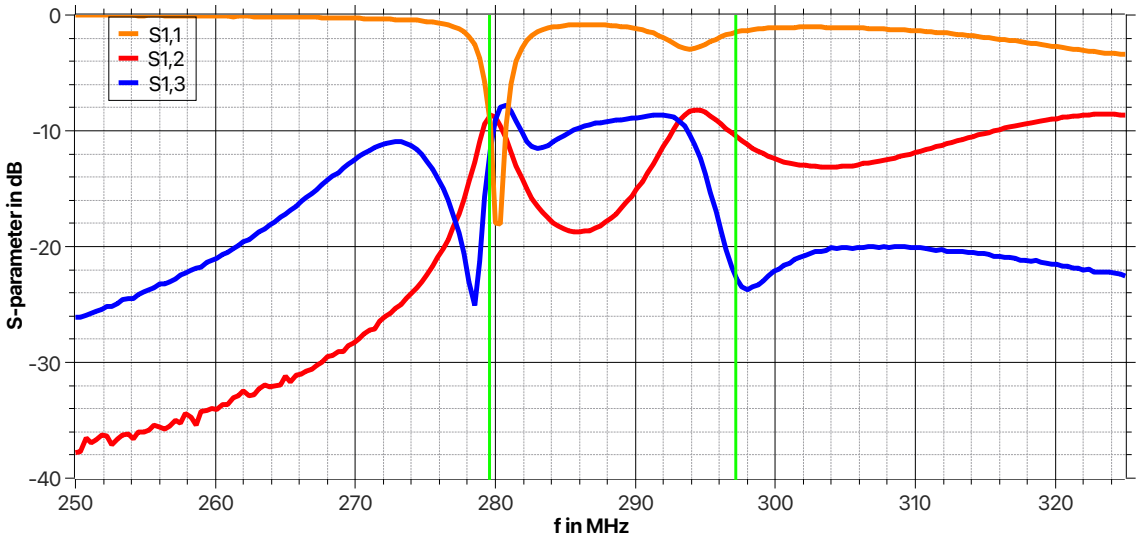


**Figure 45:** Measured S-parameters for the four-element MRI coil filled with a TFE bottle phantom (Fig. 47). As many S-parameters are very similar and 16 S-parameters would severely limit the clarity, three S-parameters for the following groups are listed here as examples: S1,1 parameters for the reflection parameters (S1,1; S1,2; ...); S1,2 parameters for the coupling parameters to the nearest neighbours (S1,2; S1,3; S2,3; ...) and S1,3 parameters for the coupling parameters to the next but one neighbour (S1,3; S2,4; ...).

As some of the values of the capacitances had to be adjusted again for the simulation, a simulation was also carried out again with the values specified above in order to be able to estimate the extent of the influence on the simulated S-parameters and thus better assess the validity of the simulation. The results of this S-parameter simulation are shown in Fig. 46.

Now that the coil had been constructed, a box was built containing the transmit-receive unit. Firstly, the four coaxial cables were routed to the box and led to a board of transmit-receive switches with included preamplifiers (Fig. 8). The outputs of the receive side were then passed to the control unit of the 7 Tscanner for signal processing, while the input side for the RF pulse was still routed via cables of different lengths. RG402 semi-rigid cables were cut in such a way that they produced a phase shift of 0°, 90°, 180° and 270° for the frequency of 279.56 MHz (i.e. Larmor frequency of $^{19}$F), which corresponds to a length of 100 mm (reference length), 286.3 mm, 472.6 mm and 658.9 mm.

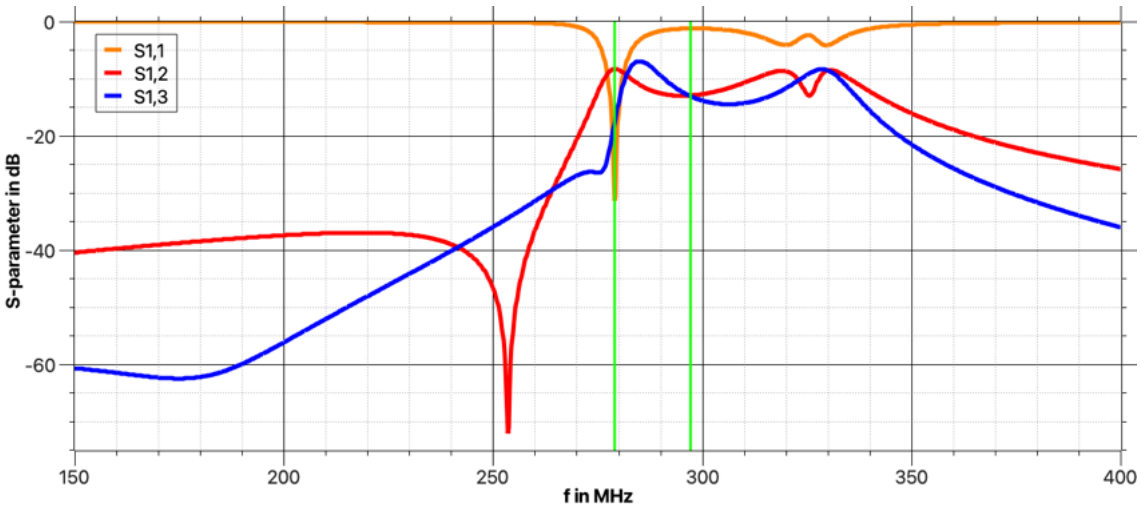


**Figure 46:** S-parameters for the four-element phased-array coil (see Fig. 21) filled with a cylindrical phantom and with the capacitance values from the real fitting of the constructed MRI coil. As an example, three S-parameters were listed, which are identical to the others due to symmetry, where S1,1 applies to the reflection parameters S1,1; S2,2; ... The coupling parameters for the nearest neighbours S1,2; S1,4; S2,3; ... are also identical. The reflection parameters of the opposite elements S1,3; S2,4; ... are then the last category accordingly. The green lines mark the resonance frequencies of $^{19}$F (279.5 MHz) and $^{1}$H (297.2 MHz).

# 4 Imaging Experiments at 7 T MRI

## 4.1 Design of Phantoms

Different phantoms were used for the measurements on the Siemens 7 T MRI in order to utilize their respective advantages and disadvantages, which will be briefly presented here so that they can be referenced accordingly in the following chapters.

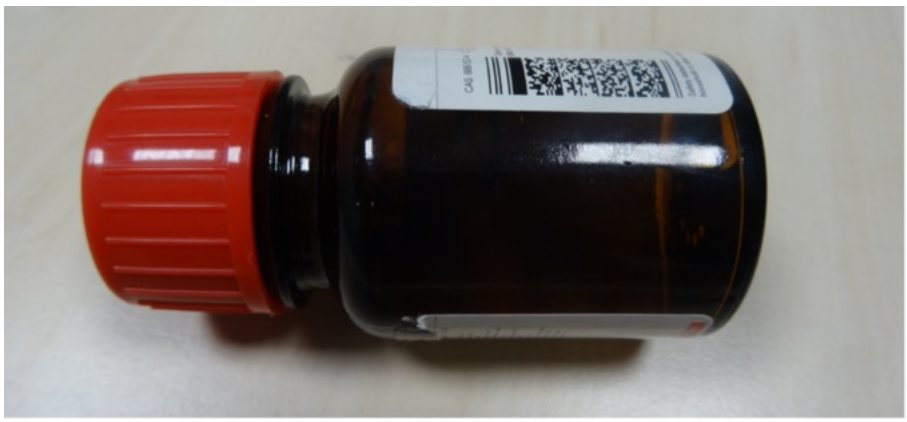

**Figure 47:** Bottle phantom with pure substance.

Initially, simple sample vials containing respective pure substance were used for the first simple demonstrations of the possibility of measurement (Fig. 47). This had the great advantage that the substance could be used inexpensively for the first experiments without it being "consumed". Nevertheless, there were problems with shimming and positioning due to various bends in the glass.

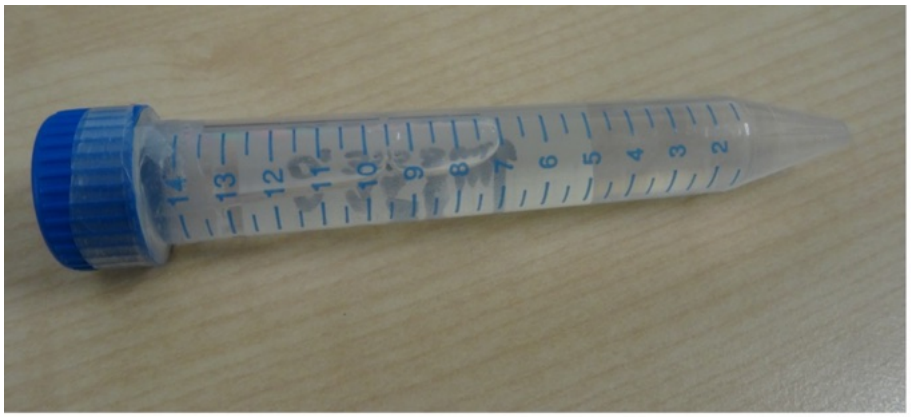


**Figure 48:** Cylindrical phantom (Falcon$^{TM}$ tube) sealed with parafilm.

For this reason, the substance to be measured, usually dissolved in water, was filled into Falcon$^{TM}$ tubes, which were additionally sealed with Parafilm (Fig. 48). When using these

tubes as a phantom, the resulting air bubble at the top always proved to be a problem. To counter this, the phantom was usually fixed into the coil at a slight angle, which had the advantage that no air bubble could be seen in the imaging layer if possible.

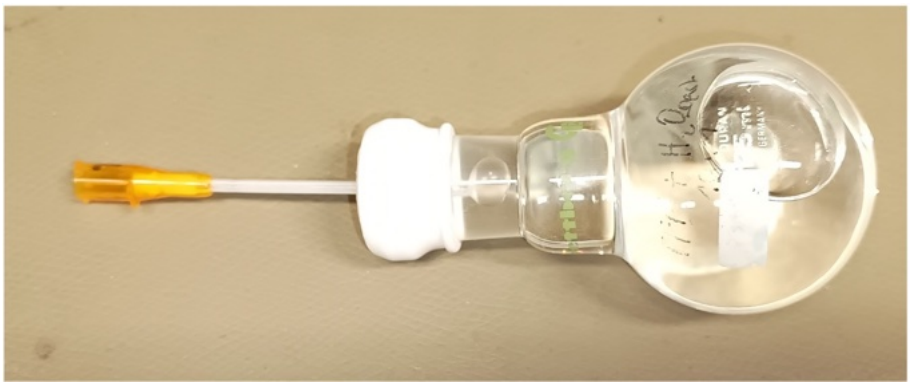

**Figure 49:** Spherical phantom (40 mm diameter) sealed with a septum. Insertion nozzle for a fiber optic using a cannula.

Another way to avoid this problem was to use an NMR sample tube (Fig. 50). Due to the thickening at the upper end, this had the advantage that the air bubble was located in the front area and a long area was available for homogeneous imaging.

**Figure 50:** Cylindrical phantom (10 mm diameter) using a NMR sample tube sealed with septum.

However, both the NMR sample tube and the Falcon$^{TM}$ tubes have the disadvantage that, if they are contained in the coil alone, relatively little volume of the coil is filled. In order to overcome this issue and at the same time to change to a spherical shape, a round bottom flask was used, which could be closed with a septum (Fig. 49). Up to 35 mL could be filled into this. Here, too, the problem of a possible air bubble arose, so that the filler neck was always turned slightly upwards if possible. Nevertheless, it was often impossible to avoid the air bubble being contained in the imaging layer. Another advantage of both the NMR tube and the round bottom flask is that both can be sealed with a septum, which in turn means that well-sealed fiber optics can be inserted, which can be used for temperature determination.

Finally, a multi-chamber phantom was constructed (Fig. 51). For this purpose, a sphere as large as possible was shaped to fit the coil housing and supplemented with retaining plates

so that the sphere is firmly fixed in the coil housing. A second bottle-shaped chamber was then constructed inside the sphere to create a separate area that can be filled with a different substance or concentration. Finally, the opening could be closed with simple plugs.

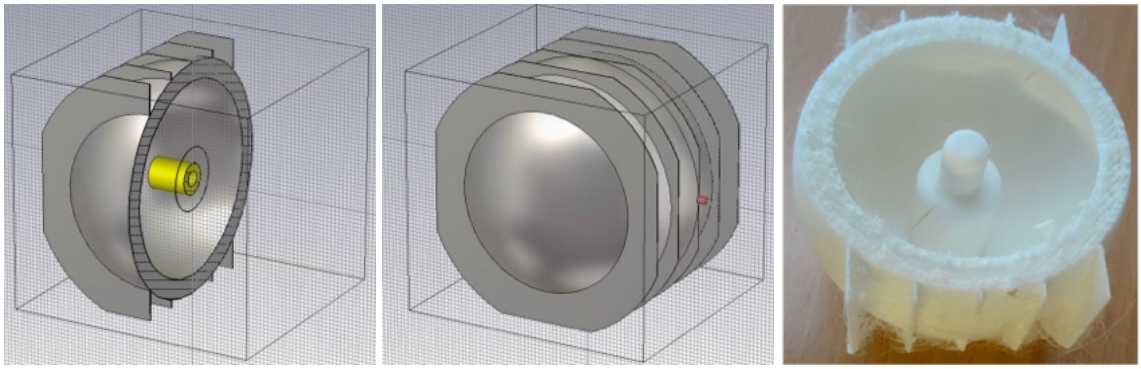

**Figure 51:** Printing and construction of a 3D-printed multi-chamber phantom. On the left, a section through the phantom with both chambers, in yellow the small inner chamber, which can be filled from the outside via an access port. In the center is the complete external view with the holding ribs to hold the phantom in the phased-array coil. On the right in the picture the half-finished printed phantom.

## 4.2 Results for Surface Coil and Four-Element Phased-Array Coil

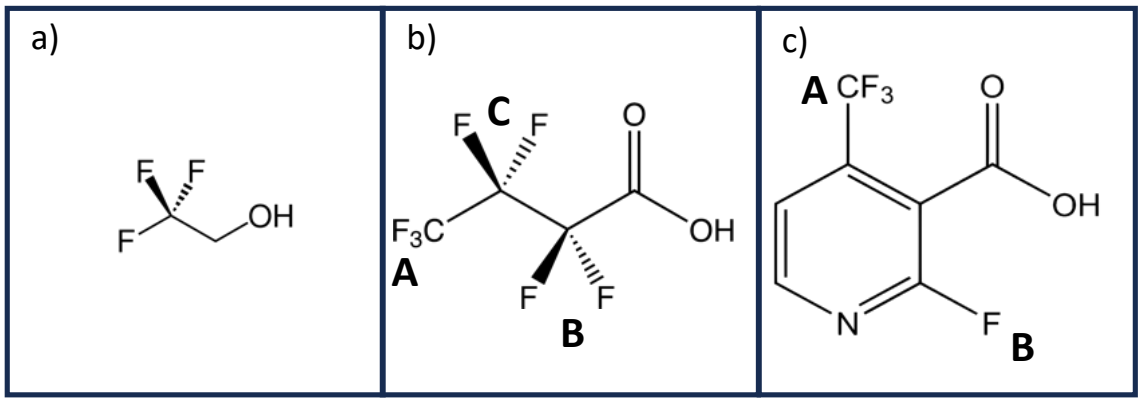


**Figure 52:** Molecular structures of the fluorinated molecules investigated in this study. a) 2,2,2-Trifluoroethanol; b) heptafluorobutyric acid with its three fluorinated groups, the $CF_3$-group A, and the $CF_2$-groups B and C; c) 2-fluoro-4-(trifluoromethyl)nicotinic acid with its two fluorinated groups, the $CF_3$-group A and the CF-group B.

Both the surface coil and the four-element volume coil were used for imaging in the 7 MRI. 3D-printed mounts were attached to the patient table. The phantoms were then positioned

as centrally as possible in the coil and fixed with pads or, in the case of the surface coil, fixed with adhesive tape. The two coils were also connected identically in principle. First, the transmit/receive switch boxes with their preamplifiers were connected to the 7 T MRI system. The one-channel system was used for the surface coil, while the four-channel system was used for the phased-array coil. The coils were then connected to these boxes accordingly.

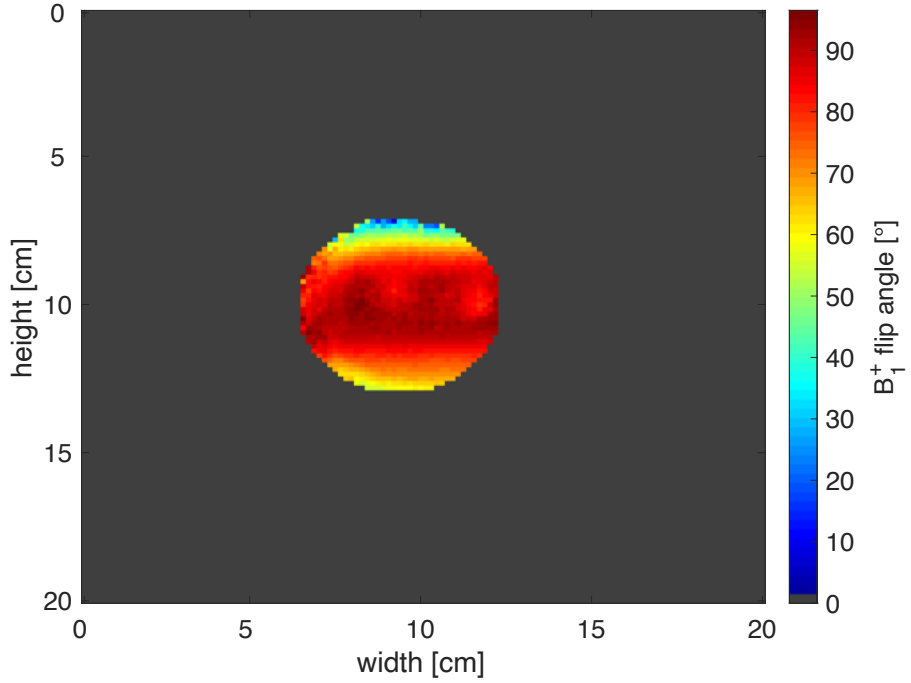


**Figure 53:** $B_1^+$ imaging of a surface coil with a bottle phantom. Image size: 128x128, slice thickness 8mm, FoV: 115 x 115 $mm^2$, TE: 2.06 ms, TR: 5000 ms. The noise around the phantom has been masked for better recognizability.

First, comparative measurements were carried out with the $B_1^+$ fields from the simulation. A $B_1^+$ flip angle mapping sequence was used for this (Siemens work in progress package). This was based on a turbo FLASH (Fast Low-Angle Shot) sequence, with a magnetization preparation pulse to determine the flip angle distribution. [57], [58] To determine the $B_1^+$ flip angle maps in the FoV, the flip angle $\alpha$ of the preparation pulse had to be in the range between 45° and 90°. This reduced the noise-related measurement error to a minimum. A rectangular preparation saturation pulse was used to reduce the longitudinal magnetization $M_z$, which helped to determine the flip angle more accurately. The $B_1^+$ flip angles measured by this sequence were stored as gray values corresponding to 10 times the nominal flip angle. This recording method is faster than the spin-echo or stimulated-echo method for determining the $B_1^+$ flip angle.[59] The excitation pulse angles $\alpha_{exc}$ and the preparation pulse angles $\alpha$ are related to the root mean square (RMS) amplitude of the reference voltage $U_{ref}$. Here, the reference voltage $U_{ref}$ characterizes the RF energy required to achieve a 180° flip angle. This 180° reference flip angle is generated by a $B_1^+ = 11{,}75\,\mu$T formed by a pulse period of $t_P = 1$ ms.[60] Especially for *in vivo* MR images,

a valid reference voltage $U_{ref}$ is indispensable for diagnostically useful contrast weighting.[61]

Since no $B_1^+$ flip angle mapping sequence was available for $^{19}F$ and the source code for a $^1H$ flip angle mapping sequence that could have been matched to $^{19}F$ was not available, only the $^1H$ measurement was performed to validate the field simulation results and it was assumed that corresponding maps were also valid for $^{19}F$. The results of the measurement with the bottle phantom (Fig. 47) filled with trifluoroethanol (2,2,2-trifluoroethanol, Sigma-Aldrich, TFE; Fig. 52a) are shown in Fig. 53 for the surface coil and with the sphere phantom (Fig. 49) filled with 686 mM TFE in Fig. 54 for the volume coil.

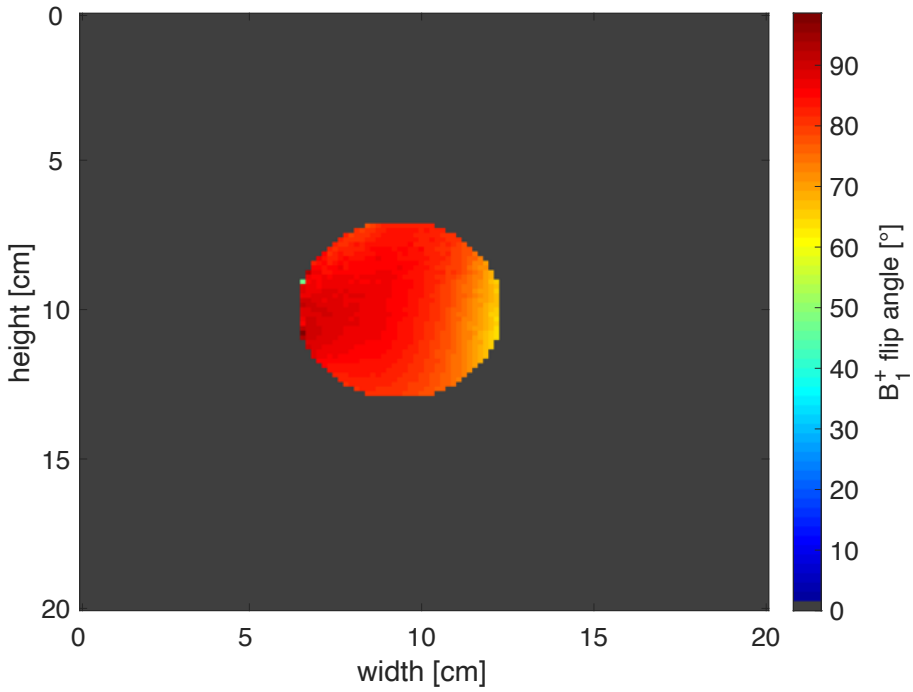


**Figure 54:** Measured $B_1^+$-flipanglemap of a four-element coil with a sphere phantom filled with TFE. The FLASH based flip angle mapping sequence had following parameter: image size: 128x128, slice thickness 8mm, FoV: 115 x 115 mm$^2$, TE: 2.06 ms, TR: 5000 ms. The noise around the phantom has been masked for better recognizability.

For a first fast acquisition with the surface coil, a ultra-short echo-time (UTE) sequence ([62]) was adapted to $^{19}F$ and used to show that $^{19}F$ imaging with the surface coil is possible. The phantom used was the upright bottle phantom filled with pure TFE (Fig. 47). The following measurements shown here, on the other hand, all deal with the volume coil, as this was the aim of this work.

In order to experimentally demonstrate the possibility of both $^{19}F$ and $^1H$ imaging, a fast low-angle shot sequence commonly used in clinical applications was used.[57] This is based

on a simple gradient-echo sequence, whereby small flip angles are used in the excitation pulse to allow very fast repetition of the experiment. Using the source code in the Siemens IDEA environment, the standard $^{1}$H FLASH sequence was adapted to the $^{19}$F Larmor frequency so that it is consequently suitable for fluorine and proton imaging.

**Figure 55:** $^{19}$F imaging in a 7T MRI system using the surface coil and the bottle phantom filled with TFE (Fig. 47). The UTE sequence used had the following parameters: image size: 64 x 64; slice thickness: 1.54 mm; TE: 1.08 ms; TR: 100 ms; FoV: 130 x 130 mm$^2$.

This sequence has shown that a transmit voltage of 120 V for proton imaging and 13.3 V for fluorine imaging are ideal for excitation. At the same time, however, it was also shown that if the repetition times (TR) were too short, the fluorine image exhibited significantly less $SNR$ than with longer ones, which is why a significantly longer TR was required for $^{19}$F imaging than for $^{1}$H imaging. All other sequence parameters were left identical to ensure good comparability of the images. The results of this imaging with the following sequence parameters are shown in Fig. 56 and 57 for the phased-array coil: imaging size: 128 x 128; slice thickness: 3 mm; TE: 4.8 ms; FoV: 80 x 80 mm$^2$ and TR: 200 ms for $^{1}$H imaging and TR: 4000 ms for $^{19}$F imaging.

In addition, experiments were carried out to show the effect on imaging when only individual elements were used for excitation. The results can ultimately be used to estimate the possibilities of a $B_1$ shimming and at the same time to estimate the effects of the failure of individual elements. For this purpose, Fig. 58, the element that is aligned directly downwards was excited using a FLASH sequence. The following sequence parameters were

used: imaging size: 64 x 64; slice thickness: 3 mm; TE: 4.8 ms; FoV: 100 x 100 $mm^2$. TR: 4000 ms for $^{19}F$ and TR: 300 ms for $^{1}H$.

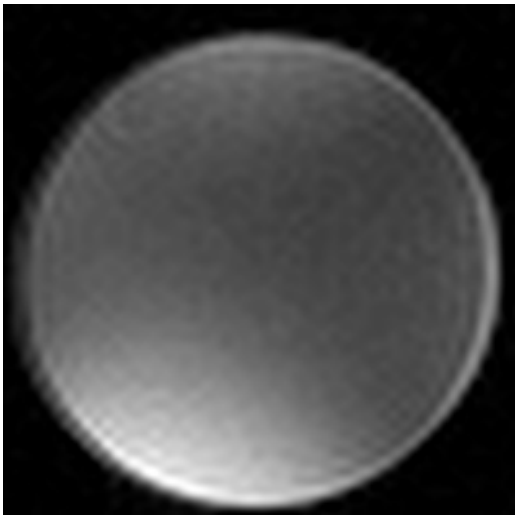

**Figure 56:** $^{1}H$ imaging at 7 T MRI system using the four-element MRI coil (Fig. 44) and the bottle phantom (Fig. 47) filled with TFE. The FLASH sequence had following parameters: imaging size: 128 x 128; slice thickness: 3 mm; TE: 4.8 ms; TR: 200 ms; FoV: 80 x 80 $mm^2$.

In order to measure other substances in addition to TFE, additional experiments were carried out with heptafluorobutyric acid (Sigma-Aldrich, HFBA; Fig. 52b). The special feature here is that it contains various fluorinated groups. This results in up to three signals whose influence on the imaging should be investigated accordingly. Fig. 59 shows that despite the fact that only one sample tube was localized within the coil, two identical images could be detected, which were shifted by 27 px (Pixel) in the frequency encoding direction.

A further test was then carried out with a multi-chamber phantom (Fig. 51). Here, 100 mM TFE was filled into the outer and larger of the two chambers, while $H_2O_{dist.}$ was filled into the inner and smaller chamber. The result of this measurement is shown in Fig. 60. It is noticeable that an $^{19}F$ signal can be seen both inside and outside the small vessel.

Finally, a turbospin echo sequence was tested, which is also widely used in everyday clinical practice, particularly in the differentiation of tissue types. This is ultimately based on the spin-echo phenomenon, which was described by Erwin Hahn. [63] After the 90° pulse, a further 180° refocusing pulse is emitted, which compensates for the signal decay and thus generates an echo. In the turbospin echo sequence, several of these 180° refocusing pulses are sent. Here, too, a standard proton sequence was provided by Siemens and adapted to $^{19}F$ in the IDEA environment. The result of these measurements can be seen in Fig. 61 and 62.

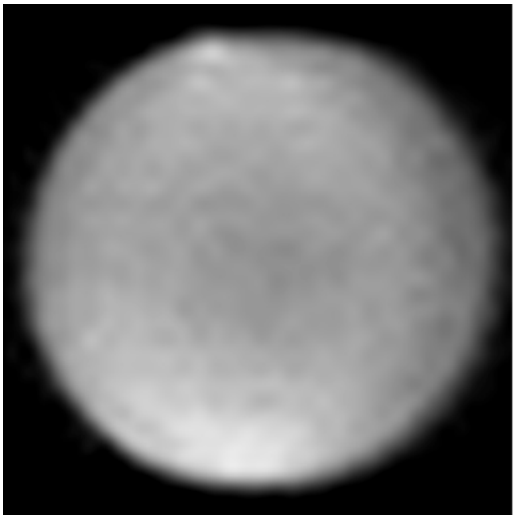

**Figure 57:** $^{19}$F imaging at 7 T MRI system using the four-element MRI coil (Fig. 44) and the bottle phantom (Fig. 47) filled with TFE. The FLASH sequence had following parameters: imaging size: 128 x 128; slice thickness: 3 mm; TE: 4.8 ms; TR: 4000 ms; FoV: 80 x 80 mm$^2$.

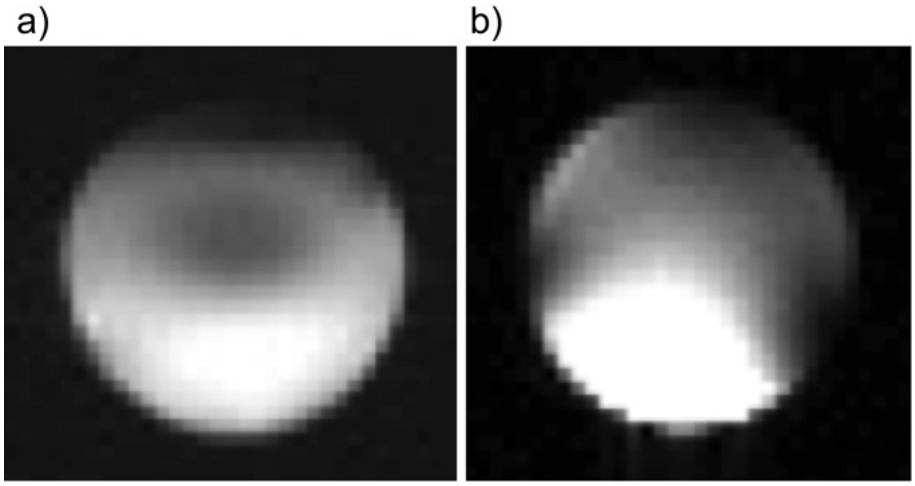


**Figure 58:** Imaging at 7 T MRI system for $^{19}$F/$^{1}$H imaging (left/right) using the four-element MRI coil (Fig. 44) and the bottle phantom (Fig. 47) filled with TFE. Just one channel on the downside was active. a)The $^{19}$F-FLASH sequence had following parameters: imaging size: 64 x 64; slice thickness: 3 mm; TE: 4.8 ms; TR: 4000 ms; FoV: 100 x 100 mm$^2$. b) The $^{1}$H FLASH sequence had following parameters: 64 x 64; slice thickness: 3 mm; TE: 4.8 ms; TR: 300 ms; FoV: 100 x 100 mm$^2$.

**Figure 59:** Imaging at 7 T MRI system for $^{19}$F imaging (left) using the four-element MRI coil (Fig. 44) and one cylindric phantom (Fig. 48) filled by HFBA with a concentration of 120 mm. The two images are shifted by 27 px in frequency encoding direction. The FLASH sequence had following parameters: imaging size: 64 x 64; slice thickness: 2 mm; TE: 9.8 ms; TR: 500 ms; FoV: 100 x 100 mm$^2$.

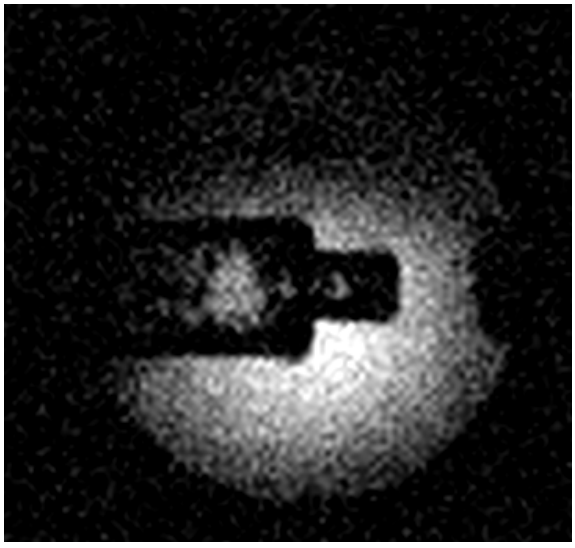

**Figure 60:** $^{19}$F imaging at 7 T MRI system using the four-element MRI coil (Fig. 44) and the two chamber phantom (Fig. 51). The larger chamber, shown here on the right, contains 100 mM TFE, while the smaller of the two is filled with $H_2O_{dist.}$. The FLASH sequence had following parameters: imaging size: 128 x 128; slice thickness: 3 mm; TE: 4.8 ms; TR: 200 ms; FoV: 80 x 80 mm$^2$.

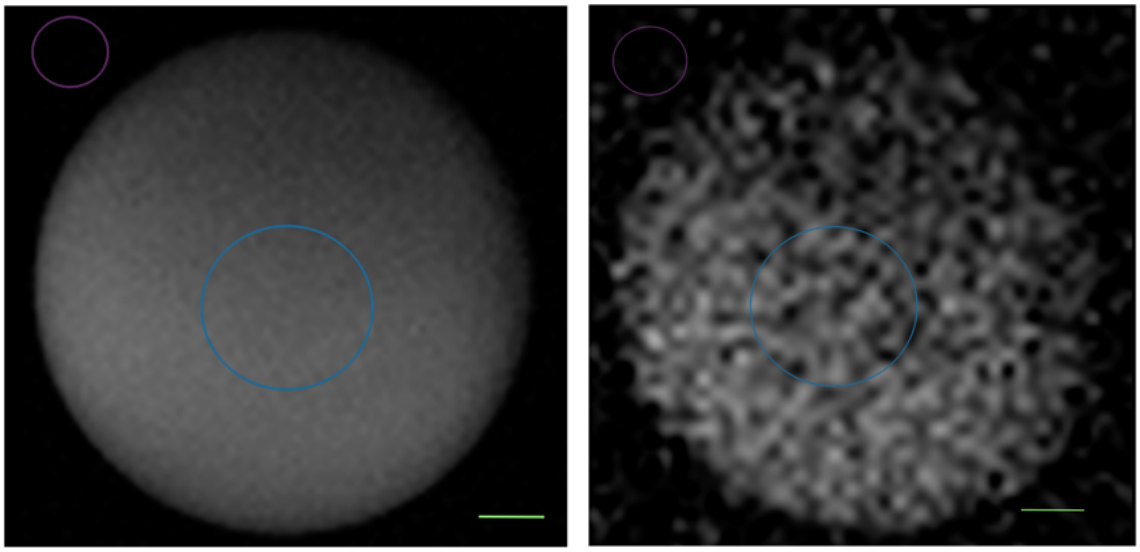

**Figure 61:** $^{19}$F imaging at 7 T MRI system using the four-element MRI coil (Fig. 44) for different TFE concentrations in a spheric phantom. Left/right side shows a concentration of 70 mM/7 mM with an $SNR$ of 18.6/2.5 respectively. The TSE sequence had following parameters: imaging size: 46 x 46; slice thickness: 15 mm; TE: 56 ms; TR: 5000 ms; FoV: 45 x 45 mm$^2$, NA: 32. The circles mark the areas for measuring the $SNR$. At the right lower corner is a 5 mm green line shown.

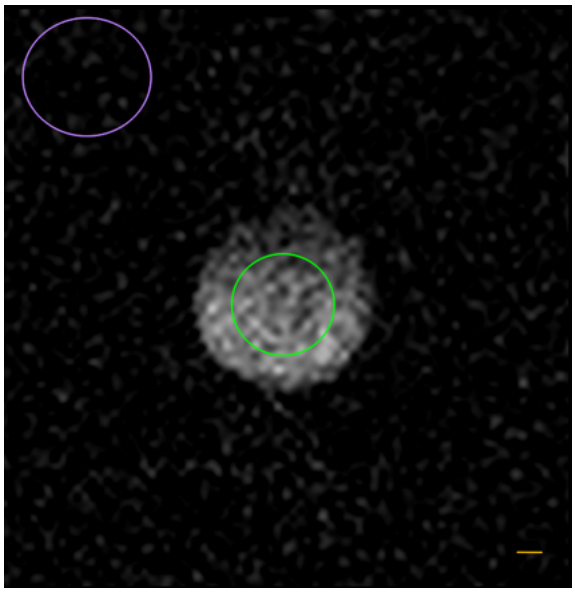

**Figure 62:** $^{19}$F imaging at 7 T MRI system using the four-element MRI coil (Fig. 44) for a concentration of 0.7 mm TFE in a spheric phantom. The TSE sequence had following parameters: imaging size: 78 x 78; slice thickness: 20 mm; TE: 100 ms; TR: 6000 ms; FoV: 119 x 119 mm$^2$, NA: 32. The circles mark the areas for measuring the $SNR$. At the right lower corner is a 5 mm line shown.

As the signal yield per time was particularly high here, this sequence was also used for a concentration series. Images of different concentrations were measured here. With a sub-mm layer resolution, it was still possible to record an image at a TFE concentration of 7 mM with 32 mean values. The $SNR$ was determined by the quotient between a noise measurement at the edge and the mean value of the signal within the phantom. To record a concentration of 0.7 mM, the resolution had to be reduced. Nevertheless, even this sub-mM concentration of TFE could be recorded with a signal-to-noise ratio of about 2.5 and a measurement time of about 4 minutes.

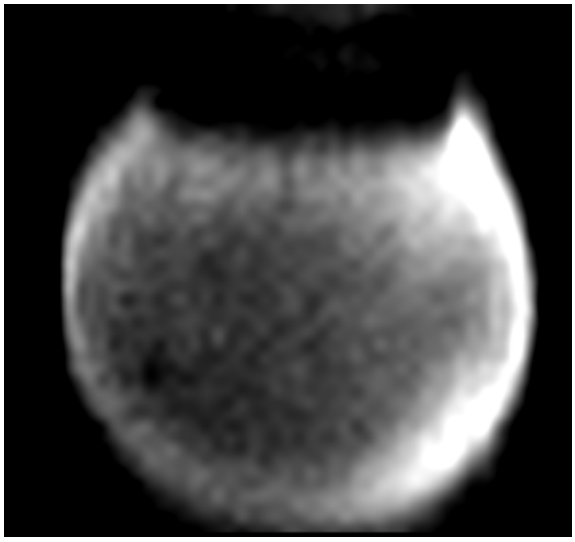

**Figure 63:** $^{19}$F imaging at 7 T MRI system using the four-element MRI coil (Fig. 44) toothpaste (elmex® gelée) in a spheric phantom. The TSE sequence had following parameters: imaging size: 46 x 46; slice thickness: 3.5 mm; TE: 87 ms; TR: 8000 ms; FoV: 45 x 45 mm$^2$, NA: 32.

Motivated by these low concentrations, additional experiments were carried out with the toothpaste elmex® gelée (GABA international AG, Therwil, Switzerland, containing 0.287 g dectaflur, 3.032 g olaflur and 2.21 g sodium fluoride or 1.25 % total fluoride). The gel was poured into a spherical phantom (Fig. 49) and made as bubble-free as possible by shaking. Nevertheless, not all air bubbles could be removed. Shimming was very difficult when measuring this substance. As the exact composition of the toothpaste was not known, the largest signal was used as the reference frequency for imaging. The result, which was achieved with a TSE sequence, can be seen in Fig. 63.

# 5 Temperature-Dependent Measurements with MRI, NMR and MRS

In order to check the spectroscopic behavior of the self-built four-element MRI coil, spectroscopic measurements were performed on the 7 T human MRI scanner and on a Bruker NMR spectrometer (300 MHz proton frequency). This allows the best possible direct comparison of the measurement results due to the very similar field strength. For the measurements at the MRI scanner, an Free Induction Decay (FID) sequence and a Chemical Shift Imaging (CSI) sequence from Siemens were adapted in IDEA environment to the $^{19}$F resonance frequency and used accordingly. The big advantage of the CSI sequence is that the complete volume of the sample does not have to be measured, but a spatially resolved spectroscopy is possible. Its benefit will be explaint in this chapter.

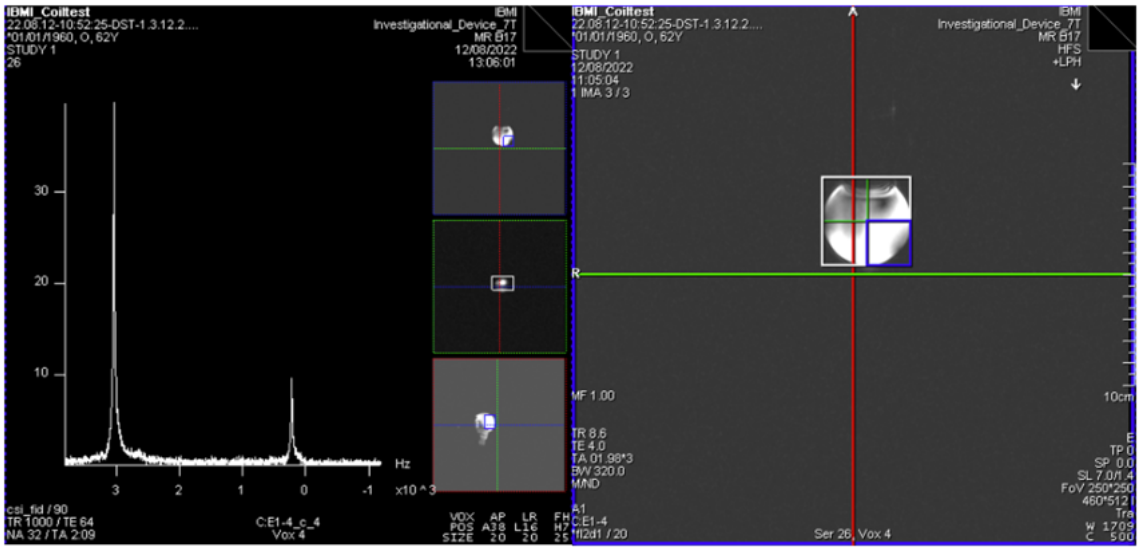


**Figure 64:** GUI (Siemens-Syngo) for acquisition and post-processing CSI measurements for 2-Fluoro-4-(trifluoromethyl)nicotinic acid in isotonic saline solution.

Fig. 64 shows the user interface of the graphical user interface (GUI) of Siemens Syngo viewer, where the corresponding voxel can be selected on the right side and the respective spectrum measured within this voxel is plotted on the left side. In this case it is a spherical phantom following the example of Fig. 49 filled with a solution of 2-fluoro-4-(trifluoromethyl)nicotinic acid dissolved in isotonic saline solution with a concentration of 10 mM.

The same sample was then placed in a 10 mm NMR tube and measured in the Bruker NMR. The result of this measurement is shown in Fig. 65. First of all, both measurements show two signals belonging to the respective fluorinated groups of 2-fluoro-4-(trifluoromethyl)nicotinic acid. The left and higher signal belongs to the $CF_3$ group, while the lower signal belongs to the CF group. The first thing to notice here is that both, the ratio of the amplitudes and the distance of the signals, correlate very well. The exact distance of the signals is

2831.9 Hz in the NMR measurement, while it is 2825.0 Hz in the human MRI. Since it has been noticed in measurements on the NMR spectrometer that the signal difference is very dependent on the temperature, these values show a very good agreement. The measurement on the NMR spectrometer was recorded on a very warm day and thus could not be cooled below 301.1 K, while the measurement in the MRI was performed at a room temperature of about 296 K.

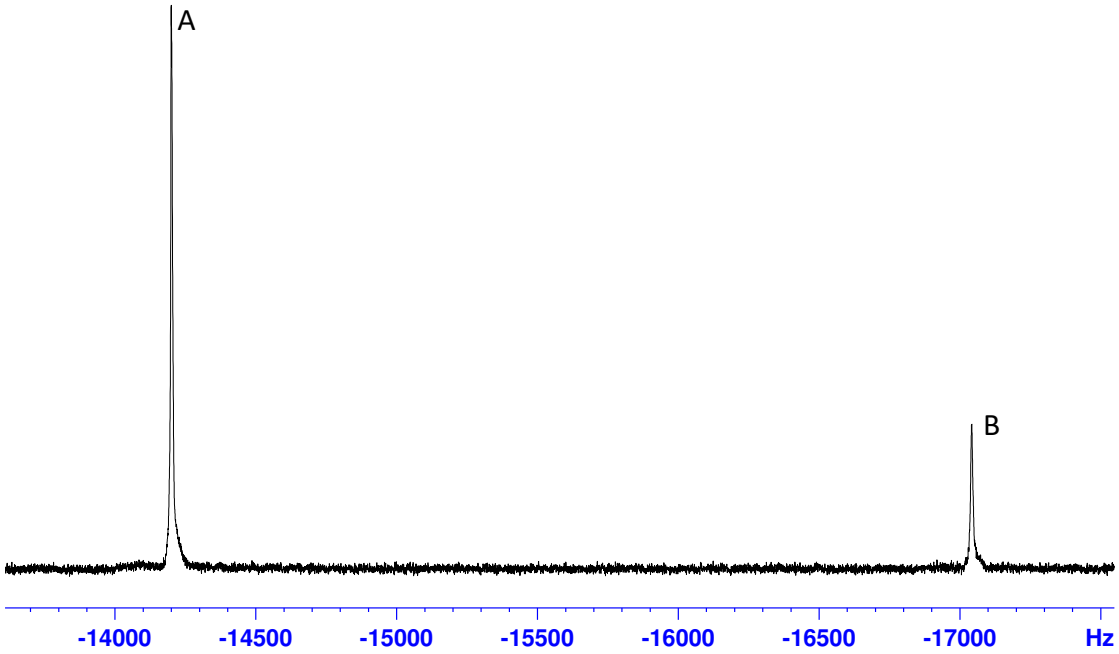


**Figure 65:** Spectrum of 2-fluoro-4-(trifluoromethyl)nicotinic acid in isotonic saline solution by Bruker NMR spectrometer. The Signals to the groups from A and B can be find in Fig. 52.

In order to perform a temperature-independent check of the agreement here, a measurement of trifluoroethanol in a solution with water and a concentration of 694 mM was carried out. As can be seen in Fig. 66, a triplet is formed, which originates from the $CF_3$ group. The splitting and thus the difference of the outer peaks to the middle one results from the ${}^3J_{HF}$-coupling and is consequently temperature independent. In order to measure the largest possible distance, the distance of the two outer peaks was determined for both the NMR measurement and the measurement on the human scanner, which thus corresponds to double ${}^3J_{HF}$-coupling. Here, a distance of 17.5 Hz was determined on the human scanner and a distance of 17.4 Hz on the NMR spectrometer, which represents an excellent agreement.

In addition, the change in the chemical shift of TFE in aqueous solution as a function of temperature was investigated. To obtain the temperature changes, different approaches were used for the two measurement systems.

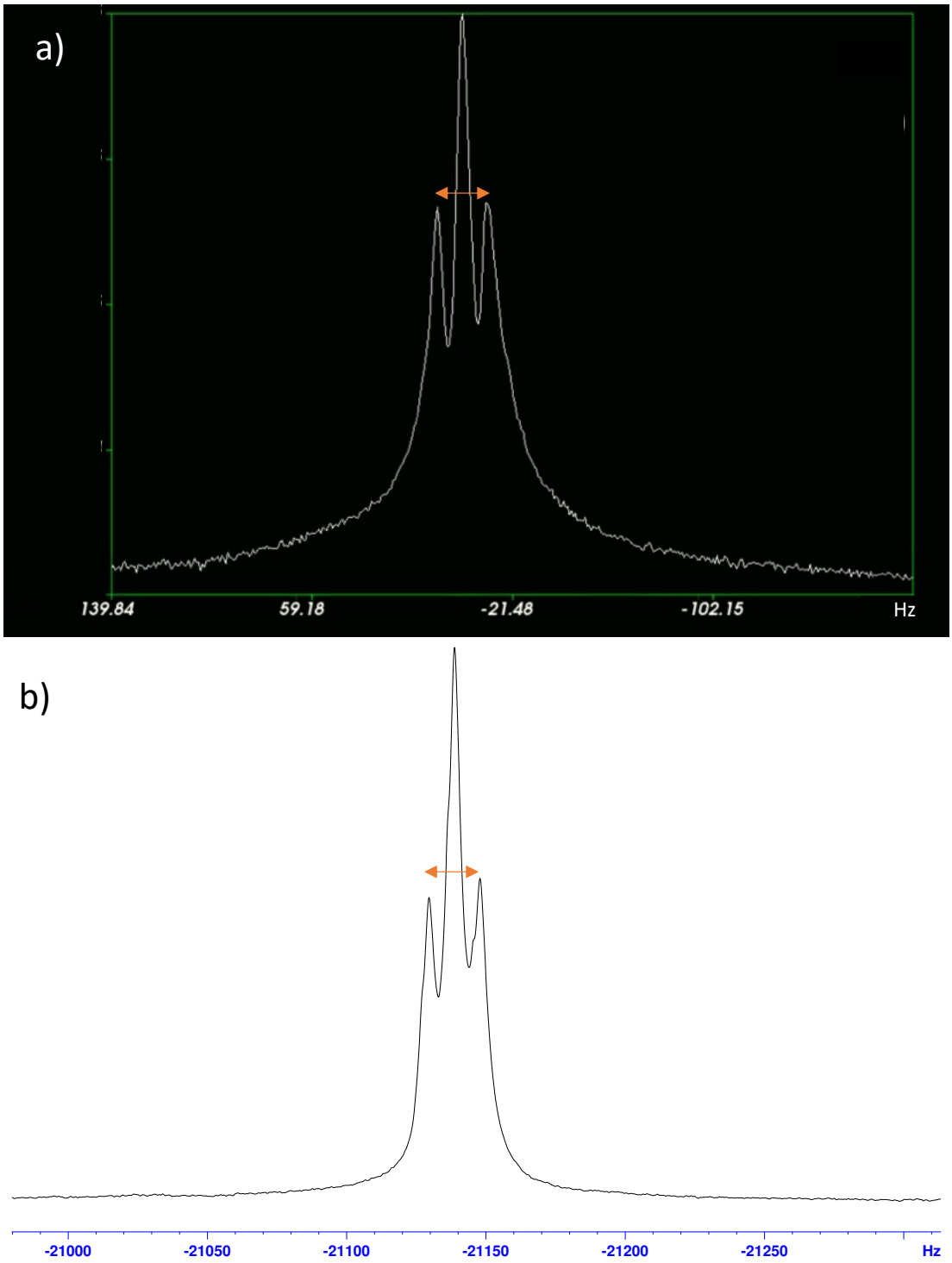


**Figure 66:** Comparison of trifluoroethanol spectra at two different experimental setups. a) Spectrum acquired woth the 7 T MRI scanner and self developed RF coil (CSI sequence). The double J-coupling (the difference between the outer peaks, orange arrow) is 17.5 Hz. b) Spectrum acuired with the Bruker NMR spectrometer (7 T, vendor provided $^{19}$F coil). The $^{3}J_{HF}$-coupling ( half of the distance between the outer peaks, orange arrow, 17.5 Hz) is 8.7 Hz.

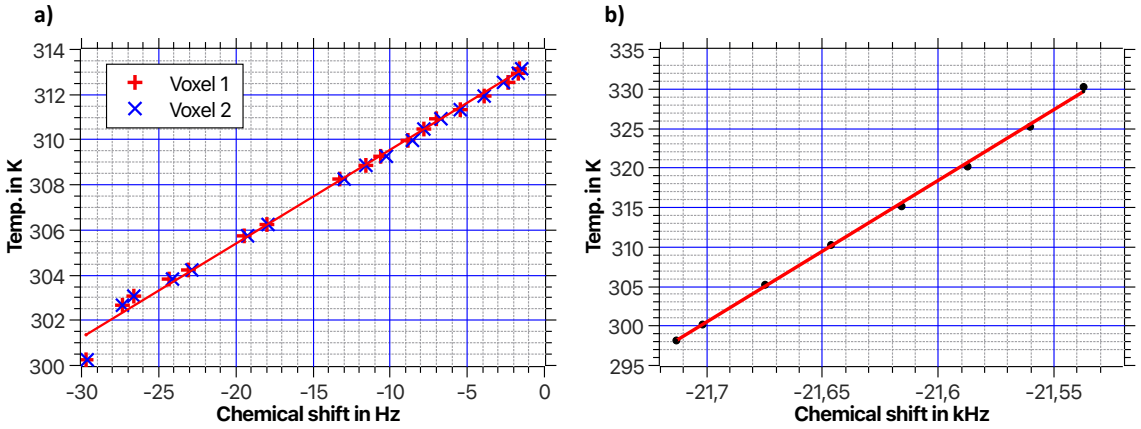


**Figure 67:** Temperature dependency of the $^{19}$F MR signal of trifluoroethanol in aqueous solution in a) MRI and b) NMR. In a), the chemical shift of the spectra within two different voxels of the phantom are shown. The red line depicts a linear fit using SciDAVis.

First, a measurement was carried out on the 7 T MRI. There was no temperature control unit here, which is why the spherical phantom (Fig. 49) was first placed in a warm water bath for a longer period of time so that the internal temperature approached the water temperature. A cannula was then inserted through the septum to introduce a glass fiber, which could later be used for temperature control with a Fotemp 4 (Optocon, `https://comem.com/en/optocon/`, Germany). Due to the influence of the GaAs -Fotemp probes by a strong magnetic field, the temperatures were adjusted by +2.9 K according to [64].

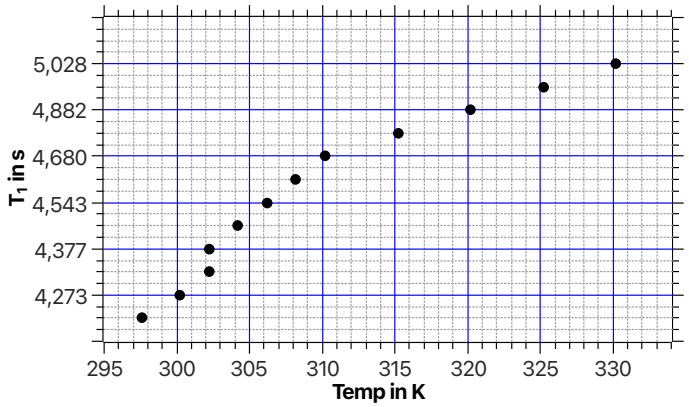


**Figure 68:** Temperature depency of the $T_1$ time for 130 mM TFE in aqueous solution in NMR spectroscopy at 7 T.

The respective frequency of the center of the signal was shown in Fig. 67a as a function of the temperature. It should be noted that the shape of the signal changed due to the changing shim. Two different voxels were plotted in order to compare the reading accu-

racy and to check whether there was a difference between the voxels of the CSI measurement.

The NMR spectrometer contained a temperature control unit that used compressed air to circulate air at a certain temperature around the sample and brought it to this temperature after a certain waiting time. Here, the center of the signal was determined accordingly and plotted in Fig. 67b , too.

In addition, the influence of temperature on the $T_1$ time was determined on the NMR spectrometer in order to be able to estimate possible influences on the signal. The standard Inversion Recovering measurement was used to determine the $T_1$ time. The results are shown in Fig. 68.

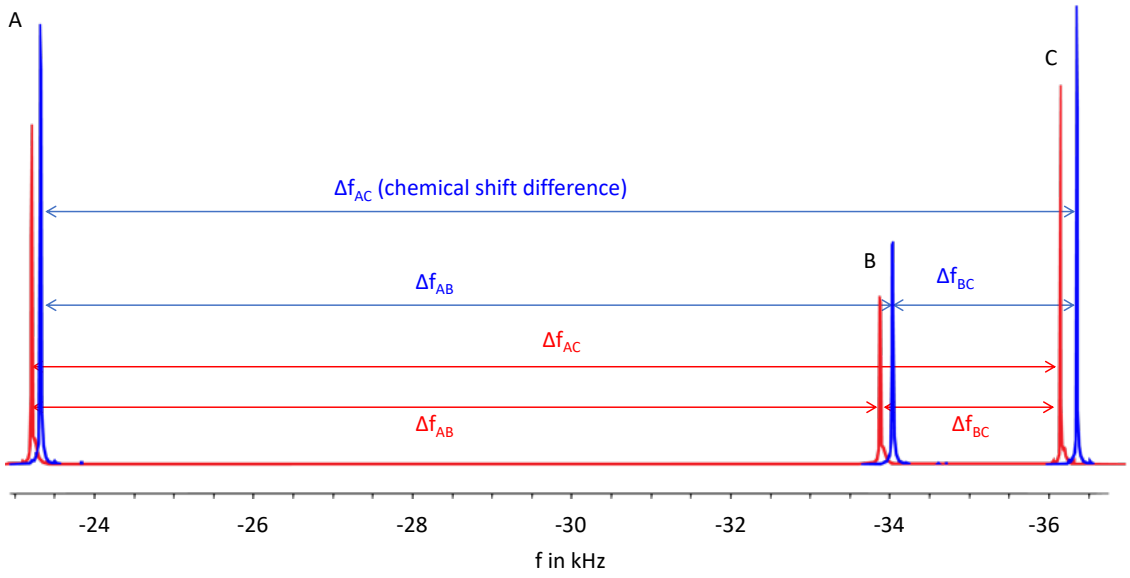


**Figure 69:** Chemical shift change for two different temperatures of 1.9 M HBFA dissolved in $D_2O$. The red spectrum shows a temperature of 330 K, while the blue spectrum was recorded at a temperature of 296 K. It can be observed that the differences $\Delta f_{XY}$ (where X and Y are A, B or C) to the same groups have individual characteristic values at each temperature. The designation of the groups A, B, and C refers to Fig. 52b.

In order to then investigate the effect of the temperature dependence of the chemical shift between signals of different fluorinated groups of a substance in more detail, heptafluorobutyric acid was used as an example substance (see Fig. 52b), which shows a signal from each of its three fluorinated groups in the spectrum. It was found that each of these signals had its own characteristic and temperature-dependent change in chemical shift., as can be seen in Fig. 69. This observation was used to generate calibration curves from the differences of the various signals that were specific to the respective temperature.

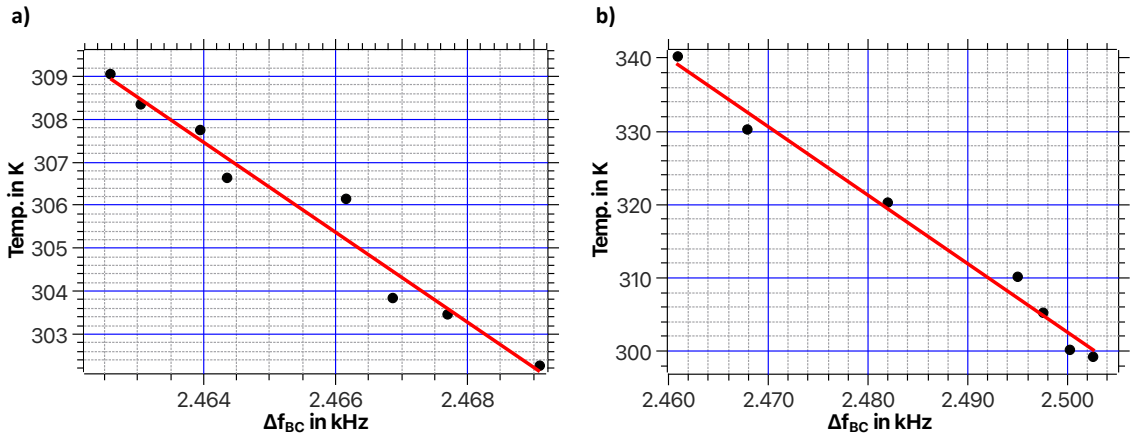


**Figure 70:** Frequency difference $\Delta f_{BC}$ in the spectra of 536 M heptafluorobutyric acid in aqueous solution between the signals of the $CF_2$ groups. a) Recorded with a 7 T MRI scanner with a self-developed RF coil. The solvent here was entirely $H_2O_{dist.}$. b) Recorded by a Bruker NMR spectrometer. Here 20 $\mu$L $D_2O$ and 580 $\mu$L $H_2O_{dist.}$ were used as solvent. The red line depicts a linear fit using SciDAVis.

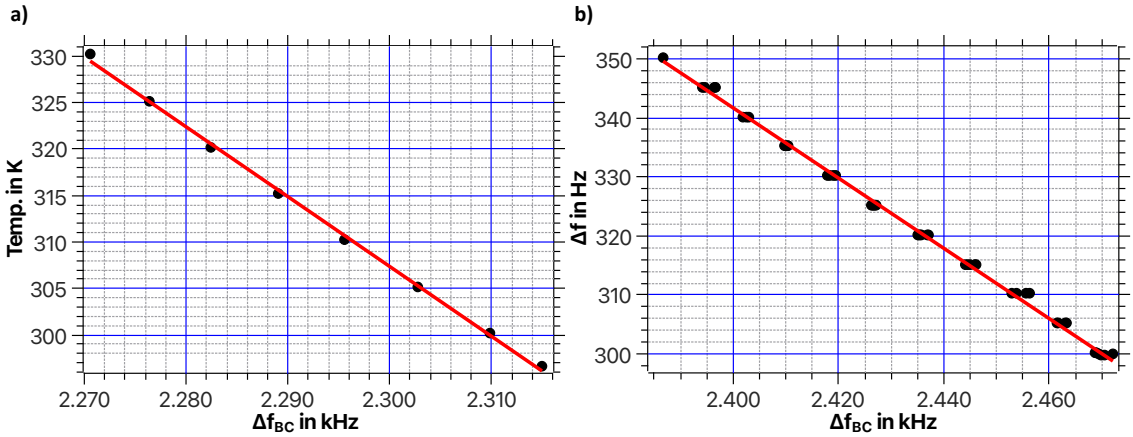


**Figure 71:** Frequency difference $\Delta f_{BC}$ in spectra of heptafluorobutyric acid in aqueous solution between the signals of the $CF_2$-groups recorded by a Bruker NMR spectrometer. a) At a concentration of 1.9 M. b) At a concentration of 0.96 M with multiple measurements per temperature step. The red line depicts a linear fit using SciDAVis.

For the 7 T MRI measurement, a $^{19}$F CSI sequence with a maximum bandwidth of 10 kHz was used. However, since the bandwidth between the outer signals of the HFBA is 13 kHz depending on the room temperature, it was decided to consider only the distance between the $CF_2$ groups at the measurments of the MRI scanner. The methods used to determine the temperature are similar to those used in the TFE measurements.

In Fig. 70a the temperature dependence of the differences of the chemical shifts of the $CF_2$ groups is plotted. From these distances, a calibration function could be determined in a first approximation as a linear fit with a coefficient of determination of $R^2 = 0.999$ for the 7 T MRI:

$$T = -1.04 \frac{\mathrm{K}}{\mathrm{Hz}} \cdot \Delta f_{\mathrm{BC}} + 2887\,\mathrm{K}. \tag{55}$$

This linear regression was performed using the SciDAVis software (`https://github.com/SciDAVis/scidavis`). It should be noted that the calculated error for the slope is $\pm 0.08 \frac{\mathrm{K}}{\mathrm{Hz}}$.

The results of the NMR measurements are shown in the Figs. 70b,71 and 72. As a first approximation, linear adjustments were made for the distance, all of which had a coefficient of determination $R^2 = 0.999$. First, the same concentration was measured as in the MRI experiment. For the lock signal, however, it was necessary to add some $D_2O$. Thus, 54.2 $\mu$L HFBA was dissolved in 580 $\mu$L $H_2O_{dist.}$ and 20 $\mu$L. This resulted in the following fit:

$$T = -0.94 \frac{\mathrm{K}}{\mathrm{Hz}} \cdot \Delta f_{\mathrm{BC}} + 2646\,\mathrm{K}, \tag{56}$$

with an error of the slope of $\pm 0.05 \frac{\mathrm{K}}{\mathrm{Hz}}$.

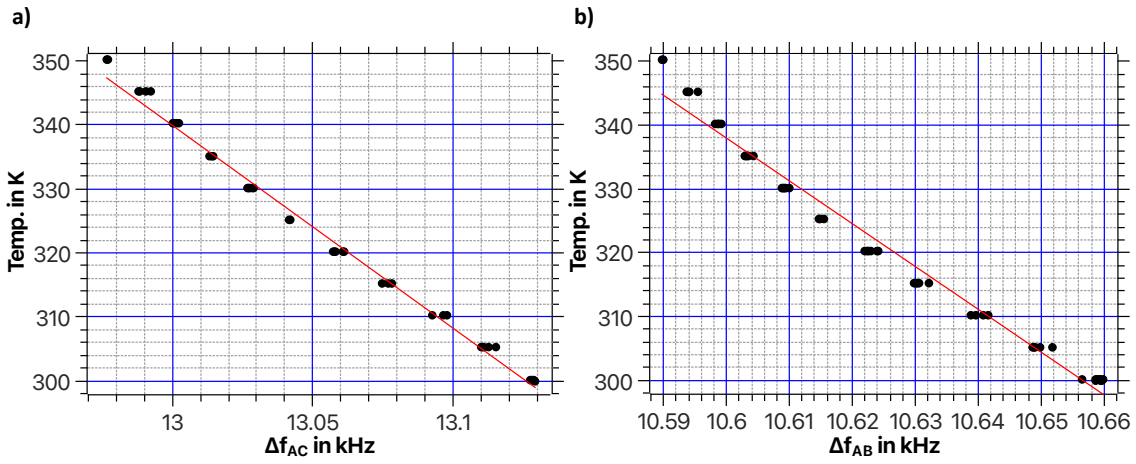


**Figure 72:** Distance in $^{19}$F NMR spectra of heptafluorobutyric acid in aqueous solution between the signals of the $CF_2$ and $CF_3$ groups: a) between group A and C b) between group A and B.

Next, for two different concentrations (shown in Fig. 71), the $CF_2$ groups were considered. For a concentration of 1.9 M (Fig. 71a), at which 0.5 mL HFBA was dissolved in 1.5 mL $H_2O_{dist}$ and 20 $\mu$L $D_2O$, the following fitting line was obtained:

$$T = -0.75 \frac{\mathrm{K}}{\mathrm{Hz}} \cdot \Delta f_{\mathrm{BC}} + 2036\,\mathrm{K}, \tag{57}$$

with an error of the slope of $\pm 0.01 \frac{\mathrm{K}}{\mathrm{Hz}}$. For a concentration of 0.96 M (Fig. 71b) this finally resulted in

$$T = -0.59 \frac{\mathrm{K}}{\mathrm{Hz}} \cdot \Delta f_{\mathrm{BC}} + 1763\,\mathrm{K}. \tag{58}$$

In order to also obtain an estimate of the other differences, the difference in chemical shifts between the $CF_3$ group and the $CF_2$ groups was also measured at 0.96 M. The difference between groups A and C from Fig. 52b are shown in Fig. 72a and can be represented by the following fit:

$$T = -316.06 \frac{\mathrm{K}}{\mathrm{Hz}} \cdot \Delta f_{\mathrm{AC}} + 4448\,\mathrm{K}, \tag{59}$$

with an error of the slope of $\pm 3,23 \frac{\mathrm{K}}{\mathrm{Hz}}$. For the difference between groups A and B, the fit in Fig. 72b then with

$$T = -670.79 \frac{\mathrm{K}}{\mathrm{Hz}} \cdot \Delta f_{\mathrm{AB}} + 7448\,\mathrm{K}, \tag{60}$$

and an error of the slope of $\pm 12.63 \frac{\mathrm{K}}{\mathrm{Hz}}$.

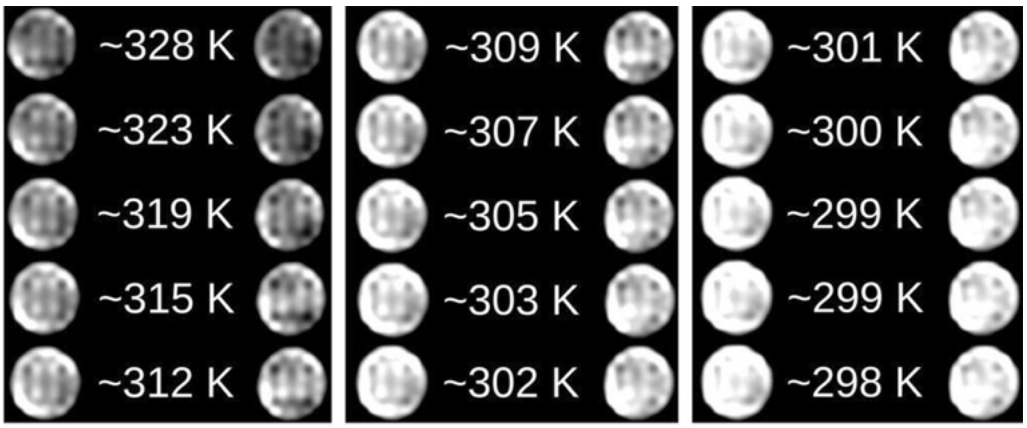


**Figure 73:** Temperature dependent imaging of HFBA dissolved in $H_2O_{dist.}$. The imaging was recorded at different states of cooling of a previously heated cylindrical phantom (Fig. 48). The images to the right and left of the temperature are the generated images of the $CF_2$ groups of the HFBA (see Fig. 59). Between 328 K and 298 K an $SNR$ increase of about 25% can be seen. The FLASH sequence had following parameters: imaging size: 64 x 64; slice thickness: 2 mm; TE: 9.8 ms; TR: 500 ms; FoV: 100 x 100 $mm^2$.

After the temperature determination by means of MR spectroscopy was investigated, a possible temperature determination by means of imaging was also investigated. A cylindrical phantom (Fig. 48) filled with HFBA dissolved in $H_2O_{dist.}$ was used in order to be able to heat it up and to allow it to cool down as homogeneously as possible afterwards. This was again kept at a constant temperature in a beaker of water for one hour and then quickly placed in the MRI scanner. During the subsequent cooling process, FLASH imaging was performed continuously in order to examine the contrast shift. A shift of the images along the frequency encoding direction could not be detected.

# 6 Discussion

## 6.1 Overview

The aim of this work was to develop, construct and test an imaging system for a 7 T MRI that is capable of both $^{19}$F and $^{1}$H imaging. It was important that a sufficient signal could be recorded for imaging at both Larmor frequencies as well as that it was possible to switch easily between the nuclei. At the same time, imaging both nuclei poses a challenge in that the resonance frequencies are very close together. This makes it very difficult to decouple the two signals and brings with it further problems that can only be solved with complex circuits.[65] Therefore, in this work, a simpler design as a proof-of-principle study was chosen to build an MRI coil that is directly matched to $^{19}$F, but the resonance curve is wide enough that there is still enough signal available for $^{1}$H imaging. Similar concepts have already been used in other systems that work with lower field strengths in our working group for imaging and spectroscopy in particular.[66] In the back of my minds, we always had a possible application as a $^{19}$F contrast agent, which simultaneously enables $^{1}$H MR anatomy or angiography imaging.

A transmit-receive system was developed for this purpose, which was able to control a phased-array coil and simultaneously transmit the measured signal pre-amplified to the 7 T MRI. The MRI coils developed for this purpose were a surface coil as a simple concept confirmation and then a four-element volume coil in a phased-array design. These were first simulated and adapted for the design using 3D field simulations and then built and measured. The discussion about the comparison of the simulation results and the final exact measurement of the constructed coils in the 7 T MRI is described in chapter 6.2. In the following section 6.3, the results of the $^{19}$F and $^{1}$H imaging are discussed and compared and classified with other studies. In the last section 6.4, observations made in this work regarding the temperature sensitivity of various fluorine compounds are discussed. In this chapter, various methods that enable spatially resolved temperature imaging are evaluated and compared with previous methods. In addition, the limitations and the need for development in this area are also presented.

## 6.2 Comparison of Simulation and Experiments

In order to have a basic concept for the later volume coil, a surface coil was built, which initially does not affect the following points as a problem:

- Decoupling of several elements from each other to enable the highest possible transmit efficiency and possible parallel imaging.
- Distribution of the input signal to the various elements.
- Inhomogeneities of individual components and elements in reality, which lead to the measured signal also becoming inhomogeneous, without the direct coil construction being included here.

If you now look at the simulated results in Fig. 15, it can be seen very clearly that the fit is already very much based on the Larmor frequency of $^{19}$F. Nevertheless, little loss in the $^{1}$H signal can be seen in the $B_1^+$ field distributions. This is partly due to the load built into the coil, but also to the fact that the energy drops off close to the coil elements, which is the purpose of a surface coil, and the signals no longer drop off so quickly at some distance. As a result, the surface coil also produces a relatively homogeneous signal within the phantom. The comparison of the Figs. 16 and 17 clearly shows once again that the orientation in the MRI is significantly decisive for the $B_1^+$ field distribution. However, since only a surface coil lying on the patient couch was used in the experiments and elements that ran parallel to the field lines were also used in the volume coil, the distribution in 16 is the more relevant one. It is particularly interesting here that although the peaks of the field distribution are significantly higher in the range of the $^{19}$F frequency, as it is also significantly more adapted in this range, similar values for the fields prevail within the phantom. Due to the circular polarization of the $B_1^+$ field, a slight asymmetry of the signal can also be seen, which describes an attenuation on the right side of the phantom. This effect can also be clearly seen in Fig. 53, where the attenuated area predominates in the upper area due to a change in orientation.

A change in the position of the phantom, i.e. the rotation of the cylinder into a horizontal position, causes a slight change in the reflection parameters in the simulation, as can be seen in Fig. 18, but does not result in a major qualitative change in the efficiency of the MRI coil. Especially against the background of the field distribution within the phantom observed and described above with different matching, it can be concluded from this, that the position of the phantom should have little influence on the image quality as long as the actual imaging takes place within the center of the coil. The comparison of the S-parameters for the built coil also shows very good agreement with the simulation. However, it is noticeable here that the matching capacitance had to be adjusted more strongly from the simulation to the construction (in this case by a factor of eight). This indicates that the network required a better adaptation to the connecting cables than in the idealized simulation, in which connected cables played no role. However, all other values of the capacities could be approximately adopted and thus indicate a good match between the simulated results and the built reality.

All these results and possible comparisons with reality show a high level of agreement between simulation and experiment. From this it was concluded for this work that the field distributions for the $^{19}$F frequency also agree accordingly, which unfortunately could not be reproduced within the experiment, since the source code of the sequences was not available for this and also no sequence that allowed the $^{19}$F imaging to perform a $B_1^+$-mapping.

After these results showed that imaging within the 7 T scanner works in principle and at the same time the results could be predicted by the simulations, the aim was to build the volume coil. The simulations of the S-parameters initially showed that the shape and volume of the phantom played a very important role in the matching and tuning of the coil. Besides the filling-factor of the coil the q-factor is one of the most important aspects to explain this phenomenon.

These influences are so significant that, as shown in Fig. 35, the fit of $^{19}$F and $^{1}$H are very close to each other, whereas clear differences could be seen in advance (Fig. 23). This shows, especially in connection with the $B_1^+$ field distributions, that imaging is also possible with different loads, but the efficiency of the coil depends significantly on which shape and which mass is used as the load. Although this shows good comparability for the experiments presented, it should be addressed again as a topic for a broader use of the coil, as this may lead to subsequent problems and difficulties in comparability. For this coil, this problem was solved by making each load adjustable with tunable capacitances at the opposite site of the ports at the coil.

In addition, it had already been observed with the surface coil that the ultimate influence on the field distribution did not depend exclusively on the adjustment of the reflection parameters. This effect was observed all the more with the four-element coil for the 7 T MRI. Here it went so far that, as shown in Fig. 28, depending on the load distribution and shape, even the field intensity for the $B_1^+$ field distribution was stronger for 297.2 MHz, the Larmor frequency of $^{1}$H, than for 279.5 MHz, the Larmor frequency of $^{19}$F. This could be justified after some investigation of the simulation results over various points. On the one hand, as also shown in Fig. 29, the better matching was not only reflected in a higher $B_1^+$ field distribution, but also in higher losses due to the conditional E-fields, which could not be used for imaging. At the same time, one can see in Fig. 27 that, on the one hand, the fitting of the reflection parameters has shifted and thus deteriorated for the specific Larmor frequency of $^{19}$F. On the other hand, the coupling to the direct and nearest neighbors in the Larmor frequency range of $^{1}$H is significantly weaker than in the range of $^{19}$F, so that the field can establish itself better for $^{1}$H, even if the overall fit is worse. At this point, more attention should be paid to the decoupling of the elements in future work. However, as can be seen from the Figs. 30, 31 and 33, re-tuning via the tunable capacitances produces the expected stronger field distribution for $^{19}$F than for $^{1}$H.

If one now compares the results of the simulations with those obtained during the measurements of the built four-element coil, it first becomes apparent that the required capacitance values of the coil in the simulation were very close to those in reality and could thus considerably simplify the entire design and many conclusions from the simulation were also a good indication of the built coil. However, one value that differed significantly by a factor of almost two was the value of the capacitance for decoupling, where an idealized assumption was also made in the simulation and no additional ports or lumped elements were inserted (see Fig. 22).

However, if you now look at the progression of the S-parameters across the frequency spectrum between the simulation (Fig. 30) and the measured results (Fig. 45), you will initially notice that the qualitative progression looks very similar. However, the measured spectrum appears to be somewhat "compressed" on the frequency axis compared to the simulated spectrum. As a result, the couplings are significantly lower, especially in the Larmor frequency range of $^{1}$H. Since the optimization of the matching was multivariant and the capacitances were not available for every value and also always show slight fluctuations, a simulation was then carried out again with the real capacitance values used. This showed

that the fit to the frequencies in particular remained very constant, but that the couplings between the elements certainly differed (Fig. 46). One explanation for this could again be the idealized simulation method, although it was decided that these values were sufficient for this proof of principle study to demonstrate the feasibility and challenges of $^{19}$F imaging in 7 T MRI.

Looking at the results of the $B_1^+$-field distribution between simulation (e.g. Fig. 39) and measurement (Fig. 53) for $^{1}$H, a slight inhomogeneity compared to the simulation is initially noticeable in the experiment. The following explanations can be found for this. Though, there were repeated problems with the control during the construction of the MRI coil, some of which could be explained by loose contacts, which resulted from various adjustments. This once again clearly shows that for a fixed system in the future, the variable adjustments to the measurement objects should be kept to a minimum in order to ensure good reproducibility. In addition, not all channels were exactly comparable in terms of their performance. In order to counteract this effect in the simulation, it was decided to carry out another simulation in which only one element is actively controlled and all other elements are terminated accordingly with 50 Ω, which is certainly a variant of inhomogeneous excitation, but makes the behaviour more visible. The result of this is shown in Fig. 41. It is noticeable that the influence of inhomogeneous excitation is significant, especially in $^{19}$F imaging. Here, signal extinction occurs in the center of the coil. But even for $^{1}$H imaging, the effect is not negligible, especially if the phantom is not positioned 100% in the center (which was mostly the case due to the positioning on different pads). In this respect, the result of the measurement can be considered to be quite expected against the background of the conditions. Since, as already mentioned above, it was not possible to measure the $B_1^+$ field distribution for $^{19}$F, it is assumed that the simulations are in good agreement here as well, and that the extinctions within the phantom in particular can also be reproduced very well in the imaging (Fig. 41).

## 6.3 $^{19}$F and $^{1}$H MR Imaging

Once the basic design of the coil had been completed and the usability of the simulation had been evaluated, various imaging experiments were carried out. Additionally in the experimental session it was shown that the two main sequences used for clinical imaging (fast spin and fast gradient recalled echo) led to good results. The comparatively long TR times here were due to the long T1 times of many fluorinated substances.[11] For this evaluation, TFE was first measured at different concentrations. It was found that both $^{19}$F imaging (Fig. 57) and $^{1}$H imaging (Fig. 56) led to good results, which also allowed sub-mm resolution.

The measured concentration series with TFE in aqueous solution showed a good sensitivity of the coil. Thus, measurements with a sub-mm resolution down to below 7 mM concentration could be performed (Fig. 61). At lower concentrations, the resolution had to be reduced. Minimal concentrations of 700 $\mu$M TFE dissolved in $H_2O_{dist.}$ could be detected. Here, the structure of the phantom could still be clearly traced due to a signal-to-noise ratio of 2.5. Caused by the voxel size of 1.5 x 1.5 x 20 mm$^3$, the corresponding concentra-

tion and the fact that three fluorine nuclei contribute to the signal in trifluoroethanol, it can be estimated that $5.7 \cdot 10^{16}$ fluorine nuclei per voxel could be detected, which corresponds to approximately $9.45 \cdot 10^{-8}$ mol. The results for the lowest concentration could be recorded with 32 averages and a recording time of 4 min using a turbo spin-echo sequence.

A comparison to existing results of other groups is difficult due to the lack of similar developments. However, the group of van Gorp et al. [26] has also developed an eight-channel coil system on a 7 T human scanner. The results shown in this work were achieved with a complex $B_1$ shimming and over 2000 averages. Nevertheless, Gorp et al. achieved lower sensitivity and lower homogeneity compared to the statically structured four-element coil shown in my work. Fluorine was detected there only by MRS and the lowest detectable concentration was 5 mM of capecitabine. A major advantage of the coil developed by van Gorp et al. over my coil is that it has already been tested on test subjects and was designed to be as flexible as possible thanks to its plate-like design. Van Gorp's group also focused on broadband tuning and matching of the coil.

In order to obtain measurement data of more inhomogenous substance distributions, an experimental multi-chamber phantom was constructed and created using 3D printing (Fig. 51). In the imaging experiments using this phantom, it was possible, as shown in Fig. 60, to detect a fluorine signal in both chambers, although TFE was only added to one of the two chambers. Subsequent investigations with a 300 MHz Bruker NMR spectrometer, with which samples from both chambers were examined, showed an $^{19}$F signal for both samples. From this it can be concluded that the TFE had diffused through the plastic into both chambers, so that a simple assignment was no longer possible.Due to the complexity of this problem and because it was not the main focus here, this project may be further evaluated in future experiments.

When imaging HFBA, two objects could be seen seperated along the read out axis (Fig. 59), although there was only one tube in the coil. Robien showed in [67] that HFBA displays three well seperable NMR $^{19}$F signals within the range of about 50 ppm. The signals of the two $CF_2$ groups are 7 ppm apart, which corresponds to about 2080.4 Hz for 7 T at the human scanner. The distance to the $CF_3$ group, on the other hand, is significantly greater at 39.2 ppm and 46.2 ppm respectively. The signals are approximately 27 px apart, whereby the bandwidth per pixel on the encoded axis frequency corresponds to 80 Hz/px. This would result in a distance between the signals of 2160 Hz. Taking into account that Robien's measurements were reported in $CDCl_3$ and our measurements in $H_2O_{dist.}$, it was concluded that the typical chemical shift artifact was generated by the signals of the two $CF_2$ groups and is close to the literature values. This means that when measuring fluorinated substances with several signals, care should always be taken to select the bandwidth of the frequency encoded direction carefully so that no artifacts are produced.

In this work, fluorinated test substances were used, which should serve as proof of principle. Further work needs to be done to develop possible contrast agents that have sufficient concentration for imaging, are cell-permeable and at the same time do not have a toxic effect on the human body. Future derivatization or encapsulation are also possibilities that

should be considered. However, motivated by the experiments with the low concentrations that could be detected by imaging, this work also looked for a freely available substance that also enters the human body in everyday life. Walnuts, with a relatively high proportion of fluorinated compounds [68], are the first option here, but the walnut would have to be pressed, and it is also uncertain whether the liquid would take the fluorine with it and in what form it would then be present. As a substance of daily use we examined fluorinated toothpaste. According to the manufacturer, 100 g of the product elmex® gelée contains 0.287 g dectaflur, 3.032 g olaflur and 2.21 g sodium fluoride or 1.25 % total fluoride content. These concentrations are close to the detection limit, however, Fig. 63 shows that imaging of these substances is possible. Though, shimming was difficult because the air bubbles were challenging to be removed completly from the gel and could not be removed completely. The exact composition of the product is also not known, which is why different compounds with very different chemical shifts probably contribute a signal and therefore it cannot be estimated which amount of fluorine atoms ultimately contribute to the imaging. Nevertheless, this result shows that products are already in use that can be safely introduced into the human body and that further development of fluorine-containing contrast agents is therefore conceivable. In addition, many other fluorine-containing drugs are already used to treat various diseases, some of which could potentially serve as fluorine-containing contrast agents.

## 6.4 Temperature Measurement

As an application of the developed coil this work showed the non invasive measurement of temperature is possible. This included spectroscopic and imaging measurements. The first temperature-sensitivity experiments of $^{19}$F MR signals were carried out in 1965 by Newmark and Sederholm. In these they investigated internal rotation in halogen-substituted ethanes. [69] Three years later, R. A. Newmark and R. E. Graves investigated the halogenated molecules $CFCl_3$ and $CF_2Cl_2$. [70] The first larger organic molecules (perfluorodecalin and perfluorotributylamine) were finally investigated by Berkowitz et al. 1992 with regard to $^{19}$F MR temperature sensitivity. [71] In recent decades, studies have been carried out with liposomes or perfluorocyclohexyl ethers, for example. In these, the temperature change led to a release of the fluorinated molecules and a change in the chemical shift. [20], [21], [72] Motivated on these findings, spectroscopic experiments on a 7 T Bruker NMR spectrometer were carried out for comparison, and additionally on a 7 T MRI which allowed to compare both results.

Corresponding temperature measurements were mainly performed with HFBA and TFE. This choice of investigations was interesting insofar as experiments that had previously been carried out only on the Bruker NMR spectrometer [73] showed that substances with a fluorinated group (in this case TFE) were easier to observe overall and that TFE also produced a clear triplet splitting, which was also clearly visible in the 7 T MRS (Fig. 66). Heptafluorobutyric acid, on the other hand, has several fluorinated groups, which makes it challenging for imaging, as discussed above, but showed interesting properties as spectroscopy-based a temperature marker.

In order to obtain an estimate of how well spectroscopic measurements can be carried out at the 7 T MRI, spectra of TFE dissolved in water were first recorded and compared with those in the spectrometer. These showed very good agreement (Fig. 66). In order to determine this agreement quantitatively, the $^3J_{HF}$-coupling in the triplet splitting of the signal was determined. To minimize measurement errors due to the reading, the distance in frequencies between the two outer peaks was measured and devided by two, as the system is symmetrical around the middle peak, as expected. Both the 7 T MRI and the Bruker NMR spectrometer showed a $^3J_{HF}$-coupling of about 8.7 Hz. This is in very good agreement with the values in the literature presenting a coupling constant of $^3\mathrm{J}_{FH}$ of 8.8 Hz.[74]

First, as expected, the temperature change was found to have an effect on the frequency and amplitudes of the $^{19}$F MR signals. When the sample is heated, only a slight decrease and broadening of the signal amplitude is observed. This could be due to various effects caused by the relaxation times, Boltzmann distribution and hydrophobically induced aggregation.[75]–[77] For a first comparison, the chemical shift of each $^{19}$F signal was plotted against temperature (Fig. 67). Although the data points are not linear over a wider temperature range, a linear regression can be used as a good approximation for the initial assessment in the temperature range of interest for potential future applications, as shown by the high coefficient of determination.

However, temperature is not the only factor influencing the chemical shift, but also the concentration, solvent, pH, gases and/or ions in the solution. The presented work clearly demonstrates the relationship between the chemical structure of fluorinated molecules and the temperature sensitivity of $^{19}$F MR signals in aqueous solution. These measurements are built on the previously mentioned publications by Berkowitz et al. [71] and Lee et al. [78] but emphasize the application in water. It was shown that temperature coefficients $\mathrm{C}_T$ of 5,6 Hz/K (corresponding to 0.02 ppm/K) could be achieved. $\mathrm{C}_T$ could even be driven up to 8.8 Hz/K with other substances on the spectrometer in the work by Bruns et al. (which also contains some of this presented work). In comparison to Bruns et al. where mainly $\mathrm{D_2O}$ was used, however, here only $\mathrm{H_2O}$ was used. In previous work by Prinz et al. [79] which also dealt with temperature markers, maximum values of 0.0082 ppm/K (corresponding to 2.3Hz/K at 7 T) were given.

The next step was to use the HFBA to measure a substance that shows multiple non-overlapping fluorine signals. Because each group of the substance has characteristic chemical shifts as a function of temperature that are independent of each other, the temperature can be calculated from the difference in chemical shifts of the individual signals without measuring a reference sample in the system. Here it is important to ensure that all fluorine signals originate from one compound and that intermolecular interactions between different fluorinated substances can be excluded. All of this applies to HFBA dissolved in water, and three signals are clearly recognizable due to two chemically non-equivalent $\mathrm{CF_2}$ groups and one $\mathrm{CF_3}$ group. However, the distances between the signals differ considerably due to the different temperature sensitivities. As the frequency difference between the $\mathrm{CF_2}$ and the $\mathrm{CF_3}$ group was above the maximum possible bandwidth of 10kHz of the available spectroscopic sequences on the 7 T MRI, which led to infolding of the $\mathrm{CF_3}$ group in the

frequency window. The comparative measurements with the NMR allowed the signals of the two $CF_2$ groups to be differentiated by their distance in frequency (2520 Hz in the 7 T MRI and 2580 Hz in the Bruker NMR spectrometer), so that this difference was sufficient for the temperature determination. Subsequently, calibration functions were determined using linear fits.

Nevertheless, it became apparent that the determination of the calibration curves still required further investigation. Here it was shown that the approach of the differences of the chemical shifts was a promising approach, which could also be seen in the MRI. However, the error in the rise also showed that its influence on the temperature determination is too great now to be used for specific biological applications. One of the reasons for this was the difficulty in determining the reference temperature using the fiber optic cables, which were on the one hand sensitive to the magnetic field and could on the other hand only accurately determine one point within the phantom at a time.

To investigate the potential for spatial resolution, a CSI sequence was additionally employed. The idea here is that spatially resolved spectra can be measured (Fig. 64). This allows the temperature to be determined at different locations with the resolution of the voxels of the CSI sequences using the method above. However, since only homogeneous phantoms were used in these experiments, which were cooled down relatively slowly, only uniform temperature changes could be determined here. An additional problem arose in the registration of the voxels. Since the mapping was performed on a localizer image with $^1H$ imaging, there were slight shifts between the phantom and the measured values of the CSI due to the different registered frequencies. For this proof-of-principle study, it was sufficient to demonstrate the procedure. For a concrete application, however, this registration problem in the design of the sequences still needs to be adjusted.

Finally, the extent to which direct imaging can be used for temperature determination was investigated. A sample was heated and an image was taken at time intervals during the cooling process (Fig. 73). This resulted in a lower $SNR$ for higher temperatures compared to lower temperatures. Specifically, the temperature difference between 328 K and 298 K resulted in an $SNR$ drop of approximately 25 %. However, this method has some difficulties. Firstly, the temperature of this temperature series was determined by estimation rather than measurement and only the start and end values were determined precisely. The much greater problem, however, is the multiple temperature dependence of the signal.[75]–[77] It may be possible to calibrate the sequences in such a way that they can reproducibly determine the temperature in a known phantom. However, in order to then measure in phantoms or even biological systems that have not been used or calibrated beforehand, the significance is not reliable enough. This approach was therefore not pursued further.

Another attempt would be to use the described effect of the chemical shift artefact appearing as "double image" due to the different larmor frequencies of the two $CF_2$ groups by matching the bandwidth so that the images shift in relation to each other depending on the temperature. Nevertheless, even this effect does not allow a good spatial resolution of the temperature, as the image would be distorted accordingly at different temperatures.

In addition, a very small bandwidth per pixel would have to be used here, which in turn would have other negative effects.

In general, it can be said that the described methods represent an improvement of temperature determination using fluorinated substances, but ultimately their use for *in vivo* measurements still requires further investigation. In particular, the dependence of the chemical shift on the pH value and the concentration poses a challenge for complex systems.

# 7 Conclusion and Prospects

This work shows as a proof-of-principle study the simulation, construction and evaluation of a $^{19}F/^{1}H$ phased-array coil for a Siemens 7 T MRI. Despite the high field strength, a system was chosen that was resonantly matched and tuned to the Larmor frequency of $^{19}F$, exhibiting sufficient broadband characteristics that $^{1}H$ frequency could be detected with a good $SNR$. The simulation results in particular showed that the difference in transmit efficiency for both hydrogen and fluorine was not as high as would initially have been expected for a single-matched coil, mainly due to the coupling of the different elements. In future research, a way should be found to decouple the elements more strongly, which would lead to a better $SNR$, especially for $^{19}F$ imaging. The experiments also showed that the $SNR$ with respect to $^{1}H$ should allow easy identification of the position of the $^{19}F$ signal using the $^{1}H$ MRI. In addition, this coil showed that high $SNR$ in imaging is possible in a 7 T human scanner, but its current diameter has to be adapted to allow human imaging. For this purpose, a larger diameter must be designed in further work. First results were shown here by according simulation.

In addition to imaging, spectroscopic investigations were also carried out. In a comparison with the results of the same substances at the same field strength at a 7 T Bruker NMR spectrometer, showed that the results agreed well. In addition, the temperature dependence of the spectrum was observed using TFE as an example. As expected, a change in the chemical shift of the signal was observed and at the same time a reduction in amplitude with simultaneous broadening of the signal. With another substance, HFBA, it could be shown that different fluorinated groups of a substance exhibit different chemical shift changes depending on the temperature. Due to the good distinguishability of the signals through their large frequency difference, a method was developed which uses these differences between the chemical shifts of the various groups in order to be able to use them for a temperature measurement without an additional reference substance. This method was also applied using spatially resolving CSI sequences in order to prove that a spatial resolution of the temperature is also possible. However, the experiments showed that this method is still very dependent on external parameters such as the concentration of the fluorinated substance, the pH value, gas and ions in solution, and the solvent. Here too, further measurements will be necessary to calibrate and apply this method in biological systems.

Ultimately, most of the experiments in this work were carried out with TFE and HFBA. Both substances are not biocompatible in their pure form. Here too, further work is needed to find substances that are both biocompatible and cell-permeable and at the same time have enough fluorine atoms to obtain sufficient signal for imaging and thus ultimately to be able to use fluorinated substances as contrast agents. Both the fluorinated drugs already in use and encapsulation of fluorinated substances are promising options. It would also be advantageous if the substances had different fluorinated groups with a large frequency difference in the chemical shift so that they could also be used as temperature markers. Some promising work has already been published here in recent years.[73], [80]

Overall, this work has shown that both imaging and spectroscopy of fluorine on the 7 T human scanner is possible at low concentrations of sub-mM range, which also makes the use of fluorinated contrast agents conceivable. In addition, it was shown that under certain circumstances it would also be possible to resolve the spatial of temperature using according fluorinated substances.

# 9 List of Abbreviations and Formulas

**Abbreviations**

| | |
|---|---|
| $SNR$ | Signal-to-Noise Ratio |
| *in vivo* | Investigation performed on a living organism |
| CAD | Computer Aided Design |
| CP | Circular polarization |
| CSI | Chemical Shift Imaging |
| EM | Electromagnetic |
| FDTD | Finite-Difference Time Domain |
| FID | Free Induction Decay |
| FIT | Finite Integration Technique |
| FLASH | Fast Low Angle Shot |
| FoV | Field of View |
| FR4 | Glass-reinforced epoxy laminate material |
| GRE | Gradient Recalles Echo |
| GUI | Graphical user interface |
| HF | High Frequency |
| HFBA | Heptafluorobutyric acid ($CF_3CF_2CF_2COOH$) |
| MGE | Maxwell Grid Equations |
| MR | Magnetic Resonance |
| MRI | Magnetic Resonance Imaging |
| NA | Number of Acquisitions |
| NMR | Nuclear Magnetic Resonance |
| pin-Diode | Positive intrinsic negative diode |
| PLA | Polylactic acid |
| px | Pixel |
| RF | Radio Frequency |
| ROI | Region of Interest |
| Rx | Receive |
| S-parameter | Scatter parameter |
| SAR | Specific Absorption Rate |
| SMA | SubMiniature version A |
| SWR | Standing Wave Ratio |
| TE | Echo Time |
| TFE | 2,2,2-Trifluoroethanol ($C_2H_3F_3O$) |
| TR | Repetition Time |
| TSE | Turbo Spin Echo |
| Tx | Transmit |
| Tx/Rx | Transmit/Receive |

| | |
|---|---|
| UTE | Ultrashort Echo Time |
| Voxel | Volumetric pixel |

**Formula Symbols**

| | |
|---|---|
| $\alpha$ | Flip angle |
| $\epsilon$ | Permittivity |
| $\epsilon_0$ | Electric field constant in vacuum |
| $\epsilon_r$ | Relative permittivity |
| $\gamma$ | Gyromagnetic ratio |
| $\gamma_p$ | Propagation constant |
| $\hbar$ | Planck's quantum of action |
| $\lambda$ | Wavelength |
| $\mu$ | Permeability |
| $\mu_0$ | Magnetic field constant in vacuum |
| $\mu_r$ | Relative permeability |
| $\nabla$ | Nabla operator |
| $\omega_L$ | Larmor circuit frequency |
| $\rho$ | Charge density |
| $\rho$ | Charge distribution |
| $\sigma$ | Electrical material conductivity |
| $\vec{E}$ | Electric field strength |
| $\vec{k}$ | Wave vector |
| $\vec{S}$ | Nuclear spin |
| $\vec{\mu}_M$ | magnetic dipole moment |
| $\overrightarrow{B_0}$ | Static magnetic field |
| $\overrightarrow{B_1}$ | Excitation magnetic field |
| $\vec{j}$ | Electric current density |
| $\overrightarrow{M}$ | Longitudinal magnetization in z-direction |
| $\vec{S}_P$ | Poynting-Vektor |
| $B_1^+$ | Rotating $B_1$-field in nuclear spin direction |
| $B_1^-$ | $B_1$ field rotating in the opposite direction to the nuclear spin |
| $C'$ | Capacitance layer |
| $CF$ | Receiving coil factor |
| $f$ | Frequency |
| $G$ | Conductance |
| $G'$ | Conductance layer |
| $k_B$ | Boltzmann constant |
| $L$ | Inductance |
| $L'$ | Inductance coating |
| $M_z$ | Longitudinal magnetization in z-direction |
| $M_{xy}$ | Transverse magnetization in x- and y-direction |
| $n_\alpha$ | Number of spins with lower energy level |
| $n_\beta$ | Number of spins with higher energy level |
| $n_{ap}$ | Number of antiparallel spins |
| $n_p$ | Number of parallel spins |

| | |
|---|---|
| $R'$ | Resistance load |
| $T$ | Temperature |
| $t$ | Time |
| $t_0$ | Start time of the pulse |
| $T_1$ | Longitudinal relaxation |
| $T_2$ | Transverse relaxation |
| $t_p$ | Pulse duration |
| $Z_0$ | Impedance of free space |
| $Z_C$ | Characteristic impedance |

# 10 Bibliography


[1] F. Bloch, W. W. Hansen, and M. Packard, "The nuclear induction experiment", *Physical Review*, vol. 70, no. 7, pp. 474–485, Oct. 1, 1946, Publisher: American Physical Society. DOI: 10.1103/PhysRev.70.474. [Online]. Available: https://link.aps.org/doi/10.1103/PhysRev.70.474 (visited on 06/04/2024).

[2] I. I. Rabi, "Space quantization in a gyrating magnetic field", *Physical Review*, vol. 51, no. 8, pp. 652–654, Apr. 15, 1937, Publisher: American Physical Society. DOI: 10.1103/PhysRev.51.652. [Online]. Available: https://link.aps.org/doi/10.1103/PhysRev.51.652 (visited on 06/17/2024).

[3] E. M. Purcell, H. C. Torrey, and R. V. Pound, "Resonance absorption by nuclear magnetic moments in a solid", *Physical Review*, vol. 69, no. 1, pp. 37–38, Jan. 1, 1946, Publisher: American Physical Society. DOI: 10.1103/PhysRev.69.37. [Online]. Available: https://link.aps.org/doi/10.1103/PhysRev.69.37 (visited on 06/17/2024).

[4] M. A. Brown and R. C. Semelka, *MRI: basic principles and applications*, 4th ed. Hoboken, N.J: Wiley-Blackwell/John Wiley & Sons, 2010, 264 pp., OCLC: ocn520441344, ISBN: 978-0-470-50098-9.

[5] R. Damadian, "Tumor detection by nuclear magnetic resonance", *Science (New York, N.Y.)*, vol. 171, no. 3976, pp. 1151–1153, Mar. 19, 1971, ISSN: 0036-8075. DOI: 10.1126/science.171.3976.1151.

[6] P. Mansfield and A. A. Maudsley, "Line scan proton spin imaging in biological structures by NMR", *Physics in Medicine and Biology*, vol. 21, no. 5, pp. 847–852, Sep. 1976, ISSN: 0031-9155. DOI: 10.1088/0031-9155/21/5/013.

[7] P. Mansfield and A. A. Maudsley, "Medical imaging by NMR", *The British Journal of Radiology*, vol. 50, no. 591, pp. 188–194, Mar. 1977, ISSN: 0007-1285. DOI: 10.1259/0007-1285-50-591-188.

[8] R. Lützkendorf, J. Bernarding, F. Viezens, A. Thiel, and D. Krefting, "Enabling of grid based diffusion tensor imaging using a workflow implementation of FSL", *Studies in health technology and informatics*, vol. 147, pp. 72–81, Feb. 2009. DOI: 10.3233/978-1-60750-027-8-72.

[9] S. Hirsch, J. Braun, and I. Sack, *Magnetic Resonance Elastography: Physical Background And Medical Applications*. Weinheim: Wiley-VCH Verlag, 2017, 426 pp., ISBN: 978-3-527-34008-8.

[10] E. T. Ahrens, R. Flores, H. Xu, and P. A. Morel, "In vivo imaging platform for tracking immunotherapeutic cells", *Nature Biotechnology*, vol. 23, no. 8, pp. 983–987, Aug. 2005, ISSN: 1087-0156. DOI: 10.1038/nbt1121.

[11] U. Flogel and E. Ahrens, *Fluorine Magnetic Resonance Imaging*, 1st ed. Singapore: Pan Stanford Publishing Pte Ltd, Oct. 21, 2016, 445 pp., ISBN: 978-981-4745-31-4.

[12] J. Ruiz-Cabello, B. P. Barnett, P. A. Bottomley, and J. W. M. Bulte, "Fluorine ($^{19}$F) MRS and MRI in biomedicine", *NMR in biomedicine*, vol. 24, no. 2, pp. 114–129, Feb. 2011, ISSN: 1099-1492. DOI: 10.1002/nbm.1570.

[13] J.-X. Yu, R. R. Hallac, S. Chiguru, and R. P. Mason, "New frontiers and developing applications in $^{19}$F NMR", *Progress in nuclear magnetic resonance spectroscopy*, vol. 70, pp. 25–49, Apr. 2013, ISSN: 0079-6565. DOI: 10.1016/j.pnmrs.2012.10.001. [Online]. Available: https://www.ncbi.nlm.nih.gov/pmc/articles/PMC3613763/ (visited on 06/17/2024).

[14] U. Flögel, S. Su, I. Kreideweiß, Z. Ding, L. Galbarz, J. Fu, C. Jacoby, O. Witzke, and J. Schrader, "Noninvasive detection of graft rejection by in vivo $^{19}$F MRI in the early stage", *American Journal of Transplantation*, vol. 11, no. 2, pp. 235–244, 2011, ISSN: 1600-6143. DOI: 10.1111/j.1600-6143.2010.03372.x. [Online]. Available: https://onlinelibrary.wiley.com/doi/abs/10.1111/j.1600-6143.2010.03372.x (visited on 06/17/2024).

[15] U. Flögel, Z. Ding, H. Hardung, S. Jander, G. Reichmann, C. Jacoby, R. Schubert, and J. Schrader, "In vivo monitoring of inflammation after cardiac and cerebral ischemia by fluorine magnetic resonance imaging", *Circulation*, vol. 118, no. 2, pp. 140–148, Jul. 8, 2008, ISSN: 1524-4539. DOI: 10.1161/CIRCULATIONAHA.107.737890.

[16] R. Schwarz, M. Schuurmans, J. Seelig, and B. Künnecke, "$^{19}$F-MRI of perfluorononane as a novel contrast modality for gastrointestinal imaging", *Magnetic Resonance in Medicine*, vol. 41, no. 1, pp. 80–86, Jan. 1999, ISSN: 0740-3194. DOI: 10.1002/(sici)1522-2594(199901)41:1<80::aid-mrm12>3.0.co;2-6.

[17] P. Bachert, "Pharmacokinetics using fluorine NMR in vivo", *Progress in Nuclear Magnetic Resonance Spectroscopy*, vol. 33, no. 1, pp. 1–56, Jul. 1, 1998, ISSN: 0079-6565. DOI: 10.1016/S0079-6565(98)00016-8. [Online]. Available: https://www.sciencedirect.com/science/article/pii/S0079656598000168 (visited on 06/17/2024).

[18] S. Liu, S. J. Shah, L. J. Wilmes, J. Feiner, V. D. Kodibagkar, M. F. Wendland, R. P. Mason, N. Hylton, H. W. Hopf, and M. D. Rollins, "Quantitative tissue oxygen measurement in multiple organs using $^{19}$F MRI in a rat model", *Magnetic resonance in medicine : official journal of the Society of Magnetic Resonance in Medicine / Society of Magnetic Resonance in Medicine*, vol. 66, no. 6, pp. 1722–1730, Dec. 2011, ISSN: 0740-3194. DOI: 10.1002/mrm.22968. [Online]. Available: https://www.ncbi.nlm.nih.gov/pmc/articles/PMC3186821/ (visited on 06/17/2024).

[19] M. Plaumann, U. Bommerich, T. Trantzschel, D. Lego, S. Dillenberger, G. Sauer, J. Bargon, G. Buntkowsky, and J. Bernarding, "Parahydrogen-induced polarization transfer to $^{19}$F in perfluorocarbons for $^{19}$F NMR spectroscopy and MRI", *Chemistry – A European Journal*, vol. 19, no. 20, pp. 6334–6339, 2013, ISSN: 1521-3765. DOI: 10.1002/chem.201203455. (visited on 06/17/2024).

[20] S. Langereis, J. Keupp, J. L. J. van Velthoven, I. H. C. de Roos, D. Burdinski, J. A. Pikkemaat, and H. Grüll, "A temperature-sensitive liposomal $^{1}$H CEST and $^{19}$F contrast agent for MR image-guided drug delivery", *Journal of the American Chemical Society*, vol. 131, no. 4, pp. 1380–1381, Feb. 4, 2009, Publisher: American Chemical Society, ISSN: 0002-7863. DOI: 10.1021/ja8087532. [Online]. Available: https://doi.org/10.1021/ja8087532 (visited on 06/17/2024).

[21] L. Ren, S. Chen, W. Jiang, Q. Zeng, X. Zhang, L. Xiao, M. T. McMahon, L. Xin, and X. Zhou, "Efficient temperature-feedback liposome for $^{19}$F MRI signal enhancement", *Chemical Communications*, vol. 56, no. 92, pp. 14 427–14 430, Nov. 19, 2020, Publisher: The Royal Society of Chemistry, ISSN: 1364-548X. DOI: 10.1039/D0CC05809B. [Online]. Available: https://pubs.rsc.org/en/content/articlelanding/2020/cc/d0cc05809b (visited on 06/17/2024).

[22] B. Ross, P. Bhattacharya, S. Wagner, T. Tran, and N. Sailasuta, "Hyperpolarized MR imaging: Neurologic applications of hyperpolarized metabolism", *AJNR: American Journal of Neuroradiology*, vol. 31, no. 1, pp. 24–33, Jan. 2010, ISSN: 0195-6108. DOI: 10.3174/ajnr.A1790. [Online]. Available: https://www.ncbi.nlm.nih.gov/pmc/articles/PMC7964072/ (visited on 06/17/2024).

[23] O. Kraff, A. Fischer, A. M. Nagel, C. Mönninghoff, and M. E. Ladd, "MRI at 7 Tesla and above: Demonstrated and potential capabilities", *Journal of magnetic resonance imaging: JMRI*, vol. 41, no. 1, pp. 13–33, Jan. 2015, ISSN: 1522-2586. DOI: 10.1002/jmri.24573.

[24] R. Hu, D. Kleimaier, M. Malzacher, M. A. Hoesl, N. K. Paschke, and L. R. Schad, "X-nuclei imaging: Current state, technical challenges, and future directions", *Journal of Magnetic Resonance Imaging*, vol. 51, no. 2, pp. 355–376, 2020, ISSN: 1522-2586. DOI: 10.1002/jmri.26780. [Online]. Available: https://onlinelibrary.wiley.com/doi/abs/10.1002/jmri.26780 (visited on 06/17/2024).

[25] O. Maxouri, Z. Bodalal, M. Daal, S. Rostami, I. Rodriguez, L. Akkari, M. Srinivas, R. Bernards, and R. Beets-Tan, "How to $^{19}$F MRI: Applications, technique, and getting started", *BJR|Open*, vol. 5, no. 1, p. 20 230 019, Aug. 2023, ISSN: 2513-9878. DOI: 10.1259/bjro.20230019. [Online]. Available: https://academic.oup.com/bjro/article/7468323 (visited on 08/11/2024).

[26] J. S. van Gorp, P. R. Seevinck, A. Andreychenko, A. J. E. Raaijmakers, P. R. Luijten, M. A. Viergever, M. Koopman, V. O. Boer, and D. W. J. Klomp, "$^{19}$F MRSI of capecitabine in the liver at 7 T using broadband transmit–receive antennas and dual-band RF pulses", *NMR in Biomedicine*, vol. 28, no. 11, pp. 1433–1442, 2015, ISSN: 1099-1492. DOI: 10.1002/nbm.3390. [Online]. Available: https://onlinelibrary.wiley.com/doi/abs/10.1002/nbm.3390 (visited on 06/10/2024).

[27] K. Yee, "Numerical solution of initial boundary value problems involving maxwell's equations in isotropic media", *IEEE Transactions on Antennas and Propagation*, vol. 14, no. 3, pp. 302–307, May 1966, Conference Name: IEEE Transactions on Antennas and Propagation, ISSN: 1558-2221. DOI: 10.1109/TAP.1966.1138693. [Online]. Available: https://ieeexplore.ieee.org/document/1138693 (visited on 06/17/2024).

[28] J. Mallow, "Optimierung der Anwendung von 7 Tesla Ultrahochfeld Magnetresonanztomographie HF-Spulen durch EM-Feldsimulation", Dissertation, Universität Duisburg-Essen, 2016, Ph.D. dissertation, Duisburg, Essen, 2016. [Online]. Available: https://duepublico.uni-due.de/servlets/DocumentServlet?id=42436 (visited on 06/17/2024).

[29] M. H. Busch, W. Vollmann, J. Schnorr, and D. H. Grönemeyer, "Finite volume analysis of temperature effects induced by active MRI implants with cylindrical symmetry: 1. properly working devices", *BioMedical Engineering OnLine*, vol. 4, no. 1, p. 25, Apr. 8, 2005, ISSN: 1475-925X. DOI: 10.1186/1475-925X-4-25. [Online]. Available: https://doi.org/10.1186/1475-925X-4-25 (visited on 06/17/2024).

[30] B. Denis de Senneville, B. Quesson, and C. T. W. Moonen, "Magnetic resonance temperature imaging", *International Journal of Hyperthermia*, vol. 21, no. 6, pp. 515–531, Sep. 1, 2005, ISSN: 0265-6736. DOI: 10.1080/02656730500133785. (visited on 06/17/2024).

[31] Y.-M. Seo, S.-A. Im, I. K. Sung, and Y. A. Youn, "The prognosis of brain magnetic resonance imaging injury pattern for outcomes of hypothermia-treated infants", *Medicine*, vol. 99, no. 48, e23176, Nov. 25, 2020. DOI: 10.1097/MD.0000000000023176. [Online]. Available: https://journals.lww.com/md-journal/fulltext/2020/11250/the_prognosis_of_brain_magnetic_resonance_imaging.26.aspx (visited on 06/17/2024).

[32] B. Madore, "MR thermometry", in *Advances in Magnetic Resonance Technology and Applications*, vol. 1, Elsevier, 2020, pp. 885–905, ISBN: 978-0-12-817057-1. DOI: 10.1016/B978-0-12-817057-1.00036-6. [Online]. Available: https://linkinghub.elsevier.com/retrieve/pii/B9780128170571000366 (visited on 06/17/2024).

[33] V. Rieke and K. B. Pauly, "MR thermometry", *Journal of magnetic resonance imaging : JMRI*, vol. 27, no. 2, pp. 376–390, Feb. 2008, ISSN: 1053-1807. DOI: 10.1002/jmri.21265. [Online]. Available: https://www.ncbi.nlm.nih.gov/pmc/articles/PMC2780364/ (visited on 06/17/2024).

[34] M. H. Levitt, *Spin dynamics: basics of nuclear magnetic resonance*, 2nd ed. Chichester, England; Hoboken, NJ: John Wiley & Sons, 2008, 714 pp., OCLC: ocn141380283, ISBN: 978-0-470-51118-3 978-0-470-51117-6.

[35] W. Demtröder, *Atome, Moleküle und Festkörper* (Experimentalphysik / Wolfgang Demtröder 3), 5., neu bearbeitete und aktualisierte Auflage. Berlin Heidelberg: Springer Spektrum, 2016, 586 pp., ISBN: 978-3-662-49093-8. DOI: 10.1007/978-3-662-49094-5.

[36] Z.-P. Liang and P. C. Lauterbur, *Principles of magnetic resonance imaging: a signal processing perspective*. Bellingham, Wash., New York: SPIE Optical Engineering Press; IEEE Press, 2000, OCLC: 557447393, ISBN: 978-0-470-54565-2.

[37] R. J. Kirkpatrick, "Nuclear magnetic resonance spectroscopy", in *Handbook of Analytical Techniques in Concrete Science and Technology*, Elsevier, 2001, pp. 205–230, ISBN: 978-0-8155-1437-4. DOI: 10.1016/B978-081551437-4.50009-6. [Online]. Available: https://linkinghub.elsevier.com/retrieve/pii/B9780815514374500096 (visited on 08/07/2024).

[38] E. M. Haacke, Ed., *Magnetic resonance imaging: physical principles and sequence design*, New York: Wiley, 1999, 914 pp., ISBN: 978-0-471-35128-3.

[39] S. C. Bosshard, "Non-invasive assessment of sensory and nociceptive processing in mice using functional MRI", Ph.D. dissertation, ETH Zurich, 2011. [Online]. Available: http://hdl.handle.net/20.500.11850/109936 (visited on 08/07/2024).

[40] H. Friebolin, *Ein- und zweidimensionale NMR-Spektroskopie: eine Einführung*, 5., vollständig überarbeitete und aktualisierte Auflage, in collab. with C. M. Thiele. Weinheim: Wiley-VCH-Verlag GmbH & Co. KGaA, 2013, 429 pp., ISBN: 978-3-527-33492-6.

[41] D. I. Hoult and R. E. Richards, "The signal-to-noise ratio of the nuclear magnetic resonance experiment", *Journal of Magnetic Resonance*, vol. 24, no. 1, pp. 71–85, Oct. 1, 1976, ISSN: 0022-2364. DOI: 10.1016/0022-2364(76)90233-X. [Online]. Available: https://www.sciencedirect.com/science/article/pii/002223647690233X (visited on 06/04/2024).

[42] G. Mur, "Absorbing boundary conditions for the finite-difference approximation of the time-domain electromagnetic-field equations", *IEEE Transactions on Electromagnetic Compatibility*, vol. EMC-23, no. 4, pp. 377–382, Nov. 1981, ISSN: 0018-9375. DOI: 10.1109/TEMC.1981.303970. [Online]. Available: http://ieeexplore.ieee.org/document/4091495/ (visited on 07/01/2024).

[43] T. Weiland, "A discretization model for the solution of maxwell's equations for six-component fields", *Archiv Elektronik und Uebertragungstechnik*, vol. 31, pp. 116–120, Apr. 1, 1977, ADS Bibcode: 1977ArElU..31..116W. [Online]. Available: https://ui.adsabs.harvard.edu/abs/1977ArElU..31..116W (visited on 07/01/2024).

[44] D. Meschede, C. Gerthsen, and H. Vogel, Eds., *Gerthsen Physik*, 25. Auflage, Springer-Lehrbuch, Berlin Heidelberg: Springer Spektrum, 2015, 1047 pp., ISBN: 978-3-662-45976-8. DOI: 10.1007/978-3-662-45977-5.

[45] A. Krischke and K. Rothammel, *Rothammels Antennenbuch* (DARC-Buchreihe Antennentechnik), 13., aktualisierte und erweiterte Auflage. Baunatal: DARC Verlag GmbH, 2013, 1504 pp., ISBN: 978-3-88692-065-5.

[46] H. Haf, Ed., *Höhere Mathematik für Ingenieure. 1: Analysis / bearb. von Herbert Haf*, 7., überarb. und erw. Aufl, Lehrbuch Mathematik, Wiesbaden: Teubner, GWV Fachverlage, 2006, 604 pp., ISBN: 978-3-8351-0045-9.

[47] J. Schneider, "Understanding the finite-difference time-domain method", 2011. [Online]. Available: https://api.semanticscholar.org/CorpusID:123243832.

[48] J. W. Hand, "Modelling the interaction of electromagnetic fields (10 MHz–10 GHz) with the human body: Methods and applications", *Physics in Medicine and Biology*, vol. 53, no. 16, R243–R286, Aug. 21, 2008, ISSN: 0031-9155, 1361-6560. DOI: 10.1088/0031-9155/53/16/R01. [Online]. Available: https://iopscience.iop.org/article/10.1088/0031-9155/53/16/R01 (visited on 07/01/2024).

[49] C.-N. Chen, D. Hoult, and V. Sank, "Quadrature detection coils—a further $\sqrt{2}$ improvement in sensitivity", *Journal of Magnetic Resonance (1969)*, vol. 54, no. 2, pp. 324–327, Sep. 1983, ISSN: 00222364. DOI: 10.1016/0022-2364(83)90057-4. [Online]. Available: https://linkinghub.elsevier.com/retrieve/pii/0022236483900574 (visited on 06/04/2024).

[50] V. Sank, C.-N. Chen, and D. Hoult, "A quadrature coil for the adult human head", *Journal of Magnetic Resonance (1969)*, vol. 69, no. 2, pp. 236–242, Sep. 1986, ISSN: 00222364. DOI: 10.1016/0022-2364(86)90075-2. [Online]. Available: https://linkinghub.elsevier.com/retrieve/pii/0022236486900752 (visited on 06/04/2024).

[51] F.-H. Lin, K. K. Kwong, I.-J. Huang, J. W. Belliveau, and L. L. Wald, "Degenerate mode birdcage volume coil for sensitivity-encoded imaging", *Magnetic Resonance in Medicine*, vol. 50, no. 5, pp. 1107–1111, Nov. 2003, ISSN: 0740-3194, 1522-2594. DOI: 10.1002/mrm.10632. [Online]. Available: https://onlinelibrary.wiley.com/doi/10.1002/mrm.10632 (visited on 06/04/2024).

[52] P. B. Roemer, W. A. Edelstein, C. E. Hayes, S. P. Souza, and O. M. Mueller, "The NMR phased array", *Magnetic Resonance in Medicine*, vol. 16, no. 2, pp. 192–225, Nov. 1990, ISSN: 0740-3194, 1522-2594. DOI: 10.1002/mrm.1910160203. [Online]. Available: https://onlinelibrary.wiley.com/doi/10.1002/mrm.1910160203 (visited on 06/04/2024).

[53] H. Lindner, H. Brauer, C. Lehmann, and H. Lindner, *Taschenbuch der Elektrotechnik und Elektronik: mit 108 Tabellen*, 8., neu bearb. Aufl. München Wien: Fachbuchverl. Leipzig im Carl Hanser Verl, 2004, 696 pp., ISBN: 978-3-446-22546-6.

[54] F. Strauß, *Grundkurs Hochfrequenztechnik: eine Einführung* (Studium Nachrichtentechnik), 1. Aufl. Wiesbaden: Vieweg + Teubner, 2012, 196 pp., ISBN: 978-3-8348-1242-1.

[55] K.-N. Kim, "Homogeneous and heterogeneous resonators in ultrahigh field MRI", 2011, Publisher: Duisburg, Essen, 2011. [Online]. Available: https://bibliographie.ub.uni-due.de/servlets/DozBibEntryServlet?id=ubo_mods_00032766&lang=en (visited on 11/13/2020).

[56] E. Wilkinson, "An n-way hybrid power divider", *IEEE Transactions on Microwave Theory and Techniques*, vol. 8, no. 1, pp. 116–118, Jan. 1960, ISSN: 0018-9480. DOI: 10.1109/TMTT.1960.1124668. [Online]. Available: http://ieeexplore.ieee.org/document/1124668/ (visited on 01/29/2025).

[57] J. Frahm, A. Haase, and D. Matthaei, "Rapid NMR imaging of dynamic processes using the FLASII technique", *Magnetic Resonance in Medicine*, vol. 3, no. 2, pp. 321–327, 1986, ISSN: 1522-2594. DOI: 10.1002/mrm.1910030217. [Online]. Available: https://onlinelibrary.wiley.com/doi/abs/10.1002/mrm.1910030217 (visited on 06/18/2024).

[58] U. Klose, "Mapping of the radio frequency magnetic field with a MR snapshot FLASH technique", *Medical Physics*, vol. 19, no. 4, pp. 1099–1104, 1992, ISSN: 0094-2405. DOI: 10.1118/1.596828.

[59] S. Akoka, F. Franconi, F. Seguin, and A. Le Pape, "Radiofrequency map of an NMR coil by imaging", *Magnetic Resonance Imaging*, vol. 11, no. 3, pp. 437–441, 1993, ISSN: 0730-725X. DOI: 10.1016/0730-725x(93)90078-r.

[60] T. Herrmann, "Entwicklung eines Anregungs- und Empfangssystems zur Primaten-Bildgebung an einem 7 Tesla Ultrahochfeld Human-Ganzkörper MRT-System", de, Ph.D. dissertation, Mar. 2014. [Online]. Available: https://duepublico2.uni-due.de/receive/duepublico_mods_00033454.

[61] K. Setsompop, V. Alagappan, B. Gagoski, T. Witzel, J. Polimeni, A. Potthast, F. Hebrank, U. Fontius, F. Schmitt, L. L. Wald, and E. Adalsteinsson, "Slice-selective RF pulses for in vivo B inhomogeneity mitigation at 7 tesla using parallel RF excitation with a 16-element coil", *Magnetic Resonance in Medicine*, vol. 60, no. 6, pp. 1422–1432, 2008, ISSN: 1522-2594. DOI: 10.1002/mrm.21739. [Online]. Available: https://onlinelibrary.wiley.com/doi/abs/10.1002/mrm.21739 (visited on 06/18/2024).

[62] J. E. Holmes and G. M. Bydder, "MR imaging with ultrashort TE (UTE) pulse sequences: Basic principles", *Radiography*, vol. 11, no. 3, pp. 163–174, Aug. 2005, ISSN: 10788174. DOI: 10.1016/j.radi.2004.07.007. [Online]. Available: https://linkinghub.elsevier.com/retrieve/pii/S1078817404001257 (visited on 08/11/2024).

[63] E. L. Hahn, "Spin echoes", *Physical Review*, vol. 80, no. 4, pp. 580–594, Nov. 15, 1950, ISSN: 0031-899X. DOI: 10.1103/PhysRev.80.580. [Online]. Available: https://link.aps.org/doi/10.1103/PhysRev.80.580 (visited on 06/30/2024).

[64] C. Renschen, *Der Einfluß starker Magnetfelder auf die gemessene Temperatur bei FOTEMP Meßsonden*, 2007.

[65] P. Villa-Valverde, I. Rodríguez, D. Padró, M. Benito, C. E. Garrido-Salmon, and J. Ruiz-Cabello, "A dual $^{1}$H/$^{19}$F birdcage coil for small animals at 7 T MRI", *Magnetic Resonance Materials in Physics, Biology and Medicine*, vol. 32, no. 1, pp. 79–87, Feb. 2019, ISSN: 0968-5243, 1352-8661. DOI: 10.1007/s10334-018-00733-z. [Online]. Available: http://link.springer.com/10.1007/s10334-018-00733-z (visited on 07/02/2024).

[66] J. Bernarding, C. Bruns, I. Prediger, M. Mützel, and M. Plaumann, "Detection of sub-nmol amounts of the antiviral drug favipiravir in $^{19}$F MRI using photo-chemically induced dynamic nuclear polarization", *Scientific Reports*, vol. 14, no. 1, p. 1527, Jan. 17, 2024, ISSN: 2045-2322. DOI: 10.1038/s41598-024-51454-4. [Online]. Available: https://www.nature.com/articles/s41598-024-51454-4 (visited on 07/02/2024).

[67] W. Robien. "Heptafluorobutyric acid - $^{19}$F NMR - chemical shifts - SpectraBase". (), [Online]. Available: https://spectrabase.com/spectrum/3WaBTeVYO7y (visited on 06/10/2024).

[68] S. Souci, W. Fachmann, and H. Kraut, *Food Composition and Nutrition Tables*. Stuttgart: Medpharm Scientific Publishers, 2000.

[69] R. A. Newmark and C. H. Sederholm, "NMR determinations of barriers to internal rotation in halogen-substituted ethanes", *The Journal of Chemical Physics*, vol. 43, no. 2, pp. 602–623, Jul. 15, 1965, ISSN: 0021-9606, 1089-7690. DOI: 10.1063/1.1696785. [Online]. Available: https://pubs.aip.org/jcp/article/43/2/602/209844/NMR-Determinations-of-Barriers-to-Internal (visited on 07/28/2024).

[70] R. A. Newmark and R. Graves, "Internal rotation in liquid 1, 2-difluorotetrachloroethane", *The Journal of Physical Chemistry*, vol. 72, no. 12, pp. 4299–4303, 1968, Publisher: ACS Publications.

[71] B. A. Berkowitz, J. T. Handa, and C. A. Wilson, "Perfluorocarbon temperature measurements using $^{19}$F NMR", *NMR in Biomedicine*, vol. 5, no. 2, pp. 65–68, Mar. 1992, ISSN: 0952-3480, 1099-1492. DOI: 10.1002/nbm.1940050204. [Online]. Available: https://analyticalsciencejournals.onlinelibrary.wiley.com/doi/10.1002/nbm.1940050204 (visited on 07/03/2024).

[72] A. Dimitrov, U. Groß, W. Storek, J. Burdon, *et al.*, "Temperature-dependent changes in the $^{19}$F NMR spectra of perfluorocyclohexyl ethers", *Journal of fluorine chemistry*, vol. 78, no. 1, pp. 1–5, 1996, Publisher: Elsevier.

[73] C. Bruns, R. Ringleb, I. Prediger, F. Euchner, J. Bernarding, and M. Plaumann, "Organic fluorine compounds and their uses as molecular MR-based temperature sensors", *ChemPhysChem*, vol. 24, no. 22, e202300512, 2023, ISSN: 1439-7641. DOI: 10.1002/cphc.202300512. [Online]. Available: https://onlinelibrary.wiley.com/doi/abs/10.1002/cphc.202300512 (visited on 06/17/2024).

[74] A. A. Ribeiro and M. J. Glen, "$^{19}$F-$^{13}$C, $^{1}$H-$^{13}$C multi-bond and single-bond 2D correlations and determinations of coupling-constant signs", *Journal of Magnetic Resonance, Series A*, vol. 107, no. 2, pp. 158–166, Apr. 1, 1994, ISSN: 1064-1858. DOI: 10.1006/jmra.1994.1063. [Online]. Available: https://www.sciencedirect.com/science/article/pii/S1064185884710631 (visited on 06/10/2024).

[75] R. M. Lynden-Bell, "Relaxation and linewidths in some nuclear magnetic resonance spectra", *Proceedings of the Royal Society of London. Series A. Mathematical and Physical Sciences*, vol. 286, no. 1406, pp. 337–351, 1965, Publisher: The Royal Society London.

[76] D. H. Gultekin and J. C. Gore, "Temperature dependence of nuclear magnetization and relaxation", *Journal of Magnetic Resonance*, vol. 172, no. 1, pp. 133–141, Jan. 2005, ISSN: 10907807. DOI: 10.1016/j.jmr.2004.09.007. [Online]. Available: https://linkinghub.elsevier.com/retrieve/pii/S1090780704002812 (visited on 07/03/2024).

[77] E. Van Dijk, A. Hoogeveen, and S. Abeln, "The hydrophobic temperature dependence of amino acids directly calculated from protein structures", *PLOS Computational Biology*, vol. 11, no. 5, H. Grubmüller, Ed., e1004277, May 22, 2015, ISSN: 1553-7358. DOI: 10.1371/journal.pcbi.1004277. [Online]. Available: https://dx.plos.org/10.1371/journal.pcbi.1004277 (visited on 07/03/2024).

[78] A. L. Lee, A. K. Pandey, S. Chiniforoush, M. Mandal, J. Li, C. J. Cramer, C. L. Haynes, and W. C. Pomerantz, "Development of a highly responsive organofluorine temperature sensor for $^{19}$F magnetic resonance applications", *Analytical Chemistry*, vol. 94, no. 9, pp. 3782–3790, Mar. 8, 2022, ISSN: 0003-2700, 1520-6882. DOI: 10.1021/acs.analchem.1c04248. [Online]. Available: https://pubs.acs.org/doi/10.1021/acs.analchem.1c04248 (visited on 07/03/2024).

[79] C. Prinz, P. R. Delgado, T. W. Eigentler, L. Starke, T. Niendorf, and S. Waiczies, "Toward $^{19}$F magnetic resonance thermometry: Spin–lattice and spin–spin-relaxation times and temperature dependence of fluorinated drugs at 9.4 T", *Magnetic Resonance Materials in Physics, Biology and Medicine*, vol. 32, no. 1, pp. 51–61, Feb. 2019, ISSN: 0968-5243, 1352-8661. DOI: 10.1007/s10334-018-0722-8. [Online]. Available: http://link.springer.com/10.1007/s10334-018-0722-8 (visited on 08/10/2024).

[80] F. Mysegaes, P. Voigt, P. Spiteller, I. Prediger, J. Bernarding, and M. Plaumann, "Two fluorinated thulium complexes as molecular temperature sensors in MR applications", *Chemical Communications*, vol. 59, no. 61, pp. 9340–9343, 2023, ISSN: 1359-7345, 1364-548X. DOI: 10.1039/D3CC02724D. [Online]. Available: https://xlink.rsc.org/?DOI=D3CC02724D (visited on 08/08/2024).

# 11 Declaration of Honor

I hereby declare that I prepared this thesis without impermissible help of third parties and that none other than the indicated tools have been used; all sources of information are clearly marked, including my own publications.

In particular I have not consciously:

- Fabricated data or rejected undesired results,
- Misused statistical methods with the aim of drawing other conclusions than those warranted by the available data,
- Plagiarized external data or publications,
- Presented the results of other researchers in a distorted way.

I am aware that violations of copyright may lead to injunction and damage claims of the author and also to prosecution by the law enforcement authorities.

I hereby agree that the thesis may be reviewed for plagiarism by mean of electronic data processing.

This work has not yet been submitted as a doctoral thesis in the same or a similar form in Germany or in any other country. It has not yet been published as a whole.

Hohendodeleben, August 13, 2024

Christian Bruns